

Emittance Measurements from a Laser Driven Electron Injector

David A. Reis

Stanford Linear Accelerator Center
Stanford University
Stanford, CA 94309

SLAC-Report-539

Prepared for the Department of Energy
under contract number DE-AC03-76SF00515

For Marissa.

Emittance Measurements from a Laser Driven Electron Injector

by

David A. Reis

Submitted in Partial Fulfillment
of the
Requirements for the Degree
Doctor of Philosophy

Supervised by

Professor Adrian C. Melissinos
and
Professor David D. Meyerhofer

Department of Physics and Astronomy
The College
Arts and Sciences
The University of Rochester
Rochester, New York

1999

Curriculum Vitae

The author was born in Buffalo, New York on the 28th of January, 1970. He attended the University of California at Berkeley from 1988 to 1993, and graduated with an A.B. in physics. He came to the University of Rochester in the Fall of 1993 and began graduate studies in physics. He received the Department of Education Fellowship for the years 1993 through 1995 and received the Masters of Arts Degree in 1995. Also, in 1995 he began to pursue his research in the application of lasers to high energy and accelerator physics at the Stanford Linear Accelerator Center under the direction of professors Adrian C. Melissinos and David D. Meyerhofer of the University of Rochester. In addition to the research presented in this thesis, the author has contributed to the field of non-linear quantum electrodynamics.

Acknowledgments

I have pondered what to say in these acknowledgments for quite a while; nonetheless, I am certain that I cannot possibly do everyone justice. It seems a little ironic and perhaps cliché to say that physics is not done in a vacuum, but this really is true. There are a number of very talented individuals who have contributed greatly to the both to the successful construction and operations of the Gun Test Facility (GTF) and to my growth as a physicist and a person.

I would like to thank the entire Gun Test Facility Collaboration that includes individuals from Argonne National Lab, Brookhaven National Lab, the Stanford Linear Accelerator Center, the University of California at Los Angeles and The University of Rochester. The late Jim Weaver was instrumental in nearly every aspect of the GTF. Without his hard work and attention to detail, I do not think there would have been a GTF. Herman Winick was the mastermind behind the GTF; it was his baby, but he let us run it like our own. Herman, we got 1π mm-mrad . . . at least. John Schmerge was kind enough to tackle many of the administrative problems of the GTF when I know he would have rather been in the lab more often. He has been responsible, perhaps as much as anyone else, for the success of the GTF. He also has taught me much about accelerator physics and FELs as well as has kept me on my toes. Mike Hernandez has also taught me much about accelerator physics. He was responsible for and provided much of the beam-line diagnostics. The two of us took all of the emittance data together. He has also provided simulations of the gun and linac. I would also like to thank Adrian Melissinos and David Meyerhofer for not only being great advisors and friends but also for allowing me to cannibalize the SLAC Experiment-144 laser stockpile; Steve Milton for loaning the laser oscillator; Dennis Palmer for his work on the prototype gun and solenoid that were primarily the result of the thesis work; Bob Siemann for the loan of the streak camera as well as his newly hired post-doc, Mark Hogan, to operate it; and Jym Clendenin, Eric Colby, Max Cornaccia, Alan Fisher, Uli Haug, Theo Kotseroglou, Helmut Wiedemann, David Whittum, and many others for all of their help.

In addition, I would like to thank the entire staff of the Stanford Synchrotron Radiation Lab. Each member of the staff has probably been recruited to help in one way or another. I would especially like to acknowledge the hard work of Brian Choi, Joe Ormonde, and Rocky Pena for the construction of the Laser Room; Ian Evans and Reuben Yotam for the safety and beam containment systems; Dave Ernst, Bill Hauffer, Ben Poling, Mike Swanson, and Gary Woodcock for mechanical support; Harry Morales and

Mike Nalls for vacuum support; Ramona Theobald for assembling many an electronics chassis, terminating cables, and keeping the candy jar full; The SPEAR operators, especially P.J. Boussina, Craig Haggart, Glen Kerr, and Thomas Nyugen, for helping with everything from data acquisition and controls to building the laser enclosure and most importantly for allowing essentially unlimited access to the Linac Vault (while not injecting into SPEAR).

There are also many other people which I would like to acknowledge for their various contributions on a more personal level. Professor Sumner Davis of the University of California at Berkeley had faith in me at a time when I was a little timid when it came to the laboratory environment. Professor Berken Chang of California State University at Los Angeles was a joy to work with and taught me much—about physics and otherwise. Thomas Koffas has been a great friend and colleague. He has taught me how to study (which somehow escaped my grasp until graduate school), helped me through my class work, and taught me how to count in Greek (through dominoes, cards, backgammon, etc.). He has been a great office-mate on both sides of the country. There have been many who have helped me learn about lasers. Professor Davis allowed me my first toy: an Ar⁺ pumped dye laser. Alan Fry introduced me to Nd:YLF and glass lasers and entrusted me to work on “his” system. He also introduced me to the “tweaking bug” which I think I finally overcame. Wolfram Ragg taught me “German” engineering and yielded the E144 terawatt laser to me. And, David Meyerhofer taught me that the last 5% is hardly ever worth the effort—a philosophy that was often echoed by Adrian Melissinos with “the better is the enemy of the good.” This philosophy could easily come into conflict with what my mother has taught me—to strive for perfection in the details. I think it is necessary to obtain a certain amount of harmony between the two, and I have done my best to accomplish this (dotting the appropriate i’s, crossing the appropriate t’s, and not worrying too much about their fonts). I would also like to say thanks to the entire E144 collaboration for allowing me the privilege of participating in a world class experiment. I don’t know which is more prestigious the PRL or the New York Times article.

Finally, I would like to thank my family for all of their support and encouragement. I know my mother will look at this thesis more critically than anyone (although not for the physics). My wife and best friend, Marissa, has been most supportive (and patient). She has allowed me to turn the majority of the apartment into one big messy office during these last months of writing. I have no excuse for the mess anymore. Thank you, Marissa, for everything. I love you and I’ll clean it up in the morning

This work was supported in part by the U.S. Department of Energy under contract numbers DE-AC03-76SF00515 and DE-FG02-91ER40685.

Abstract

The Gun Test Facility (GTF) at the Stanford Linear Accelerator Center was constructed to develop an appropriate electron beam suitable for driving a short wavelength free electron laser (FEL) such as the proposed Linac Coherent Light Source (LCLS). For operation at a wavelength of 1.5 Å, the LCLS requires an electron injector that can produce an electron beam with approximately 1π mm-mrad normalized rms emittance with at least 1 nC of charge in a 10 ps or shorter bunch.

The GTF consists of a photocathode rf gun, emittance-compensation solenoid, 3 m linear accelerator (linac), drive laser, and diagnostics to measure the beam. The rf gun is a symmetrized 1.6 cell, S-band, high gradient, room temperature, photocathode structure. Simulations show that this gun when driven by a temporally and spatially shaped drive laser, appropriately focused with the solenoid, and further accelerated in linac can produce a beam that meets the LCLS requirements.

This thesis describes the initial characterization of the laser and electron beam at the GTF. A convolved measurement of the relative timing between the laser and the rf phase in the gun shows that the jitter is less than 2.5 ps rms. Emittance measurements of the electron beam at 35 MeV are reported as a function of the (Gaussian) pulse length and transverse profile of the laser as well as the charge of the electron beam at constant phase and gradient in both the gun and linac. At 1 nC the emittance was found to be $\sim 13 \pi$ mm-mrad for 5 ps and 8 ps long laser pulses. At 0.5 nC the measured emittance decreased approximately 20% in the 5 ps case and 40% in the 8 ps case. These measurements are between 40–80% higher than simulations for similar experimental conditions. In addition, the thermal emittance of the electron beam was measured to be 0.15π mm-mrad.

Contents

1 Introduction	1	3 Electron Injector	53
1.1 High Quality Charged Particle Beams	2	3.1 Electron Beam Line	54
1.2 Free Electron Lasers	5	3.1.1 Photocathode rf Gun	55
1.3 FEL Mechanism	8	3.1.2 Solenoid	59
1.4 Gun Test Facility	12	3.1.3 Linac	63
2 Electron Beam Parameters	14	3.1.4 Quadrupoles	65
2.1 Electron Emission from a Metal Cathode	15	3.1.5 BeamLine Diagnostics	68
2.1.1 Work Function and the Schottky Effect	16	Beam Profile Monitors	68
2.1.2 Thermal Emission	18	Faraday Cups	69
2.1.3 Field Emission	20	Toroids	71
2.1.4 Photoemission and Quantum Efficiency	22	4 Drive Laser	73
2.1.5 Estimate of Emission Time	25	4.1 Gun Drive Laser Requirements	74
2.2 Single Particle Dynamics for an rf Gun	26	4.2 Chirped Pulse Amplification	78
2.2.1 Longitudinal Dynamics	27	4.3 Oscillator	78
2.2.2 Transverse Dynamics	30	4.4 Pulse Expansion Stage	79
2.2.3 Peak Electric Field Determination	32	4.5 Regenerative Amplifier	80
2.3 Single Particle Trajectories in the Absence of Acceleration	34	4.6 Pulse Compression Stage	83
2.4 Electron Beam Characterization	35	4.7 Frequency Conversion	84
2.4.1 Choice of Coordinate System	35	4.8 Imaging and Transport System	86
2.4.2 Phase Space and Emittance	36	4.9 Longitudinal Pulse Shaping	90
2.4.3 Quantum Limit to Emittance	41	4.9.1 Chirped Gaussian Pulses	91
2.4.4 Transverse Thermal Emittance	41	4.9.2 Pulse Shaping Utilizing the Chirp in the Compressor	94
2.4.5 Longitudinal Thermal Emittance and Uncorrelated Energy Spread	44	4.9.3 Other Methods for Pulse Shaping	95
2.4.6 Magnetic Emittance	45	Frequency Domain Pulse Shaping	96
2.4.7 Multipole Emittance	46	Temporal Pulse Stacker	97
2.4.8 rf Emittance	46	5 rf Systems and Timing Measurements	108
2.4.9 Space-charge Emittance	47	5.1 rf System	110
2.4.10 Transverse Emittance Summary and Estimates	50	5.1.1 Low Level rf	110
		5.1.2 High Power rf	111
		5.1.3 rf Diagnostics	112
		5.2 Timing Measurements	116
		5.2.1 High Power rf Phase Stability	117
		5.2.2 Low Level rf and Laser Stability	121
		5.2.3 Other Timing Measurements	124
		5.2.4 Summary	125
		6 Results	127
		6.1 Quantum Efficiency Measurements	128
		6.1.1 Cathode Uniformity	131
		6.1.2 Schottky Scans	135
		6.2 Emittance Measurements	137

6.2.1	Thermal Emittance Measurement	137
6.2.2	Quadrupole Scans	139
6.2.3	Spotsize Determination	142
	Image Acquisition	142
	Beam Moment Calculation	143
	Horizontal-Vertical Coupling	148
	Definition of Beam Size in the Presence of Cross Plane Coupling	151
6.2.4	Operating Parameters	152
6.2.5	Beam Cuts	155
6.2.6	Horizontal Emittance Results	156
	Emittance as a Function of Laser Pulse Length	157
	Emittance as a Function of Charge	159
	Emittance as a Function of Transverse Laser Profile	159
6.3	Conclusions	161
	References	167
A	LCLS Design Requirements	174
B	Description of Beam Ellipses	176
B.1	Upright Ellipse in Cartesian Coordinates	179
B.2	Rotated Ellipse in Cartesian Coordinates	179
B.3	Ellipses in Polar Coordinates	182
C	Expansion and Compression	184
C.1	Geometry	185
C.2	Design	188
D	Grazing Incidence Design	191
E	Normal Incidence Mirror Charging	196
F	Emittance Data	200

List of Tables

2.1	Physical properties of copper	17
2.2	Calculated reflectivity of 4.7 eV photons off of copper for normal and grazing incidence	23
2.3	Parameters used for emittance estimates	51
2.4	Emittance scaling and estimates for conditions given in Table 2.3	52
4.1	Laser parameters	76
5.1	Summary of timing jitter results	126
6.1	Experimental conditions for emittance data	154
6.2	Projected transverse emittance summary	156
6.3	Projected transverse emittance for the data analyzed with a definition of the emittance based on 39% of the beam	163
6.4	Comparison of selected emittance measurements with simulation	164
A.1	LCLS design parameters [1]	175
C.1	Expansion and compression parameters	189
F.1	Summary of emittance data	201

List of Figures

1.1	Peak power and wavelength of various light sources.	6
1.2	The proposed Linac Coherent Light Source	7
1.3	Schematic of electron trajectory through the wiggler	9
1.4	Bunching of the electron beam at the FEL wavelength.	10
2.1	Schematic of the rf gun with the longitudinal field profile superimposed.	15
2.2	Potential diagram for the Schottky effect.	19
2.3	Electric field lines for a rough cathode showing field enhancement for convex features.	21
2.4	Reflectivity of copper as a function of incidence angle and polarization	24
2.5	Longitudinal on axis field in 1.6 cell gun.	29
2.6	1.6 cell energy and phase as a function of laser injection phase for 140 MV/m peak field.	30
2.7	Energy and phase for 1.6 cell gun with 140 MV/m maximum accelerating gradient and 50 degree injection phase as a function of kz	31
2.8	Phase space ellipse showing the rms beam size and divergence.	39
2.9	Phase space diagram showing emittance increase due to non-linear rf kick at the exit of a standing wave accelerator.	47
2.10	Phase space under the influence of space-charge	49
3.1	Schematic of the Gun Test Facility beam line.	54
3.2	Plan view of the SLAC Gun Test Facility.	55
3.3	Schematic of the 1.6 cell photocathode gun showing symmetric laser ports in the "half cell".	56
3.4	Schematic of the 1.6 cell photocathode gun showing waveguide feed and symmetric <i>pump-out</i> port.	57
3.5	Schematic of the normal incidence geometry.	58
3.6	Magnetic field map (longitudinal and radial on axis) of the solenoid at an excitation current of 150 A.	61
3.7	Longitudinal field on axis as a function of solenoid excitation current.	62
3.8	Hysteresis in the longitudinal field of the solenoid on axis.	62
3.9	rf power in linac and load (with gun power for reference) before PFN delay.	65
3.10	rf Power in linac and load (with gun power for reference) after PFN delay.	66
3.11	Faraday cup connection: circuit equivalent.	71
3.12	Schematic of a beam toroid.	72
4.1	Block diagram of the gun drive laser.	76
4.2	Schematic of the regenerative amplifier and injection stage.	80
4.3	The Q-switch pulse inside the regen both with and without an injected pulse from the oscillator.	81
4.4	Regen contrast ratio	82
4.5	2:1 Spatial filter	84
4.6	Frequency doubling efficiency for a 2 ps pulse through 1 cm thick KD*P.	86
4.7	Green and UV yield and Green to UV efficiency vs. IR pulse length.	87
4.8	Schematic of the GTF laser transport system.	88
4.9	A simple telescope.	89
4.10	Autocorrelation measurements of the IR laser as a function of grating separation.	93
4.11	Streak camera measurements of the quadrupled laser as a function of grating separation.	95
4.12	UV streak camera pulse showing 4.7 ps pulse with roughly 2 ps/mm spatial chirp.	96
4.13	Streak camera measurements of the doubled laser as a function of grating separation.	97
4.14	Sample streak camera data for the 3 different UV pulses with Gaussian fits.	98
4.15	Calculated clipped Gaussian spectrum (intensity) and resulting temporal (intensity) profile for both a chirped ($b/a=10$) and unchirped ($b/a=0$) pulse.	99
4.16	A schematic of the 16-pulse stacker.	100
4.17	The calculated results of the interference between two pulses separated by approximately the single pulse duration in both an unchirped and 4 times chirped case.	101
4.18	A sample of measured spectra for two pulses with different separations.	103
4.19	The number of fringes measured in the spectrum of two pulses stacked in the temporal pulse stacker versus pulse separation counted in turn of the adjustment screw.	104
4.20	Measured UV pulse for two temporally stacked pulses for various pulse separations.	106
4.21	Schematic for 100% throughput UV pulse stacker with minimal interference.	107
5.1	The 119 MHz source.	110
5.2	The 2856 MHz master clock and 1 kW drive.	111

5.3	High power rf system.	112
5.4	rf diagnostic signals showing the forward,reflected and stored power in the rf gun, and dark current collected on a Faraday cup under these conditions.	114
5.5	Phase detector output as a function of input phase.	116
5.6	Schematic of the phase jitter measurements.	118
5.7	Histograms of the phase of the gun klystron, its drive, and the difference logged for 100 shots over a few minutes.	118
5.8	Histograms of the phase of the gun, the klystron's drive, and the difference logged for 50 shots over a few minutes.	119
5.9	Steady state gun phase shift as a function of frequency offset.	119
5.10	Spectrum of the 119 MHz from the laser photodiode both with and without feedback on the cavity length.	122
5.11	Spectrum of the 2856 from the multiplier and the laser on a fast photodiode.	123
5.12	Spectrum of the 24 times frequency multiplier when driven with the free running laser.	124
5.13	Experimental setup for beam phase measurement.	125
6.1	Calibration of the laser energy monitor.	129
6.2	The charge and quantum efficiency versus laser energy incident on the cathode.	130
6.3	Quantum efficiency as a function of waveplate angle for grazing incidence.	131
6.4	Quantum efficiency across cathode before "laser cleaning".	132
6.5	A "super-charge" event as seen on the gun field probe and a Faraday cup.	133
6.6	Quantum efficiency across cathode after "laser cleaning".	134
6.7	Fowler Nordheim plot of the dark current before and after "laser cleaning".	136
6.8	A typical Schottky scan from which the laser phase relative to the gun and the thermal emittance are estimated.	137
6.9	Thermal emittance plot.	138
6.10	Lattice used in emittance measurements.	139
6.11	Sample quadrupole scan with least squares fit to thick lens plus drift.	141
6.12	Radial profile and integrated signal for a typical electron beam image.	146
6.13	Logarithmic plot of signal and background pixel amplitudes for a typical electron beam image.	147
6.14	Histogram of signal, background and beam edge pixel amplitudes for all the images of a typical quadrupole scan.	148
6.15	Sample quadrupole scan as a function of the definition of the electron beam extent.	149
6.16	Sample beam image.	150

6.17	Spot size definition.	152
6.18	Emittance as a function of spot-size before the first quadrupole for all beam conditions.	157
6.19	Emittance as a function of solenoid field for 1 nC of charge and different pulse widths.	158
6.20	Emittance as a function of Solenoid for the 0.5 and 1 nC, 5 ps data.	159
6.21	Emittance as a function of Solenoid for the 0.5 and 1 nC, 8 ps data.	160
6.22	Emittance (rms) as a function of solenoid field for 0.5 nC for the transverse Gaussian and clipped Gaussian data.	161
6.23	Emittance (39%) as a function of solenoid field for 0.5 nC for the transverse Gaussian and clipped Gaussian data.	162
B.1	Rotated ellipse.	178
C.1	Grating compression setup.	186
C.2	Expansion setup.	188
D.1	Geometry of grazing incidence showing both the time-slew and the ellipticity generated by the incident laser beam.	193
D.2	Grating geometry for determining beam slew and aspect ratio.	194
D.3	Grazing incidence design: no dispersion correction.	195
E.1	Discharge from the normal incidence laser mirror.	198
F.1	Quadrupole scan for the minimum emittance at 1 nC and 5 ps.	202
F.2	Quadrupole scan for the minimum emittance at 1 nC and 8 ps.	202
F.3	Quadrupole scan for the minimum emittance at 1 nC and 11 ps.	203
F.4	Quadrupole scan for the minimum emittance at 0.5 nC and 5 ps.	203
F.5	Quadrupole scan for the minimum emittance at 0.5 nC and 8 ps.	204
F.6	Quadrupole scan for the minimum emittance at 0.5 nC, 5 ps, and transversely clipped.	204

List of Symbols

Symbol	Representation
ASE	Amplified spontaneous emission
FEL	Free electron laser
GTF	Gun Test Facility
LCLS	Linac Coherent Light Source
S-band	Specifically rf at $f = 2856$ MHz
SLAC	Stanford Linear Accelerator Center
SSRL	Stanford Synchrotron Radiation Lab
regen	Regenerative amplifier
rf	Radio Frequency
IR	Infra-red light more specifically 1053 nm (wavelength of Nd:glass laser)
Green	527 nm (wavelength of doubled Nd:glass laser)
UV	Ultra-violet light more specifically 263 nm (wavelength of quadrupled Nd:glass laser)
a	Gaussian chirp parameter (real coefficient)
b	Gaussian chirp parameter (imaginary coefficient)
c	Speed of light
d	Generic distance
e	Electron charge
f	Focal length
f	Frequency
$f(\epsilon)$	Occupancy of states
k	Wavevector
k_b	Boltzmann constant
k_u	Undulator wavevector
m	Electron mass
n	Index of refraction
p	Momentum
p-polarized	TM polarization
p_r	Radial momentum
p_z	Longitudinal momentum
q	Charge

r	Radius
s-polarized	TE polarization
t	Time
x, y	Transverse spatial coordinate x', y' Divergence angles
z	Longitudinal spatial coordinate
A	Aspect ratio (σ_x/σ_z)
\vec{A}	Vector potential
\vec{B}	Magnetic field (induction)
B_n	Normalized beam brightness
\vec{E}	Electric field
E	Energy
$E(\omega)$	Fourier transform of electric field
E_{eff}	Effective microscopic field
E_r	Transverse electric field
E_z	Longitudinal electric field
I	Current
$I(\omega)$	Spectrum
$I(t)$	Intensity
I_A	Alfvén current
J_e	Electron flux (number)
K	Undulator parameter
L	Lattice transfer function
N_e	Number of electrons
N_u	Number of undulator periods
P_f	Forward power
P_w	Power lost on cavity walls
QE	Quantum efficiency
R_s	Shunt Impedance
$S(\omega)$	Spectral (sideband) density
T	Temperature
T	time delay
TE	Transverse electric
TM	Transverse magnetic
TEM	Transverse electric and magnetic mode
T_f	Fermi temperature
U	Stored energy
V	Electric potential
Γ^x	Area in (x, p_x) space
Φ	Work function (Schottky lowered)
Φ_0	Zero field work function
Q	Quality factor
Q_0	Cavity Q

Q_L	Loaded Q
α	Normalized vector potential
α	Twiss parameter (related to coupling)
β	Field enhancement factor
β	Twiss parameter (related to spotsizes)
β	rf coupling coefficient
β_z	Normalized longitudinal velocity
δ	Skin depth
ϵ	Electronic energy level
ϵ_0	Permittivity of free space
ϵ_{geom}	Geometrical emittance
ϵ_f	Fermi energy
ϵ_n	Normalized emittance
$\epsilon_{39\%}$	39% emittance
η	Quantum efficiency
γ	Normalized beam energy
γ	Twiss parameter (related to divergence)
\hbar	Planks constant divided by 2π
λ	Wavelength
λ_0	Center wavelength
λ_u	Undulator wavelength
μ	Chemical Potential
μ_0	Permiability of free space
μ_x	Geometric transverse space-charge factor
μ_y	Geometric transverse space-charge factor
μ_z	Geometric longitudinal space-charge factor
ω	Angular frequency
ω_0	Center angular frequency
ϕ	Azimuthal angle
ϕ	Beam phase
ϕ_0	Laser-rf phase
ϕ_{opt}	Optimum injection phase for maximizing acceleration in a cavity ($\beta = 1$)
σ	Beam matrix
σ_{ij}	i, j -th component of beam matrix
σ_t	timing jitter
σ_x	rms x -spotsizes
σ_y	rms y -spotsizes
σ_z	rms z -spotsizes
τ	Bunch length
θ	angle
θ_{max}	maximum angle of emission

Chapter 1

Introduction

1.1 High Quality Charged Particle Beams

High quality relativistic charged particle beams are needed for high energy physics and advanced light sources. What constitutes a high quality beam depends on the exact application in mind, but some general statements can be made: the beam should consist of a large number of particles—each particle behaving roughly the same as the next; it should have a very high energy, with small energy spread, and a very short bunch length; and it should be well contained in a small spot with a small divergence. In short, the beam should have a dense phase space i.e., a large amount of charge and a small *emittance*—the beam size multiplied by the divergence angle.

Typical parameters of a beam may include ~ 10 billion particles (~ 1 nC charge) in multi-GeV-TeV energy range, with energy spreads of less than 1%, in a \sim picosecond bunch length, with a normalized transverse emittance¹ on the order of 1 mm-mrad. As the technological limits on production of these high quality beams are (and have been) extended, new physics can be explored. The production of such an electron source, with the specific application of driving a single pass x-ray free electron laser (FEL) (such as the proposed 1.5 Å Linac Coherent Light Source—LCLS [2, 3]), will be the topic of this thesis.

The development of such an electron beam requires a novel electron source. Radio-frequency (rf) thermionic guns are limited to current densities that are too small to produce enough charge while maintaining a high quality electron beam [4]. DC photocathode guns can produce a sufficient charge but a poor quality beam that typically needs to be selectively *damped* and temporally compressed [5]. rf photocathode guns [6] are the most promising technology to date [7]. The state of the art, *emittance-compensated* [8],

¹The transverse beam size multiplied by the divergence angle in the rest frame of the average particle.

photocathode gun has produced a beam with a phase space density within about a factor of 5 [9] of the required density for the LCLS. Simulations show that this gun, driven by an appropriately shaped laser pulse, can produce the required emittance for the LCLS [10, 11]. Other promising sources include the plane-wave transformer [12] and pulsed diode guns [13].

Liouville's Theorem tells states that for an isolated system the local phase space density (and thus volume) is a constant of motion. In terms of the normalized momenta, the phase space density will be constant even under the influence of uniform (linear) acceleration. In order to understand how to produce (and transport) the highest quality beams, it must therefore be understood, under realistic conditions, how to (1) produce the beam with an initially dense phase space and (2) transport and accelerate the beam while maintaining this large phase space density.

The beam by its very nature is a collection of interacting particles. The mutual Coulomb repulsion (often called the *space-charge* force) tends to blow the beam apart, doing most damage while the beam is non-relativistic and decreasing approximately with the inverse square of the beam energy as a result of the balancing effect of the mutual magnetic and electric fields. Even though the phase space density must remain constant locally, (after all, the space-charge forces are conservative) non-linear space-charge effects lead to an effective dilution of the average density in phase space. This can easily become the dominating effect spoiling beam quality. The magnitude of this effect depends significantly on the spatial distribution in the beam. Because the profile of the electron beam will, to first order, follow the profile of the laser pulse, it is desirable to tailor laser profile in order to minimize the detrimental effect of space-charge.

With the great number of mutual interactions to take into account, it is clear that a com-

plete detailed description of the beam is impractical. Nevertheless, the beam can be well characterized by its distribution in phase space, the six dimensional space of the particle positions and canonical momenta. The more dense the phase space, the better is the *quality* of the electron beam. The ultimate limit to the phase space density is determined by the Pauli-exclusion principle for Fermion beams. Typically the phase space is divided into transverse and longitudinal sub-spaces, or transverse and longitudinal *emittances*, that are assumed to be independent of each other (an assumption which may be invalid when considering the space-charge forces acting on a finite bunch).

In addition to internal interactions, the beam also interacts with the environment: rf fields that accelerate the beam, magnets that bend and focus the beam, even the cylindrical beam-pipe that can extract energy from the beam as it passes through it. In fact, the source itself has and contributes to, the beam emittance.

In the remainder of this chapter we will motivate the requirements on the beam emittance for an x-ray FEL. In Chapter 2, we discuss the physics of the rf-photoinjector, including the photoemission process, charged particle acceleration, the definition of beam emittance and other beam parameters, and the mechanisms that generate and increase emittance. To provide a physical understanding of the process, we will emphasize the nature of the different mechanisms as opposed to how they couple to one another. In Chapter 3, we describe the rf injector used to collect the data for this thesis. This includes the photocathode gun and the emittance-compensation solenoid, the 3 m linac section, and various beam diagnostics. Chapter 4 is devoted to the laser used for driving the gun. Emphasis is placed on the pulse shaping capabilities and measurements of the system performance. Chapter 5 describes the strict synchronization requirements for a laser driven photocathode gun, when the laser pulse width is short compared to the rf period. The design of a timing system that meets the R&D requirements of the

facility is also described. Measurements of the timing stability as well as a discussion of how this relates to the timing requirements for the LCLS are also given. In Chapter 6 gives the results of electron beam studies. This includes comparison of emittance measurements as a function of the laser pulse length, charge density, and total charge as a function of the solenoid field strength. In addition, quantum efficiency measurements and a thermal emittance measurement are presented. Finally, we conclude with a summary of what has been accomplished, and present a suggested research program for producing the lowest possible emittance.

1.2 Free Electron Lasers

The FEL is a device that converts kinetic energy from a relativistic electron beam to coherent radiation by passing the electron beam through a periodic magnetic field (undulator or wiggler) inducing a bunch density modulated at the radiated wavelength. Since the first demonstration of the free electron laser (FEL) over twenty years ago [14], FELs have been operated at wavelengths ranging from ~ 200 nm (for example [15, 16, 17, 18]) to > 1 mm (for example [19, 20, 21]) [22]. The wavelength of the FEL radiation is determined by the synchronism condition that the electron beam slips in phase with respect to the radiation by 2π radians per undulator period. In the limit of small transverse momentum, the wavelength is determined by the electron energy and the undulator spacing and is given approximately by $\lambda = \lambda_u/2\gamma^2$, where λ is the radiated wavelength, λ_u is the undulator spacing and γ is the Lorentz factor (the electron energy, E , divided by its rest energy, mc^2). In the limit when a significant portion of the electron energy is from transverse motion, the wavelength increases.

One of the major advantages the FEL has over the conventional laser is its wide range of

tunability. In fact, the tunability of the FEL is essentially limited by technological rather than inherent constraints of achievable undulator spacing, the phase space density, or the electron energy. Another advantage is that, unlike the conventional laser, the waste heat is removed essentially at the speed of light in the FEL. Furthermore, due to the absence of a host material for the lasing medium, the output power is not limited by nonlinear effects. The main disadvantage of the FEL is the size and cost of the devices. Since cheaper devices span most of the visible and near-IR portions of the spectrum (dye-lasers, Ti:sapphire, Optical Parametric Oscillators) [23], future FEL development will be most promising in the Far-IR and the UV to X-ray portion of the spectrum, where few other sources can compete in tunability and output power (for example in the short wavelength range) See Fig. 1.1 for a description of the power and wavelength of various light sources in the sub-micron to Angstrom regime.

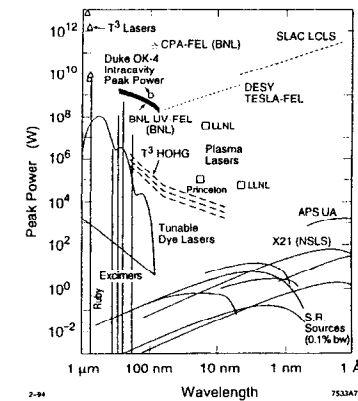


Figure 1.1: Peak power and wavelength of various light sources.

In order to push the FEL limit to shorter wavelengths, research must be done to improve both the undulator and electron beam qualities. The proposed Linac Coherent Light Source (LCLS) at the Stanford Linear Accelerator Center (SLAC) is a single pass, self-amplified spontaneous emission, free-electron laser utilizing the last third of the 3 km SLAC linac and operating at a wavelength of 1.5 \AA [2]. Fig. 1.2 shows a schematic of the LCLS and Table A.1 in Appendix A gives a summary of the proposed operating parameters.

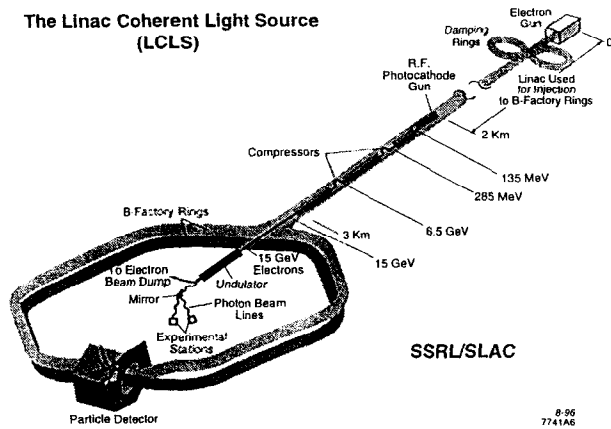


Figure 1.2: Proposed Linac Coherent Light Source, utilizing the last 1 km of the SLAC linac.

A critical component of the LCLS is a high brightness electron source. The source must be able to produce a 1 nC beam with $\leq 1 \pi \text{ mm-mrad}$ normalized rms transverse emittance and $\sim 10 \text{ ps}$ pulse length in order to reach gain saturation in a 100 m undulator. This assumes the beam is accelerated to 15 GeV, and the rms electron beam length

is compressed to 70 fs in the two magnetic chicane compressors. The LCLS design assumes a growth of $\leq 0.5 \pi \text{ mm-mrad}$ in emittance from acceleration and compression processes such that the required emittance at the undulator entrance is less than $1.5 \pi \text{ mm-mrad}$. The limit on the emittance is determined roughly by the requirement that a spatial overlap can be maintained between the electron beam and the radiation in the undulator.

1.3 FEL Mechanism

An electron exchanges energy with an electro-magnetic field according to

$$\dot{\gamma} = e\vec{\beta} \cdot \vec{E}/mc, \quad (1.1)$$

where γ is the beam energy normalized by its rest energy, e is the charge of an electron, $\vec{\beta}$ is the particles velocity normalized to the speed of light, \vec{E} is the electric field of the emitted radiation, m is the mass of the electron and c is the speed of light. For a helical undulator this leads to (see Ref. [24])

$$\dot{\gamma} = \frac{eEK}{mc\gamma} (\sin((k + k_u)c\beta_z t + kz_0 - \omega t)) \quad (1.2)$$

where $K = eB\lambda_u/2\pi mc$ is the undulator parameter (B is the peak magnetic field, λ_u is the undulator wavelength, i.e., the spacing between like magnetic poles), k is the wavevector of the radiation, $k_u = 2\pi/\lambda_u$, and β_z is the longitudinal component of the electron's normalized velocity in the z direction, defined by the axis of the undulator). A similar expression holds in the case of the planar undulator[24]. Depending on the phase of the electron relative to the optical wave, eq. (1.2) can represent either an accelerating or decelerating effect. This has the effect of bunching the electron beam at the

optical wavelength and provides for coherent radiation to be generated at the undulator of the FEL.

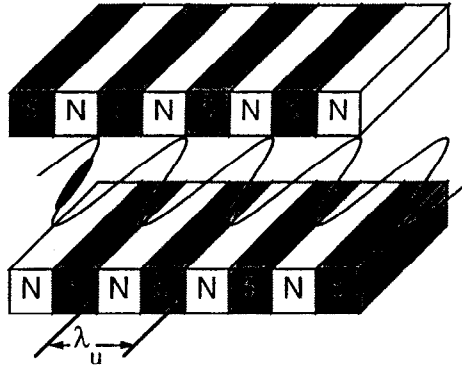


Figure 1.3: Schematic of electron trajectory through the wiggler. The transverse motion allows the electron to slip in phase one cycle of the FEL radiation each wiggler period

For the electron to continually exchange energy with the field, the electron must be in phase with the ponderomotive (beat) wave $\beta_z = \omega/c(k + k_u)$. In other words, the electron has to slip in phase by 2π (or a multiple of 2π) with respect to the emitted radiation over one undulator wavelength. Fig. 1.3 shows a schematic of the electron beam trajectory through the undulator. The requirement that the electron beam stay in phase with the ponderomotive wave in order to continually deposit energy into the EM-field leads to the FEL resonance condition,

$$\lambda = \frac{\lambda_u(1 + K^2 + \gamma^2\theta^2)}{2\gamma^2}, \quad (1.3)$$

where θ is the angle the radiation makes with respect to direction of the average electron (see, for example, [24]). Fig. 1.4 shows the potential as seen in rest frame of

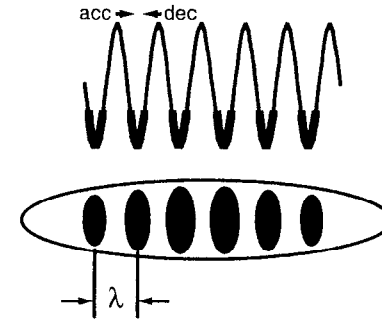


Figure 1.4: Bunching of the electron beam at the FEL wavelength.

the electron bunch, and the resultant bunching of the beam. The electron produces spontaneous radiation with a linewidth (FWHM) given by $\Delta\omega/\omega_0 = \Delta\lambda/\lambda_0 \approx 1/N_u$, where N_u is the number of undulator periods (i.e., the length of the undulator divided by λ_u) [24, 25]. Because of the nonlinear dispersion relation for a relativistic electron, $E = \sqrt{p^2c^2 + m^2c^4}$, there is a difference in the wavelength for spontaneous emission and absorption. This leads to a small signal gain for stimulated emission [24]. Thus, an FEL can amplify a seed pulse of the right frequency or even amplify existing spontaneous emission (Self Amplified Spontaneous Emission —SASE [26]). Since there are no *suitable* optics in the Å range, an Å FEL will be a single pass device designed to reach gain saturation within the length of the undulator. Furthermore, because of the lack of a good source of a seed pulse, the Å FEL will work on the principle of SASE.

In order to motivate the emittance requirements for an FEL, the forward-directed radiation is considered. Taylor expanding eq. (1.3) to lowest order,

$$\frac{\Delta\lambda}{\lambda} = -\frac{2\Delta\gamma}{\gamma} + \frac{2K\Delta K}{1+K^2} + \frac{\gamma^2(\Delta\theta)^2}{1+K^2}. \quad (1.4)$$

If one imposes the constraint that the fractional spread in wavelength be less than the

half-width ($1/2N_u$) [24], to match the linewidth for spontaneous emission, one obtains the following requirements:

$$\frac{\Delta\gamma}{\gamma} < \frac{1}{4N_u}, \quad (1.5)$$

$$\frac{K\Delta K}{1+K^2} < \frac{1}{4N_u}, \text{ and} \quad (1.6)$$

$$\Delta\theta < \left(\frac{1+K^2}{2\gamma^2 N_u}\right)^{\frac{1}{2}}. \quad (1.7)$$

Furthermore, with the requirement that the Rayleigh range² of the radiation be equal to the undulator length (such that the electron beam and the radiation are well matched), the requirement on the geometrical emittance of the electron beam (spotsizes times divergence in the rest frame of the average electron) is

$$\epsilon_{\text{geom}} < \frac{\lambda}{2\pi}. \quad (1.8)$$

The limit in eq. (1.8) is twice the diffraction limit of a lowest order Gaussian beam of wavelength λ . For the LCLS, with $\gamma \approx 3 \cdot 10^4$, a 1.5π mm-mrad normalized emittance ($\gamma\epsilon_{\text{geom}}$) is the diffraction limit for 6 \AA x-rays, and thus the LCLS, according to this simple estimate, can drive a 3 \AA FEL. A more precise requirement is that the optical beam and the electron beam stay well overlapped over one gain length (e-folding); however, in the case of a single pass FEL, the electron beam determines both the optical mode and the gain, and this is therefore a somewhat circular condition. The actual requirement on emittance depends on the particular kind of focusing used, the pulse length, gain-guiding, and a more complete 3 dimensional theory of the FEL process [27]. For the LCLS design parameters, a 1.5π mm-mrad, 1 nC beam can drive the FEL into saturation at 1.5 \AA in a 100 m long wiggler [2].

²The distance from the beam waist in which the spotsizes has increased by $\sqrt{2}$

1.4 Gun Test Facility

The Gun Test Facility (GTF) was constructed to develop an appropriate injector for the LCLS and is located in the injector vault of the Stanford Synchrotron Radiation Lab (SSRL) at SLAC (see Fig. 3.2 on page 55). The GTF was built in collaboration with Argonne National Lab, Brookhaven National Lab, the University of California at Los Angeles, the University of Rochester and others. The GTF consists of a photocathode drive laser, rf power stations, a 3 m SLAC S-band linac section, an rf gun and an emittance-compensation solenoid, as well as beam diagnostics to characterize the electron beam [28]. A SLAC XK-5 Klystron powers the 3 m linac section, which is capable of accelerating electrons to 50 MeV. A second XK-5 powers the gun. The beam line includes instrumentation for measuring the geometric emittance, beam profile, beam charge, beam momentum spectrum, and bunch length (see Fig. 3.1, page 54). The first gun, currently being characterized at the GTF, was designed in collaboration between Brookhaven National Laboratory (BNL), SLAC and the University of California at Los Angeles. It is a high-gradient symmetrized 1.6 cell standing-wave structure. Prototypes of the gun and the emittance-compensation solenoid were characterized at BNL [11].

The drive laser was constructed in collaboration with the University of Rochester and is a Chirped Pulse Amplification [29], frequency quadrupled, Nd:glass based system. The system is capable of producing picosecond pulses in the UV, with single pulse energies as high as 0.5 mJ, at a rep-rate of 2.5 Hz. Because of the relatively high bandwidth of the laser, temporal pulse shaping can be obtained with picosecond characteristics. Spatial shaping is accomplished by clipping the beam on an aperture and imaging this aperture onto the cathode, in order to avoid smearing from diffraction.

The drive laser for a photocathode gun must operate synchronously with the accelerat-

ing rf. The timing jitter between the arrival time of the laser and the operating phase in the gun should be on the order of a fraction of the bunch length, and possibly far less, depending on the particular application. Acceptable timing jitter for the R&D application has been achieved, without using feedback, by driving the gun and accelerator at a harmonic of a passively mode-locked laser oscillator. This oscillator also serves as the front end of the laser system, from which a single pulse is selected for amplification and frequency conversion to drive the photocathode.

Chapter 2

Electron Beam Parameters

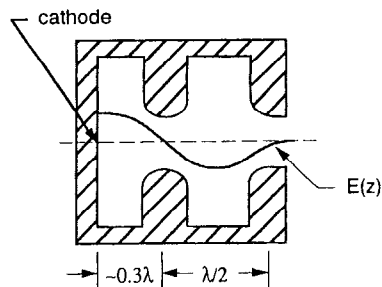


Figure 2.1: Schematic of the rf gun with the longitudinal field profile superimposed.

In this chapter, the different mechanisms for electron emission are discussed as is the origin of the quantum efficiency. Single particle dynamics for a standing wave structure are presented in order to gain understanding of the acceleration process. Fig. 2.1 shows a schematic of the 1.6 cell gun used in this experiment along with a longitudinal field profile superimposed. In order to understand a particle beam with a finite number of particles, the foundations of beam characterizations are given. This includes the definition of the beam emittance and the different mechanisms for emittance growth. The scaling laws for the emittance sources are then summarized, and estimates based on typical beam parameters are made followed by a discussion of how the emittance can be reduced to the LCLS requirements can be achieved.

2.1 Electron Emission from a Metal Cathode

In a high gradient photocathode gun a metal photocathode is typically used. While the metal cathode suffers from relatively low quantum efficiency when compared to semi-

conductor cathodes, it is quite robust and can withstand very high electric fields. In the case of the gun at the GTF, the photocathode is copper and consists of the entire back wall of the gun. This eliminates any joints between the cathode and the gun where electrical breakdown is likely to occur. At low fields and temperatures the emission from the gun is dominated by the photo-emission process; however, as the accelerating field is increased a significant "dark-current" background begins to appear well above the levels of the expected thermal emission. This emission is due to the quantum mechanical tunneling of the electrons through the Schottky lowered potential barrier.

2.1.1 Work Function and the Schottky Effect

The amount of energy required to liberate an electron from the Fermi level¹ to the vacuum is known as the work function (where the vacuum means that the electron is sufficiently far from the cathode that the potential from its image charge can be ignored—typically a few nm). In general, the work function for a metal is a few electron volts such that UV photons or very high temperatures ($\sim 10^4 - 10^5$ K) are required for emission. The exact value of the work function depends on the crystal orientation and detailed surface physics of the metal. In fact, the exact nature of the work function is quite complex and is beyond the scope of this thesis. Table 2.1 gives the accepted work function for various crystal planes of copper as well other properties used in the text.

An average value of 4.7 eV will be used for the purpose of calculations except when an upper limit on a quantity that depends on the energy difference between the laser and the work function is desired (in which case 4.5 eV is used). The wavelength of a frequency quadrupled Nd:glass laser is 263 nm (4.7 eV) such that electrons can be

¹The energy of the highest filled electronic state at absolute zero

Table 2.1: Physical properties of copper.

Index of refraction (4.7 eV)	$n = n_r + in_i$	$1.47 + 1.73i$	[30]
Skin depth	δ	24 nm	calc.
Fermi energy	ϵ_f	7 eV	[31]
Work Function	Φ_0	4.59 eV (100)	[31]
		4.48 eV (110)	
		4.98 eV (111)	
Free electron density	n_e	$8.45 \cdot 10^{22} \text{cm}^{-2}$	[31]
DC conductivity	σ_0	$5.88 \cdot 10^5 \Omega^{-1} \text{cm}^{-1}$	[31]
Average (inelastic) scattering time	τ	23 fs	calc.
Mean free path (for $E = \epsilon_f + \hbar\omega$)	Λ	50 nm	calc.

emitted from either the 110 or 100 plane (until, as will be shown shortly, the electric field approaches ~ 85 MV/m where emission can occur from all 3 planes).

In the presence of an external field, the effective work function of the cathode is changed. When the field is accelerating electrons away from the cathode surface, the work function is lowered such that emission is more favorable. However, due to the presence of the electron's image potential, the lowering is not linear in the applied field. Fig. 2.2 shows a schematic of the applied (accelerating), image, and combined potential. The combined potential can be written as

$$eV = -eEz - \frac{e^2}{16\pi\epsilon_0 z}, \quad (2.1)$$

where E is the applied electric field, ϵ_0 , is the permittivity of free space, z is the distance from the cathode, and it is assumed that $kz \ll 1$, where k is the wave number of the applied field. The potential barrier is a minimum when the derivative of eq. (2.1) with

respect to the distance from the cathode vanishes: i.e., when

$$z = \frac{1}{2} \sqrt{\frac{e}{4\pi\epsilon_0}} E^{-\frac{1}{2}}, \quad (2.2)$$

and

$$eV = -e \sqrt{\frac{e}{4\pi\epsilon_0}} E^{\frac{1}{2}}. \quad (2.3)$$

The effective work function is then written as

$$\Phi(E) = \Phi_0 - e \sqrt{\frac{e}{4\pi\epsilon_0}} E^{\frac{1}{2}}. \quad (2.4)$$

The lowering of the potential barrier is known as the Schottky effect [32]. For 100 MV/m the work function is effectively decreased by ~ 0.38 eV while the distance from the cathode in which the barrier is a minimum is ~ 2 nm consistent with the approximation that the applied field is independent of position considering that the rf wavelength is about 10^7 nm (10 cm).

2.1.2 Thermal Emission

In the thermionic gun electron emission is achieved by raising the temperature of the cathode to a point where a significant number of electrons has energy above the (effective) work function of the cathode. The thermionic gun therefore emits over a wide range of phases and across many rf buckets. As a consequence, beam loading and energy spread can be quite significant for a thermionic gun. Thermionic guns therefore typically employ energy filters, beam choppers and "alpha-magnets"². In addition, the charge in each bucket is small and the emittance can be large compared to the requirements of the LCLS.

²A dipole magnet which is designed such that the transit time is independent of energy. It gets its name due to the charged particle trajectories resembling the Greek letter α .

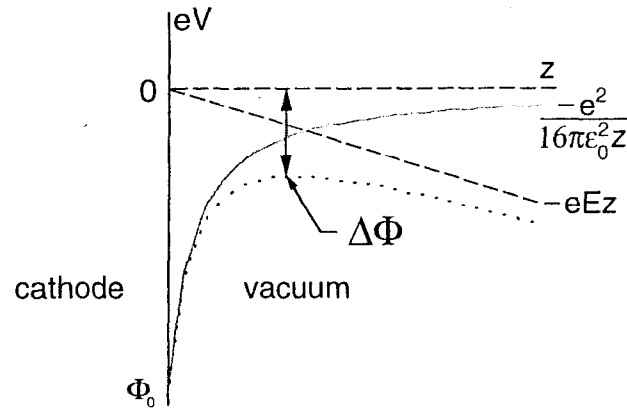


Figure 2.2: Potential diagram for the Schottky effect. Solid line is the potential due to the image charge, the long dashed is the accelerating potential, and the short dashed is the combined potential.

In order to estimate the number of electrons thermally emitted from the rf gun, it is noted that the occupancy of states in a metal is given by the Fermi-Dirac distribution,

$$f(\epsilon) = \frac{1}{e^{\frac{\epsilon - \mu}{k_b T}} + 1}, \quad (2.5)$$

where μ is the chemical potential, given by

$$\mu \approx \epsilon_f \quad k_b T \ll \epsilon_f \approx k_b T_f \quad (2.6)$$

for temperatures much less than the Fermi temperature (T_f). From Table 2.1, $\epsilon_f \approx 7$ eV for copper such that $T_f \approx 8 \cdot 10^4$ K. In this limit, the Fermi-Dirac distribution is approximated as a Boltzmann distribution,

$$f(\epsilon) \approx e^{-\frac{\epsilon - \epsilon_f}{k_b T}} \quad \epsilon > \epsilon_f. \quad (2.7)$$

At $T = 300$ K ($k_b T \sim 1/40$ eV) and $E_0 = 100$ MV/m, the occupancy at the effective work function of copper $\epsilon - \epsilon_f \approx 4.1$ eV is $f(\epsilon - \epsilon_f = 4.1 \text{ eV}) \sim e^{-164}$.

More specifically, the thermionic emission rate can be derived by treating the electrons as an ideal fermi-gas in thermal and chemical equilibrium with the cathode [31]. In terms of the electron flux it is given by

$$J_{e^-} = \frac{(k_b T)^2 m}{2\pi^2 \hbar^3} e^{-\Phi/k_b T}. \quad (2.8)$$

This is known as the Richardson-Dushman equation for thermionic emission. For the parameters given above, the emission rate is $\sim 10^{-37} \text{ e}^- \text{ m}^{-2} \text{ s}^{-1}$ which is negligible.

2.1.3 Field Emission

When operating at fields on the order of 10–100 MV/m, a significant amount of “Dark” current is observed to be emitted from the photocathode gun. Part of the explanation can be attributed to localized increases in the electric field at the cathode due to a rough surface. Because the electric field is perpendicular to a conducting surface, the field strength will be higher when the cathode is convex than when it is concave (as shown in Fig. 2.3). If sharp “whiskers” exist on the cathode the field can become high enough that an electrical breakdown occurs. The field enhancement is characterized by $\beta_E = E_{\text{eff}}/E$, where E_{eff} is the microscopic electric field [33], such that the effective work function eq. (2.4) becomes

$$\Phi(E, \beta_E) = \Phi_0 - e \sqrt{\frac{e \beta_E E}{4\pi \epsilon_0}}. \quad (2.9)$$

However, even with this explanation the observed amount of emitted current grows much too rapidly with the applied field for a reasonable surface roughness. This phenomenon is known as field emission and the explanation is purely quantum mechanical

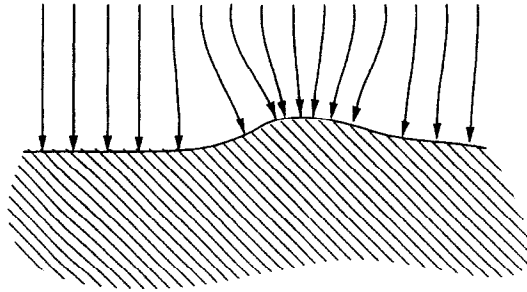


Figure 2.3: Electric field lines for a rough cathode showing field enhancement for convex features.

in nature. As the applied field grows, the Schottky lowered barrier becomes narrow enough that there is a significant probability for tunneling through the barrier. In fact, this was one of the earliest observations of quantum mechanical tunneling [34]. Reference [33] gives an approximate form for the current (in Amperes averaged over 1 rf cycle)

$$\langle I \rangle_{T_r} = \frac{5.7 \cdot 10^{-12} 10^{4.52\Phi^{-0.5}} A_e (\beta E)^{2.5} e^{-\frac{6.53 \cdot 10^9 \Phi^{1.5}}{\beta E}}}{\Phi^{1.75}} \text{ A}, \quad (2.10)$$

where all energies are in (electron) Volts, A_e is the emitting area, and E is in Volts/m. The enhancement factor for the cathode can be determined by the slope of $\langle I \rangle_{T_r} / E^{2.5}$ as a function of $\ln(1/E)$ (and the effective emitting area can be determined by the intercept). In Section 6.1.1 Fowler-Nordheim plots are given for the initial copper cathode and for both before and after “laser cleaning” the cathode in order to increase the photoelectron yield.

2.1.4 Photoemission and Quantum Efficiency

One of the major advantages of using photoemission (as opposed to thermionic emission) as an electron source is, that to first order, the photo-emitted beam takes on the characteristics of the drive (laser) beam. This can be used to tailor the longitudinal and transverse shape of the electron beam in an attempt to achieve the lowest possible emittance directly from the source. If the laser pulse length is short compared to the rf period, then the emitted beam will (typically) have a well defined energy with low energy spread. In addition, a single bunch or any number of bunches can be selected by selecting how many laser pulses are incident on the cathode.

The quantum efficiency (QE or η) is defined as the number of electrons emitted from the gun per *incident* number of laser photons:

$$\eta = \frac{N_e}{N_\gamma}. \quad (2.11)$$

This definition of the QE is essentially an effective quantum efficiency since it does not take into account the reflectance of the laser off of the cathode. It is, therefore, a practical definition. However, this means that the QE depends on the incident angle of the photons.

In the case of a copper cathode operated near room temperature and a quadrupled Nd:glass laser, only electrons near the fermi level can escape since $\hbar\omega - \Phi \ll \Phi$ and $T \ll T_f$. In addition, due to the short skin depth at the laser wavelength, only electrons near the surface of the metal can be excited. Because the mean free path of the electrons is slightly longer than the skin depth, most of the electrons do not undergo inelastic scattering.

With these simplifications it is reasonably straightforward to determine the form of

Table 2.2: Calculated reflectivity of 4.7 eV photons off of copper for normal and grazing incidence.

angle	polarization	reflectivity	$\frac{1-R(\theta_i)}{1-R(0)}$
0°		0.35	1.0
72°	s-polarized	0.68	0.49
72°	p-polarized	0.23	1.2

the emitted current by integrating over the available states in which the longitudinal momentum before emission satisfies $p_z^2/2m > \epsilon_f + \Phi$ and is oriented towards the surface. The result (see ref [35]) is that the number of emitted electrons per photon of frequency ω ,

$$n(\omega) \propto (\hbar\omega - \Phi)^2. \quad (2.12)$$

For a finite temperature a correction is given by Fowler [36]; however, the differences are only important right at threshold [37].

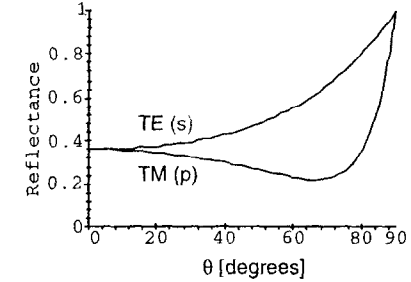
Using eqs. (2.12) and (2.4) the quantum efficiency is rewritten as

$$\eta = \eta_0 \left(\hbar\omega - \Phi_0 + e\sqrt{\frac{e}{4\pi\epsilon_0}} E^{\frac{1}{2}} \right)^2, \quad (2.13)$$

where η_0 is a constant which depends on (among other things) on the cleanliness of the cathode, and E strictly includes any enhancements due to surface features. The QE achieved (after "laser cleaning") was $\sim 3 \cdot 10^{-5}$ electrons/photons at normal incidence with an applied field of ~ 100 MV/m. This compares with a QE of $\sim 4.5 \cdot 10^{-5}$ as reported in [38].

As the quantum efficiency is defined here, it depends on the polarization of the laser for incident angles other than normal. Fig. 2.4 shows the reflectivity of 4.7 eV photons from copper as a function of angle of incidence for both transverse magnetic (TM, p)

and transverse electric (TE, s) polarizations as determined by the Fresnel equations (see for example ref. [39]). The reflectivity of the s-polarized light (TE) rises monotonically

**Figure 2.4:** Reflectivity of copper versus angle for 4.7 eV photons off of copper for s-polarized (upper) and p-polarized (lower) light.

(until grazing incidence where it is unity) while the p-polarized (TM) light first decreases and then increases. The reflectivity is lower (thus the absorbed light and hence the quantum efficiency is greater) for p-polarization than for s-polarization for all angles except normal incidence where s- and p-polarization are indistinguishable. Table 2.2 summarizes the reflectivity and the fractional number of absorbed photons (normalized to 0°) for 0° and 72°: the two angles of incidence possible with the rf photocathode gun used in this thesis.

Measurements of the quantum efficiency as a function of polarization for grazing incidence are given in Section 6.1. Note that according to Table 2.2 there should be ~ 2.5 times higher efficiency for p-polarized light than for s; however, a value of ~ 6 is seen. The discrepancy is likely explained due to additional Schottky lowering of the work function due to the electric field of the laser for p-polarization (i.e., when the electric field is perpendicular to the surface.) At typical laser intensities the electric field is

~ 40 MV/m which when combined with the applied field and the surface roughness may explain the discrepancy.

2.1.5 Estimate of Emission Time

In order for the longitudinal shape of the electron beam to follow the shape of the laser pulse, the emission must be prompt. In this section, the emission time is estimated using the typical energy of an electron and the characteristic depth at which it is produced. The length scale over which emission occurs is the skin depth of the laser—the depth at which the electric field amplitude has been reduced to $\frac{1}{e}$ of the field at the surface³. The skin depth is given by

$$\delta = \frac{1}{k_i} = \frac{c}{\omega n_i}, \quad (2.14)$$

where n_i is the imaginary portion of the index of refraction. For 4.7 eV photons the index of refraction and the associated skin depth for copper are given in Table 2.1. The index is determined from ref. [30] from a least squares fit of the theory to experimental data. The corresponding skin depth is 24 nm. For comparison, for $\omega = 2\pi \cdot 2856$ MHz, the rf frequency of the gun, the skin depth is $\sim 1\mu\text{m}$.

Most of the electrons will be excited from near the Fermi energy, such that their energy inside the cathode will be given by $\epsilon_f + \hbar\omega$. Therefore their typical velocity will be

$$\beta = \sqrt{\frac{\epsilon_f + \hbar\omega}{1/2mc^2}} \approx 7 \cdot 10^{-3}, \quad (2.15)$$

where β is the velocity normalized to the speed of light. The majority of the electrons

³The number of photons is reduced to $\frac{1}{e}$ of the number at the surface.

will then be emitted in a time

$$\tau_e < \frac{\delta}{\beta c} \approx 10 \text{ fs}. \quad (2.16)$$

This is shorter than the average scatter time (determined from the DC conductivity in the Drude model), longer than the UV single cycle time ($\sim 1\text{fs}$), and much shorter than the typical laser pulse width.

2.2 Single Particle Dynamics for an rf Gun

In this section, the longitudinal and transverse dynamics for a single particle in a standing wave accelerator structure are derived. The emphasis will be on the rf gun in which the particles start from rest. The shunt impedance is defined which relates the maximum Voltage gain obtainable through the cavity to the stored Power in the cavity.

The accelerating modes of the cavity are transverse magnetic (TM) modes. The longitudinal component to the electric field is given by

$$E_z = E(z) \sin(\omega t + \phi_0) \hat{z}, \quad (2.17)$$

where $E(z)$ contains the spatial variation of the electric field ($\cos kz$ for the TM_{010} mode), $k = 2\pi/\lambda$ is the wavevector of the accelerating rf, $\omega = 2\pi f$ is the angular frequency, and ϕ_0 is a constant phase term (corresponding to the laser arrival phase at the cathode). $z = 0$ is defined as the cathode surface where the electric field must terminate normal to the surface.

This field is clearly unphysical by itself as it is not divergence free. Therefore, there

must be a non-zero radial component⁴. $\vec{\nabla} \cdot \vec{E} = 0$ implies

$$\frac{\partial E_z}{\partial z} = -\frac{1}{r} \frac{\partial r E_r}{\partial r}, \quad (2.18)$$

or

$$E_r = -\frac{r}{2} \frac{\partial E_z}{\partial z}, \quad (2.19)$$

where it has been assumed that E_z is independent of r which is valid for $kr \ll 1$.

Furthermore, there must be an azimuthal magnetic field (from $\vec{\nabla} \times \vec{B} = \frac{1}{c} \frac{\partial \vec{E}}{\partial t}$),

$$cB_\theta = \frac{r}{2c} \frac{\partial E_z}{\partial t}. \quad (2.20)$$

From the above fields and the Lorentz force law ($\vec{F} = q(\vec{E} + \vec{v} \times \vec{B})$) the two coupled differential equations for the longitudinal and transverse momenta of a single particle of charge e are,

$$\frac{dp_r}{dt} = -\frac{er}{2} \frac{\partial E_z}{\partial z} - \frac{e\beta_z r}{2c} \frac{\partial E_z}{\partial t}, \text{ and} \quad (2.21)$$

$$\frac{dp_z}{dt} = eE_z + \frac{e\beta_z r}{2c} \frac{\partial E_z}{\partial t}, \quad (2.22)$$

where eqs. (2.19) and (2.20) give radial electric and azimuthal magnetic fields and E_z is given by eq. (2.17).

2.2.1 Longitudinal Dynamics

The second term in eq. (2.22) and the entire radial motion, eq. (2.21), become negligible essentially immediately in the photocathode gun. This leads to a differential energy gain,

$$\frac{d\gamma}{dz} = \alpha k \frac{E(z)}{E_0} \sin(kz + \phi), \quad (2.23)$$

⁴the electric field for a TM_{0pq} mode is independent of azimuthal angle.

where E_0 is the peak on axis field and $\phi = \omega t - kz + \phi_0$, is the beam phase defined such that

$$\phi = k \int_0^z \left(\frac{1}{\beta} - 1 \right) dz + \phi_0 = k \int_0^z \left(\frac{\gamma}{\sqrt{\gamma^2 - 1}} - 1 \right) dz + \phi_0. \quad (2.24)$$

And, the normalized vector potential α is

$$\alpha = \frac{eE_0}{2kmc^2}, \quad (2.25)$$

which is typically on the order of 1–2 for the high gradient photo-injector.

In the case of the 1.5 cell gun where only the TM_{010} mode is used, the differential energy gain can be written as

$$\frac{d\gamma}{dz} = \alpha k (\sin \phi + \sin(\phi + 2kz)). \quad (2.26)$$

The first term in eq. (2.26) is due to the forward wave and the second term is due to the reverse wave of the rf (absent in the case of the traveling wave linac). For long structures and relativistic beams the effects of the reverse wave average to zero as the particles slip over 2 rf waves every cycle.

Ref [40] derives approximate solutions for the energy and phase in the 1.5 cell case. In the case of the 1.6 cell rf gun, the elongated half-cell, requires higher spatial harmonics in the accelerating field for resonance. For relativistic beams the higher spatial harmonics do not contribute to the acceleration, but in the rf gun they cannot be ignored [41].

The spatial variation of the electric field, $E(z)$, for the 1.6 cell gun is given by simulations and is shown in Fig. 2.5 [42]. Also shown in Fig. 2.5 is the Electric field as seen by a particle traveling the speed of light for an injection phase of 52° . This is the phase that maximizes the energy gain and will be used in the definition of the shunt impedance of the structure in Section 2.2.3.

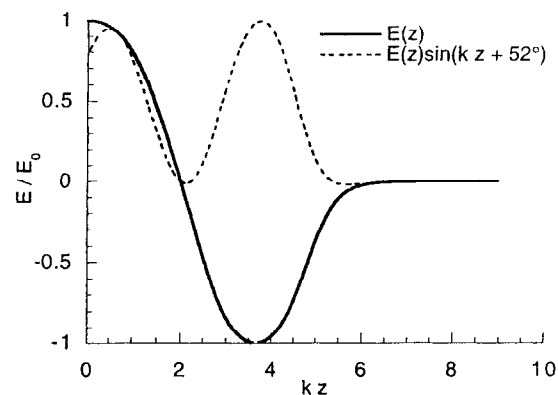


Figure 2.5: Longitudinal on axis field in 1.6 cell gun (solid) and corresponding field as seen by ultrarelativistic particle for maximum acceleration (dashed).

The energy and phase of the particles can be determined by solving eqs. (2.23) and (2.24) self consistently. This is done using numerical integrations and the field map (Fig. 2.5). Fig. 2.6 shows the calculated energy and phase at the exit of the gun ($z = 12$ cm from the cathode, $kz \approx 7.2$) as a function of the laser injection phase. The phase that maximizes the energy gain is not the same phase that minimizes the differential defocusing kick at the exit of the gun (see Section 2.2.2). The maximum energy gain is at $\sim 50^\circ$ while the injection phase for minimizing the defocusing kick at the exit of the gun is $\sim 80^\circ$. The phase chosen for the emittance measurements presented in Section 6.2.6 was 50° . While this minimizes the longitudinal phase space out of the gun ($d\gamma/dz = 0$) this puts a non-linear energy chirp on the beam that cannot be easily removed. In addition, this decrease in the longitudinal emittance is almost certainly going to correspond to an increase in the transverse emittance. The evolution of the energy and phase for an

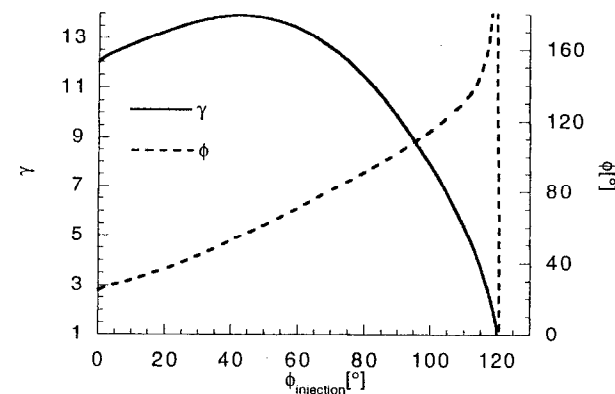


Figure 2.6: 1.6 cell energy and phase as a function of laser injection phase for 140 MV/m peak field.

input phase of 50° through the structure is shown in Fig. 2.7 for $E_0 = 140$ MV/m. The effects of the reverse wave can be clearly seen in the modulation of the energy gain. In addition in Fig. 2.7, the beam is seen to become relativistic very near the cathode.

2.2.2 Transverse Dynamics

Transverse dynamics cannot be completely neglected and become an important factor in the production of high quality electron beams. For a single particle the radial motion is quite uninteresting; however, the difference in the motion from the head to the tail of a finite beam will be one of the limiting factors in producing a very low emittance beam (non-linear rf effects). Here the transverse motion of a single particle in a standing wave accelerator is derived. The magnitude of the transverse motion will be seen to be small such that the beam size on the exit is essentially the same as at the cathode; however,

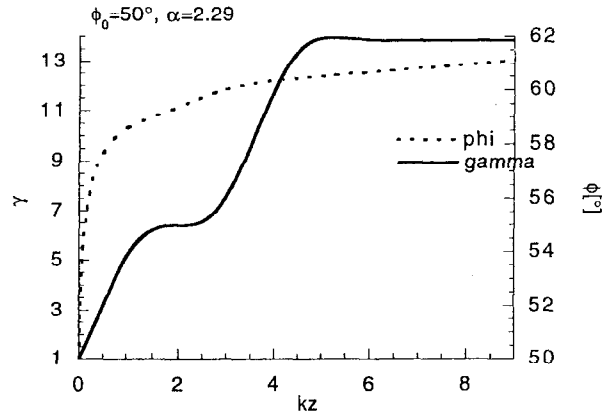


Figure 2.7: Energy and phase for 1.6 cell gun with 140 MV/m maximum accelerating gradient and 50 degree injection phase as a function of kz .

at the exit of the gun, where the field terminates abruptly, a potentially large difference in the transverse kick as a function of time develops. This result will be used in Section 2.4.8 to estimate the “rf” contribution to the beam emittance (see Section 2.4.8).

For simplicity a single TM_{010} mode is assumed such that $E(z) = E_0 \cos(kz)$.

During the short period when the beam is non-relativistic, eqs. (2.21) and (2.22) can be rewritten as

$$\frac{d\beta_r}{dt} \approx -\alpha\beta_z(kr)\omega \cos \phi_0, \text{ and} \quad (2.27)$$

$$(2.28)$$

$$\frac{d\beta_z}{dt} \approx 2\alpha\omega \left(\sin \phi_0 + (kr)\frac{\beta_r}{2} \cos \phi_0 \right), \quad (2.29)$$

where the approximations that β_r, β_z, kz , and $\omega t \ll 1$ have been made. And, where α was defined in eq. (2.25). In the limit that $\frac{(kr)\beta_r \cos \phi_0}{2 \sin \phi_0} \ll 1$, i.e., as long as ϕ_0 does not

approach 0, β_r is given as,

$$\beta_r \approx \alpha(\omega t)^2(kr) \sin 2\phi_0 \ll 1. \quad (2.30)$$

Once the beam becomes relativistic ($\beta_z \approx 1$), eq. (2.21) is integrated to yield

$$\beta_r(z) \approx -(kr)\alpha \cos(kz) \sin(kz + \phi_0) + \text{const.}, \quad (2.31)$$

The constant in eq. (2.31) will depend on the injection phase as well as the phase slippage when the beam is non-relativistic. The beam envelope makes oscillations at twice the rf frequency (due to the reverse wave passing over the beam) and as long as $kr \ll 1$ these oscillations will be small. Since r is typically on the order of a mm and $k \approx 0.06\text{mm}^{-1}$, this is quite reasonable.

At the exit of the gun the longitudinal electric field must terminate. For simplicity the field is assumed to terminate abruptly. While this is clearly unphysical, it turns out that the dominant factor in the exit kick arises from the temporal not spatial dependence of the electric field. The result is that at the exit of the gun the radial velocity is given by

$$\beta_r = \alpha(kr) \sin \phi_{\text{exit}} + \text{const.}, \quad (2.32)$$

where ϕ_{exit} is the exit phase of the gun. This result will be used later to estimate the rf emittance growth due to a finite pulse length. This time dependent kick is important in the case of the linac where the input (focusing) kick is stronger than the output (defocusing) kick due to the large energy gain through the structure. In fact the linac focusing is an important part of the emittance-compensation process.

2.2.3 Peak Electric Field Determination

In order to determine the energy from the gun, the accelerating gradient as a function of the input power to the gun needs to be known. The peak on axis field will be

proportional to the square root of the forward power to the gun in steady state. The proportionality constant will depend on the particular geometry of the structure as well as on the conductivity of the walls. It is typical to introduce the shunt impedance which relates the maximum Voltage gain to the power dissipated in the walls as

$$\frac{V^2}{2R_s} = P_w, \quad (2.33)$$

where, R_s is the shunt impedance, P_w is the power dissipated in the cavity walls and V is the maximum Voltage gain for a particle traversing the structure at the speed of light [43, 44]. The Voltage gain is given by integrating the longitudinal field across the structure namely

$$V = \int_0^{z_{\text{exit}}} E(z) \sin(kz + \phi_{\text{opt}}) dz, \quad (2.34)$$

where ϕ_{opt} is the injection phase that optimizes the voltage gain.

The power dissipated on the wall can be rewritten in terms of the quality factor (Q_0) and the stored energy (U)

$$P_w = \frac{\omega U}{Q_0}. \quad (2.35)$$

The shunt impedance is then

$$R_s = \frac{V^2 Q_0}{2\omega U}. \quad (2.36)$$

For the 1.6 cell gun reported on here with a stored energy of $U = 4.638$ J the peak on axis field is given by to be $E_0 = 100$ MV/m. This leads to $V \sim 4.74$ MV gain for $\phi_{\text{opt}} \sim 52^\circ$ where eq. (2.34) and the longitudinal field profile (from simulation [42]) have been used. This, combined with the measured $Q_0 = 12,000$, leads to a shunt impedance of $R_s = 1.6$ M Ω .

Now, the power dissipated from the forward power to the structure needs to be determined. In steady state the power dissipated in the walls is equal to the forward power to the structure minus the power reflected from the structure (if any) and minus any power removed by the beam (beam loading). In the photocathode rf gun beam loading is quite small (~ 5 MeV \cdot 1 nC = 5 mJ compared to ~ 5 J) and will be neglected here (one exception is in the "super-charge" cleaning in Section 6.1.1 where the beam carries away enough energy to empty the cavity). In this approximation, the power dissipated on the walls is related to the forward power by

$$P_w = \frac{4\beta}{(1+\beta)^2} P_f, \quad (2.37)$$

where here β is the coupling factor which, for an overcoupled cavity, is equal to the VSWR⁵ and P_f is the forward power. Substituting eq. (2.33) into eq. (2.37), the Voltage gain is given in terms of the forward power, the shunt impedance and the coupling factor as

$$V = \frac{\sqrt{8\beta P_f R_s}}{1+\beta}. \quad (2.38)$$

Or, with the measured coupling factor, $\beta = 1.5$, $E_0 \approx 37\sqrt{P_f}$ MV/m when P_f is given in MW such that just over 14 MW is required for a peak on axis field of 140 MV/m.

2.3 Single Particle Trajectories in the Absence of Acceleration

In the absence of acceleration the single particle trajectories are determined by beamline elements such as dipole magnets that are used to steer the beam and quadrupole magnets

⁵ $(1+r)/(1-r)$ where r is the "Voltage" reflection coefficient

that are used to focus the beam, and of course the drift spaces that connect them. The solution of the equations of motion for a single beam line element is expressed as a matrix [45, 46, 47] such that

$$\begin{pmatrix} x \\ x' \end{pmatrix} = \begin{pmatrix} A & B \\ C & D \end{pmatrix} \begin{pmatrix} x_0 \\ x'_0 \end{pmatrix}, \quad (2.39)$$

as is commonly done in conventional optics [48, 49]. Ref [45] gives transfer matrices for many commonly used beam line elements. The transfer matrix of cascaded elements is then simply obtained through matrix multiplication of the individual elements. Once a beam is sufficiently relativistic such that the self-forces can be neglected, we use this method to determine how the phase space ellipse (defined in Section 2.4.2 through the rms spotsizes and angle) of the beam evolves through the system. Appendix B discusses the mathematical conventions used for describing such an ellipse.

2.4 Electron Beam Characterization

2.4.1 Choice of Coordinate System

The natural choice of coordinate system for the photoinjector is a “cartesian” curvilinear system with the z axis following the nominal particle trajectory and the two transverse coordinates x and y are used (as opposed to polar coordinates) because dipole, quadrupole, and higher order beamline optics do not exhibit azimuthal symmetry. Even the rf gun and linac don’t exhibit azimuthal symmetry due to cavity penetrations (rf coupling slots, pump out ports, etc.) and thus have non-zero multipole field components (However, the current gun is designed to suppress these modes). Typically, the $x(y)$ axis is chosen to be the horizontal (vertical) plane reflecting the fact that most

quadrupoles are upright and most dipoles are oriented such that they bend the beam either left-right or up-down. A notable exception to this is in the full cell of the rf gun used in this experiment, that is mounted in such a way as the rf-coupling slot, pump-out port, and tuners are rotated 45° to the horizontal. This was chosen to allow the laser ports in the half cell (these are rotated 45° from the full cell penetrations) to be horizontal. This significantly eases the laser alignment for grazing incidence illumination of the cathode. This coordinate system assumes that the paraxial approximation holds ($p_z \gg \sqrt{p_x^2 + p_y^2}$) much as one does typically in conventional optics.

2.4.2 Phase Space and Emittance

A particle beam can be characterized by its density in the six dimensional phase space of position and canonical momentum— (x, p_x, y, p_y, z, p_z) . According to Liouville’s Theorem, the phase space density of a collection of non-interacting particles is constant in time if they are described by a time-independent Hamiltonian, i.e. the density occupied in phase space is a constant of motion. The normalized emittance of the sub-space, (x, p_x) , is defined as

$$\epsilon_{n,x} \equiv \Gamma^x / \pi m c. \quad (2.40)$$

Where Γ^x is the area the beam occupies in the (x, p_x) sub-space, m is the electron’s mass, and c is the speed of light.

Often the emittance is defined in terms of the rms-values,

$$\epsilon_{n,x}^{rms} \equiv \frac{1}{m c} \sqrt{\langle x^2 \rangle \langle p_x^2 \rangle - \langle x p_x \rangle^2}, \quad (2.41)$$

and similarly for y and z . In the paraxial limit, $(p_{x,y}/p_z \ll 1)$, the transverse emittance

can be written as

$$\epsilon_{n,x}^{rms} = \gamma\beta\sqrt{\langle x^2 \rangle \langle x'^2 \rangle - \langle x x' \rangle^2}, \quad (2.42)$$

where x' is the angle with respect to the z -axis (p_x/p_z), and $\sqrt{\langle x^2 \rangle \langle x'^2 \rangle - \langle x x' \rangle^2}$ is the geometrical emittance.

Evidently, the normalized emittance is related to the geometrical emittance by

$$\epsilon_{n,x} = \gamma_z \beta_z \epsilon_{geom}. \quad (2.43)$$

Unlike geometrical emittance, the normalized emittance is constant even under (uniform) acceleration (technically only the full six-dimensional phase space is constant). In fact, uniform longitudinal acceleration dampens the geometrical emittance of the beam; it increases p_z while keeping p_x constant.

So why define the normalized emittance? After all the geometrical emittance is typically what is measured, and it is what physically matters at the undulator or interaction point in a collider. The answer is simply that different beams at various energies can be compared without regard to a particular reference frame. The units of the normalized emittance are length, however, units of π mm-mrad will be used which stresses the geometrical significance of emittance.

The number of particles enclosed in $\epsilon_{n,x}^{rms}$ depends on the particle beam distribution. If the density distribution is Gaussian, for example, then $\pi\epsilon_{n,x}^{rms}$ is the area in which 39.3% of the beam is enclosed. While, on the other hand, if it is uniform then 78.5% of the beam is enclosed. This (as well as a myriad different definitions of emittance) can lead to confusion in comparing results.

In breaking up the phase space into three, two dimensional spaces, it is assumed that there is no correlation between the sub-spaces. This is not necessarily true. In

fact, the space-charge and non-linear rf forces on a finite beam are gross violators of this assumption as they couple the transverse and longitudinal phase spaces due to the longitudinal dependence of the radial fields and vice-versa. In addition, the solenoid couples the two transverse phase spaces by imparting a rotation on the beam. Skewed quadrupoles also couple the transverse phase space. In fact, the full cell of the gun itself mixes the transverse phase spaces as the symmetry of the full cell in the rf gun is rotated 45° with respect to the rest of the beam line. Nonetheless, the concepts of separate transverse and longitudinal phase spaces are valuable and they will be used along with the rms definitions for the emittance for characterizing a beam.

The (x, x') phase space, for example, can be described as an ellipse defined by the rms values of the particles angle and position

$$\beta x'^2 + 2\alpha x x' + \gamma x^2 = 1. \quad (2.44)$$

where α, β , and γ are known as the Twiss parameters. The three parameters are not independent as they satisfy the condition that $\beta\gamma - \alpha^2 = 1$.

It is customary to define a beam ellipse [47, 45, 46]

$$\sigma = \begin{pmatrix} \sigma_{11} & \sigma_{12} \\ \sigma_{12} & \sigma_{22} \end{pmatrix} = \epsilon \begin{pmatrix} \beta & -\alpha \\ -\alpha & \gamma \end{pmatrix}, \quad (2.45)$$

where ϵ is the geometrical emittance. The (x, x') phase space is then described as an ellipse given by the matrix equation,

$$\begin{pmatrix} x & x' \end{pmatrix} \sigma^{-1} \begin{pmatrix} x \\ x' \end{pmatrix} = 1. \quad (2.46)$$

The area of the ellipse is given by $\pi\epsilon_{geom} = \pi\sqrt{\det \sigma}$ such that

$$\epsilon = \pi\sqrt{\sigma_{11}\sigma_{22} - \sigma_{12}^2}. \quad (2.47)$$

Fig. 2.8 shows such an ellipse and Appendix B describes in more detail the mathematics involved in describing such an ellipse. The phase space ellipse transforms as

$$L\sigma L^T, \quad (2.48)$$

where L is the transformation matrix defined by eq. (2.39). The transformation of the phase space ellipse under quadrupole focusing will become the basis of the quadrupole scan used to determine the beam emittance (see Section 6.2.2).

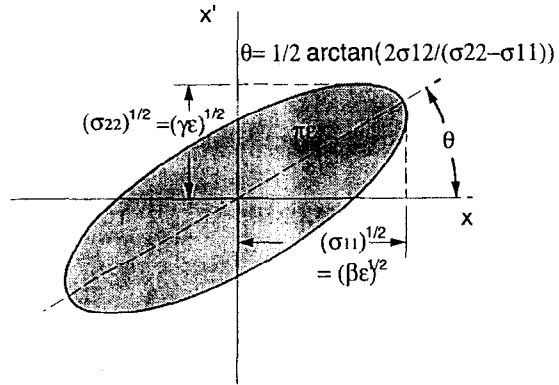


Figure 2.8: Phase space ellipse showing the rms beam size and divergence.

The emittance can only be decreased by non-conservative means such as filtering the beam at the expense of a loss of particles or through selective acceleration. However, the use of solenoidal—emittance-compensation—magnets can align the transverse phase space areas of various longitudinal segments in a beam with the effect of reducing the effective transverse emittance (time integrated or projected emittance) of the beam [8].

The emittance represents the volume of particles in phase space but not the number of particles. The beam brightness describes a beam in terms of both emittance and particle flux. The beam brightness B_n is often defined in terms of the emittance and the peak current I as

$$B_n \equiv \frac{I}{8\pi^2 \epsilon_{n,x} \epsilon_{n,y}}. \quad (2.49)$$

Other times an emittance is simply quoted along with the charge of the beam, for example, 1π mm-mrad with 1 nC.

There are many sources of a finite beam emittance. The ultimate is the quantum limit which comes from the Heisenberg uncertainty principle. Before this limit is reached there are many other factors to consider in producing a finite beam emittance. For the transverse emittance the mechanisms include the following: The thermal emittance comes from transverse momentum imparted the beam due to the excess between the photon energy and the work function in the photo-emission process. A finite longitudinal magnetic field on the cathode imparts an angular momentum that leads to a magnetic emittance term. Time dependent rf-focusing at the exit port of the rf gun leads to an rf emittance term. Multi-pole asymmetries give rise to transverse electric fields that cause an emittance increase. Space-charge causes a transverse emittance growth due to the electrostatic repulsion of the beam particles in their rest-frame. In the photocathode rf gun the emittance will be dominated by space-charge and non-linear rf forces with nearly everything which can be done to mitigate one worsens the other.

The longitudinal emittance terms include the energy spread of the electrons emitted from the cathode that gives rise to a longitudinal thermal emittance. The time dependent accelerating gradient gives rise to a (correlated) energy spread that can be made to compress the beam while space-charge forces act longitudinally to “blow apart” a beam.

2.4.3 Quantum Limit to Emittance

From the uncertainty principle, a particle's momentum and position cannot be known simultaneously with infinite precision. This leads to the normalized rms emittance of a single electron of

$$\epsilon_{n,x} = \frac{\hbar}{mc} \approx 4 \cdot 10^{-13} \text{ m}, \quad (2.50)$$

or the Compton wavelength of the electron. For the total 6D phase space the volume is given by

$$\Gamma_n = \left(\frac{\hbar}{\pi mc} \right)^3. \quad (2.51)$$

Thus, the minimum phase space volume can be constructed for N_{e^-} electrons as

$$\Gamma_n = \left(\frac{\hbar}{\pi mc} \right)^3 \frac{N_{e^-}}{2}, \quad (2.52)$$

where a factor of $\frac{1}{2}$ has been included to account for the two possible spin orientations for the electron (a spin $\frac{1}{2}$ particle). Thus the quantum limited rms emittance is given by,

$$\epsilon_{n,x} = \left(\frac{N_{e^-}}{2} \right)^{\frac{1}{3}} \frac{\hbar}{mc}. \quad (2.53)$$

A similar result is given in [50]. For 1 nC of charge ($N_{e^-} \sim 6 \cdot 10^9$), the emittance is then roughly $6 \cdot 10^{-4} \pi$ mm-mrad which is just over 3 orders of magnitude less than the LCLS design requirements.

2.4.4 Transverse Thermal Emittance

The transverse thermal emittance of the electron beam is defined by the product of the uncorrelated transverse momenta of the beam and the spotsize of the emitting area of

the cathode. It is essentially independent of charge and represents effectively the lowest achievable emittance directly from the source. In the case of the thermionic gun the emittance is determined by the size and the physical temperature of the cathode which is on the order of the work function of the cathode. However, in the photocathode gun, which is typically operated near room temperature, the physical temperature is quite small. The thermal emittance is then dominated by the effective temperature defined by the difference of the photon energy and the work function. This is typically on the order of a few tenths of an eV compared to room temperature which is about 1/40 eV.

In this section the upper limit on the transverse thermal emittance from a photocathode gun is estimated. The formalism is similar to reference [51] except most notably for the inclusion of the Fermi energy in the calculation. It is assumed that the typical electron is excited from the near the Fermi level. Since the temperature is small and the density of states is proportional to $\epsilon^{1/2}$, this is reasonable. Finally as in Section 2.1.4, inelastic scattering of the electrons in the bulk of the material is ignored.

Before emission, the energy of an excited electron in the bulk is $\epsilon_f + \hbar\omega$. Only electrons with longitudinal momenta satisfying,

$$\frac{p_z^2}{2m} > \Phi + \epsilon_f, \quad (2.54)$$

can escape (where Φ is the work function [eq. (2.9)]). The longitudinal momentum in the bulk is given by

$$p_z = p \cos \theta = \sqrt{2m(\hbar\omega + \epsilon_f)} \cos \theta, \quad (2.55)$$

where θ is the angle of the momenta with respect to the normal to the surface. The maximum angle at which an electron can be emitted is given by

$$\theta_{\max} = \arccos \sqrt{\frac{\Phi + \epsilon_f}{\hbar\omega + \epsilon_f}}. \quad (2.56)$$

For $\hbar\omega = 4.7$ eV, an applied field of $E_0 = 100$ MV/m, and a copper cathode with $\Phi_0 = 4.5$ eV and $\epsilon_f = 7$ eV, $\theta_{\max} \approx 12.9^\circ$.

The rms emittance in x is given by eq. (2.41)

$$\epsilon_{n,x} = \frac{1}{mc} \sqrt{\langle x^2 \rangle \langle p_x^2 \rangle - \langle xp_x \rangle^2}.$$

If the electrons are emitted isotropically and the electron beam is symmetric about its mean, then $\langle xp_x \rangle = 0$. The rms spotsize of the laser is given by σ_x for a Gaussian and $r/2$ for a uniform pulse, where r is the radius of the spot. The electrons will be emitted within a small angle given by eq. (2.56) with transverse momenta $p_x = p \sin \theta \cos \phi$, where θ is the angle with respect to the beam axis (z) and ϕ is the azimuthal angle. Again assuming that they are emitted isotropically, the rms x-momenta is

$$\begin{aligned} \langle p_x^2 \rangle^{\frac{1}{2}} &= \left(\frac{\int_0^{2\pi} \int_0^{\theta_{\max}} (p \sin \theta \cos \phi)^2 \sin \theta d\theta d\phi}{\int_0^{2\pi} \int_0^{\theta_{\max}} \sin \theta d\theta d\phi} \right)^{\frac{1}{2}} \\ &= \sqrt{2m(\hbar\omega - \Phi)} \frac{1}{\sqrt{3}} \left(\frac{2 + \cos^3 \theta_{\max} - 3 \cos \theta_{\max}}{2(1 - \cos \theta_{\max})} \right)^{\frac{1}{2}}, \end{aligned} \quad (2.57)$$

where $p = \sqrt{2m(\hbar\omega - \Phi)}$ after the particle escapes. The emittance is, then, given by

$$\epsilon_{n,x} = \sigma_x \sqrt{\frac{2}{mc^2} (\hbar\omega - \Phi)} \frac{1}{\sqrt{3}} \left(\frac{2 + \cos^3 \theta_{\max} - 3 \cos \theta_{\max}}{2(1 - \cos \theta_{\max})} \right)^{\frac{1}{2}}. \quad (2.58)$$

For $\hbar\omega = 4.7$ eV, $E_0 = 100$ MV/m, and a copper cathode with $\Phi_0 = 4.5$ eV and $\epsilon_f = 7$ eV, and $\sigma_x = 1$ mm, $\epsilon_{n,x} = 0.17 \pi$ mm-mrad. This will be a factor of two smaller if a uniform distribution were used.

In Section 6.1.2 the QE is measured as a function of the laser-gun phase ϕ_0 . Because the quantum efficiency depends on the electric field through the Schottky effect (eq. (2.13)) and the field at the cathode varies as $E_0 \sin(\phi_0)$, the QE is measured over a wide range by varying the laser injection phase. The data is then fit to obtain the difference between the laser energy and the work function from which the thermal emittance (at a particular field) is determined from eqs. (2.56) and (2.58).

2.4.5 Longitudinal Thermal Emittance and Uncorrelated Energy Spread

Using the same formalism as in Section 2.4.4 for the transverse thermal emittance, the longitudinal thermal emittance can be obtained utilizing the spread in the longitudinal momenta. Again it is assumed that all of the electrons are excited from the Fermi Level and that they do not undergo inelastic scattering in the bulk. The result is

$$\epsilon_{n,z} = \sigma_z \sqrt{\frac{(\hbar\omega - \Phi)}{2mc^2}} \frac{1}{\sqrt{3}} (1 - \cos \theta_{\max}) \quad (2.59)$$

where θ_{\max} is the maximum angle of emission (eq. (2.56)) which depends slowly on the difference between the work function and the photon energy. Again for $\hbar\omega = 4.7$ eV, $E_0 = 100$ MV/m, and a copper cathode with $\Phi_0 = 4.5$ eV and $\epsilon_f = 7$ eV, with $\sigma_z = 1.4$ mm (10 ps FWHM), $\epsilon_{n,z} = 0.015 \pi$ mm-mrad. This will be a factor of two smaller if a uniform longitudinal distribution were used.

The uncorrelated momentum (energy) spread is likewise given by

$$\frac{\sigma_{p_z}}{\langle p_z \rangle} = \frac{1}{\sqrt{3}\gamma} \frac{(1 - \cos \theta_{\max})^2}{(1 - \cos^2 \theta_{\max})}. \quad (2.60)$$

This corresponds to 0.7% spread at the gun when $\gamma = 1$ and will decrease as γ^{-1} during acceleration.

In addition to the uncorrelated energy spread there will be a correlated energy spread (chirp) due to the time dependence of the acceleration in the cavity and the finite extent of the beam. This energy spread leads to ballistic bunch compression (or expansion), or can be used in conjunction with future acceleration or magnetic chicanes to compress the beam and, if not compensated, can spoil the effective (projected) beam emittance.

2.4.6 Magnetic Emittance

Because the canonical momentum enters the definition of emittance, if the electron beam is emitted from the cathode with non-zero angular momentum (i.e., there exists a longitudinal magnetic field at the cathode), there will be a magnetic component to the transverse emittance. Thus, the emittance-compensation solenoid (because of its close proximity to the cathode see Section 3.1.2) will increase the emittance of the beam if the magnetic field at the cathode is not nulled with the use of a bucking coil.

If the magnetic field on axis at the cathode is given by B_z , the magnetic vector potential \vec{A} defined by $\vec{B} = \nabla \times \vec{A}$, is,

$$\vec{A} = \frac{B_z}{2} (y\hat{x} - x\hat{y}) \equiv A_x\hat{x} + A_y\hat{y} . \quad (2.61)$$

The x-component of the canonical momentum is

$$p_x = eA_x = e\frac{B_z}{2}y , \quad (2.62)$$

such that the magnetic contribution to the rms transverse emittance is

$$\begin{aligned} \epsilon_{rms,x} &= \frac{eB_z}{2mc} \sqrt{\langle x^2 \rangle \langle y^2 \rangle + \langle xy \rangle^2} \\ &= \frac{eB_z}{2mc} \sigma_x \sigma_y \quad \text{for } \langle xy \rangle = 0 . \end{aligned} \quad (2.63)$$

For an excitation current of 150 A the peak longitudinal field on axis in the solenoid is 2.24 kG with a field at the cathode of ~ 10 gauss. This would lead to a magnetic emittance term for a 1 mm Gaussian distribution of 0.29π mm-mrad. Because the magnetic emittance term depends on the beam area, the emittance will be reduced by a factor of four if a uniform transverse distribution were used.

2.4.7 Multipole Emittance

Dipole and higher fields in the rf gun can contribute to the transverse emittance of the beam by imparting a time-dependent transverse kick to the beam. This matter is further complicated since the solenoid field is rotating the beam as it passes through the structure. The dipole field is the dominant higher order mode with a value of $\sim 5 \cdot 10^{-5}$ of the TM_{010} mode for the prototype gun [38]. Ref. [38] gives an expression for the emittance term due to the dipole field as (altered to fit our conventions)

$$\epsilon_{x,rms}^{mp} = \frac{e}{mc^2} \sigma_x \sigma_z \int_0^L \frac{\partial E_z}{\partial x} dz , \quad (2.64)$$

where the solenoidal field has been ignored. From eq. (2.64), the emittance from the prototype gun was estimated to be $\epsilon_{x,rms}^{mp} \approx 0.15 \pi$ mm-mrad.

2.4.8 rf Emittance

The rf emittance due to the time dependence of the exit kick in the gun is calculated using the radial kick given in eq. (2.32), with the spotsize at the exit of the gun roughly the same as that at the cathode (ignoring space-charge and rf-focusing effects). The normalized emittance is again given by eq. (2.41),

$$\epsilon_{n,x} = \frac{1}{mc} \sqrt{\langle x^2 \rangle \langle p_x^2 \rangle - \langle xp_x \rangle^2} ,$$

where $p_x = mc\beta_x = \alpha k x \sin \phi$ (from eq. (2.32)). Therefore,

$$\epsilon_{n,x} = \langle x^2 \rangle \sqrt{\langle \sin^2 \phi \rangle - \langle \sin \phi \rangle^2} , \quad (2.65)$$

as given in ref [40]. The minimum emittance is therefore at an exit phase of $\pi/2$ (as expected since the time derivative of the field is zero when $\phi = \pi/2$). Operating away

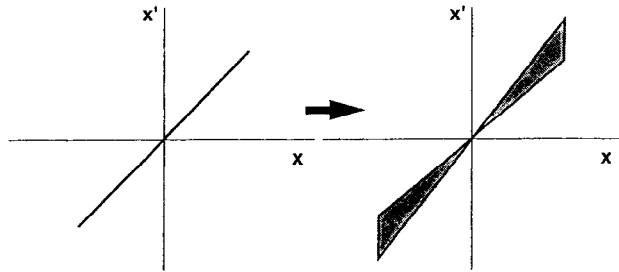


Figure 2.9: Phase space diagram showing emittance increase due to non-linear rf kick at the exit of a standing wave accelerator.

from the minimum gives,

$$\epsilon_{x,n} \approx \alpha k^2 \sigma_x^2 \sigma_z |\cos \phi_{\text{exit}}|, \quad (2.66)$$

where we assume that $k\sigma_z \ll 1$. Fig. 2.9 shows the effect of the time dependent exit kick on the (xx') beam phase space. The figure shows a “bow-tie” shaped phase space with non-zero area. In the absence of the rf emittance the phase space would be a straight line. The emittance increase is correlated and can in principle be removed with the correct phasing in future acceleration or in a bunch compressor. For an applied field of $E_0 = 100$ MV/m, $\alpha = 1.67$ and for a Gaussian longitudinal pulse with $\sigma_z = 1.4$ ps, a 1 mm transverse Gaussian, and an exit phase of 62° , $\epsilon_n = 3.9 \pi$ mm-mrad. This will be a factor of two smaller if a uniform distribution were used.

2.4.9 Space-charge Emittance

The effect of the self-fields (space-charge forces) of the electrons in the bunch can be quite destructive to the beam quality especially at low energies. The non-linear space-charge forces associated with a realistic beam cause the most damage. As it turns out,

the linear space-charge force acts essentially as a defocusing lens that only rotates the phase space.

The space-charge force tends to decrease as $1/\gamma^2$ at high energy because in the rest frame the longitudinal beam extent (and thus the density) is *decreased* by a factor of γ and the proper time is *decreased* by a factor of γ . Another way of saying this is that in the lab frame the focusing of the self-magnetic field tends to compensate for the defocusing of the electric field.

At relatively low energies, where the aspect ratio ($A = \sigma_x/\sigma_z$) of the beam in the rest frame is small, the difference in the space-charge forces between the edges of the beam and the core will become important. In this regime the reduction of the space-charge force will not yet decrease as $1/\gamma^2$.

In order to reduce the effects of space-charge emittance growth, one accelerates the beam rapidly to high energy. However, even with the high gradient photocathode guns additional acceleration is necessary and the damage due to the short time the particles are non-relativistic can be large. Emittance-compensation solenoids are employed that can remove the longitudinal correlation of the transverse emittance for linear forces. One therefore tries to produce a beam that minimizes the non-linear forces. One such attempt would be to produce a uniform beam in both space and time (although the edges of the beam still matter). In addition one wants a very low density pulse which means a large laser spot and long pulse length. However, these last two conditions would mean an increase in the rf-emittance as well as large energy spread. At some point, of course, these would also violate both the condition that $kr \ll 1$ and that $\tau < 1/f_{\text{rf}}$.

Fig. 2.10 shows the (xx') phase space evolution of a beam under the influence of space-charge. The phase space on the left shows the evolution of a beam (with finite emittance

shown) under the influence of perfectly linear space-charge forces while the phase space in the middle shows different longitudinal slices of the beam revolving at different rates leading to an increased projected emittance. Appropriate focusing of the beam could lead to the phase space ellipses again overlapping. In the non-linear case (on the right) there is no-longer just a rotation of the beam ellipse as it evolves but a distortion that manifests itself in a larger “effective” phase space volume.

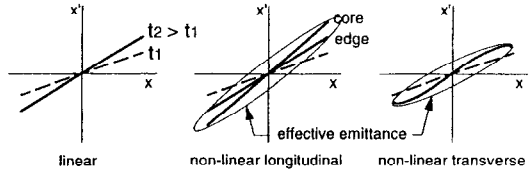


Figure 2.10: Phase space evolution under (from left to right) linear, non-linear longitudinal and non-linear transverse forces and transverse forces. The dotted line represents the initial phase space

The results derived in [40] are used to estimate the effect of space-charge on the beam emittance for both a Gaussian and uniform beam. Here the space-charge emittance term is given as

$$\epsilon_{n,x_i} = \frac{\pi}{4\alpha k \sin \phi_0} \frac{I}{I_A} \mu_{x_i}, \quad (2.67)$$

where x_i is either the transverse or longitudinal coordinate, $I_A = 4\pi\epsilon_0 mc^3/c \approx 17$ kA is the Alfvén current, and μ_{x_i} is a geometric form factor for the beam. For a Gaussian bunch, with aspect ratio A in the rest frame, the form factors become

$$\mu_x \approx \frac{1}{3A + 5} \quad (2.68)$$

$$\mu_z \approx \frac{1.1}{1 + 4.5A + 2.9A^2} \quad (2.69)$$

The form factors for a uniform distribution are also given in [40]. For an aspect ratio of 1 (for example a 1 mm beam with 7 ps FWHM pulse width) $\mu_x \approx \mu_z \approx 0.125$ for a Gaussian while for a uniform distribution this is reduced approximately a factor of 4 to $\mu_x \approx \mu_z \approx 0.03$ (see [40]). This is consistent with PARMELA[52] simulations which seem to show approximately a factor of two reduction of the emittance when replacing a Gaussian distribution with a uniform one in each of the longitudinal and transverse dimensions [53]. For an applied field of $E_0 = 100$ MV/m, $\alpha = 1.67$ and for a Gaussian longitudinal pulse with $\sigma_z = 1.4$ ps, a 1 mm transverse Gaussian, a peak current of 100 A (1 nC, 10 ps), and an initial phase of 50° , $\epsilon_n = 8.6 \pi$ mm-mrad. This will be a factor of two smaller if a uniform distribution were used.

2.4.10 Transverse Emittance Summary and Estimates

From the preceding discussions the various contributions to the transverse beam emittance are tabulated along with estimates for typical beam parameters for the 1.6 cell photocathode rf gun used in this thesis. Table 2.3 gives the relevant parameters, while Table 2.4 gives the scaling laws and emittance estimates. Each term and all symbols are defined in the text and assume no correlation between terms.

With the exception of the space-charge term all of the terms lead to smaller emittances when smaller beam dimensions are used. The space-charge and non-linear rf terms are the dominant sources of emittance. It can be seen for a fixed charge almost everything that can be done to mitigate one increases the other with two exceptions; one, by changing the beam distribution from Gaussian to Uniform, one can improve each emittance contribution, and two, by running closer to crest in the gun both the space-charge term will decrease (as the beam sees a higher field in the half cell) and the non-linear rf ef-

Table 2.3: Parameters used for emittance estimates.

E_0	100 MV/m
k	0.06 mm^{-1}
α	1.67
ϕ_0	50°
ϕ_{exit}	62°
$\tau(\sigma_z)$	10 ps (1.4 mm) FWHM(rms)
I	100 A
$\sigma_x = \sigma_y$	1 mm
B	10 Gauss

fects decreases (as the beam exits closer to $\phi = \pi/2$). However, both the space-charge and non-linear rf terms are correlated, and each can in principle be removed either with the solenoid (for linear correlations) or with appropriate phase and gradient in the linac. The thermal, and magnetic term are small compared to the other terms but suffer from the fact that they are uncorrelated. In addition, the effects of small scale enhancements on the thermal emittance could potentially be devastating but were ignored here. The extent of the effect of the multipole contribution for an improperly symmetrized cavity is given in [54] and was not explored here. Simulations show that for a 1 nC charge, a 9 ps Gaussian temporal and 1.4 mm $\sigma_{x,y}$ transverse electron beam with a peak electric field of 110 MV/m, a injection phase of $\phi_0 = 50^\circ$, and 10° ahead of crest in the linac (10 MV/m), gives 7.6π mm-mrad [55] for an emittance-compensation solenoid field of 2.1 kG.

Scaling the emittances above for higher gradient ($\alpha = 2.3$), and uniform longitudinal and temporal profiles, and phases approaching $\pi/2$ will give $\sim 1.2 \pi$ mm-mrad for the

Table 2.4: Emittance scaling and estimates for conditions given in Table 2.3

emittance term	scaling	$\epsilon_{n,rms}$ [π mm-mrad]
space-charge	$\propto \frac{I}{k\alpha \sin \phi_0} \mu_x$	$8.6^{a,b}$
non-linear rf	$\propto \alpha k^2 \sigma_x^2 \sigma_z \cos \phi_{exit}$	$3.9^{b,c}$
thermal	$\propto \sigma_x \sqrt{\hbar\omega - \Phi}$	0.17^a
magnetic	$\propto B \sigma_x \sigma_y$	0.29^c
multipole	$\propto \sigma_x \sigma_z \int \frac{\partial E_x}{\partial x} dz$	$0.15^{a,b,d}$

^a This will be reduced by a factor of 2 for replacing a Gaussian with a uniform transverse distribution.

^b This will be reduced by a factor of 2 for replacing a Gaussian with a uniform longitudinal distribution.

^c This will be reduced by a factor of 4 by replacing a Gaussian with a uniform transverse distribution.

^d from reference [38]

space-charge term and $\sim 0.3 \pi$ mm-mrad for the rf term. Simulations show that running the gun with similar conditions and 7 MV/m in the linac can achieve 1π mm-mrad (see Ref. [56]).

Chapter 3

Electron Injector

3.1 Electron Beam Line

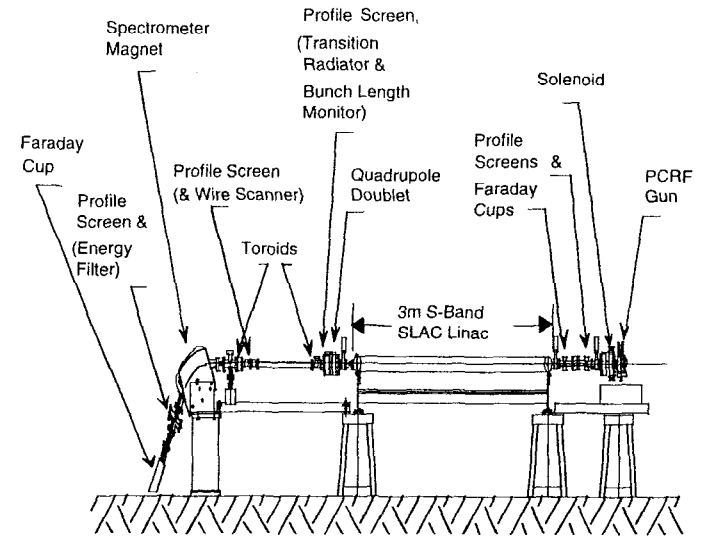


Figure 3.1: Schematic of the Gun Test Facility beam line.

The GTF electron beam line consists of a 1.6 cell photocathode rf gun, a ~ 2 kG emittance-compensation solenoid, a 3 m SLAC S-band linac section, as well as electron beam diagnostics. The diagnostics include instrumentation for measuring the geometric emittance, beam profile, beam charge, beam spectrum, and bunch length (Fig. 3.1). Because of the large amount of ionizing radiation typically present with a high energy accelerator, the entire beamline is shielded in a concrete bunker. Fig. 3.2 shows the layout of the Gun Test Facility which shares the enclosure with the injector for the Stanford Synchrotron Radiation Lab's synchrotron light source—SPEAR. The Klystrons are labeled K1 and K3 for the gun and linac klystron respectively (K2 is for the SPEAR

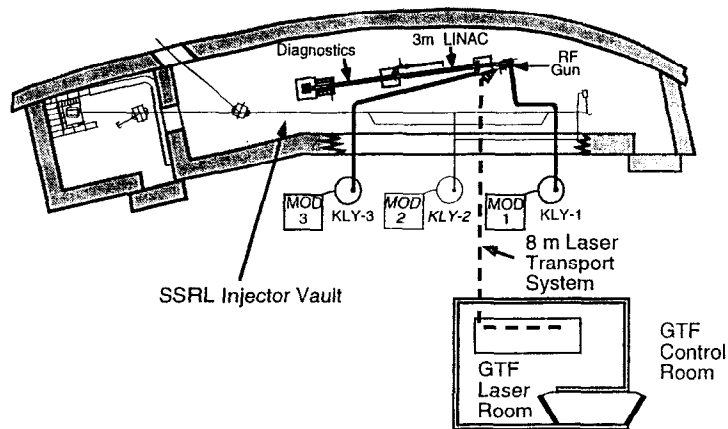


Figure 3.2: Plan view of the SLAC Gun Test Facility.

injector), and the Modulators are labeled Mod 1 and Mod 3. Also shown is the laser room and the control room.

3.1.1 Photocathode rf Gun

The electron source (photocathode rf gun) for the photo-injector is a standing wave room temperature copper structure consisting of two coupled rf cavities. It was designed to achieve peak electric fields on axis of $\sim 100 - 140$ MV/m. A schematic of the gun is shown in Figs. 3.3 and 3.4. The two schematics are rotated 45° with respect to one another to show the different cavity penetrations. Details about the design, construction and measurements on the prototype gun can be found in [38]. The gun used at the GTF is essentially the electrical equivalent of the prototype with small mechanical differences relating to the vacuum and rf joints and in the heat removal.

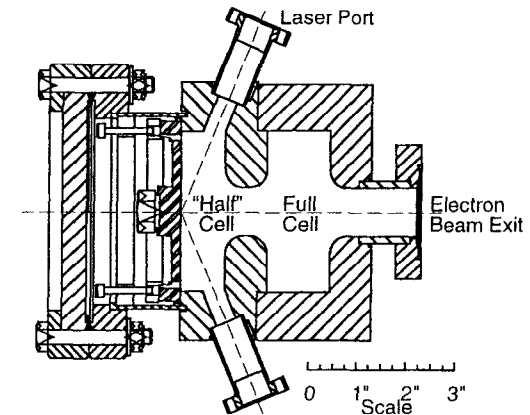


Figure 3.3: Schematic of the 1.6 cell photocathode gun showing symmetric laser ports in the "half cell".

The photocathode is copper and makes up the entire back wall of the gun as shown in Fig. 3.4. In this manner, the rf joint between the cathode and the rest of the gun has been moved to the outer walls of the gun where the electric fields are small. However, the outer walls are a region of high magnetic field such that a good rf connection is required because of the large surface currents. Cathode joints are notorious sites for rf breakdowns, and moving the cathode joint out to an area of low field enables higher fields to be stored in the gun.

The laser is incident on the cathode either at near normal incidence as shown in Fig. 3.5 or at near grazing incidence ($\sim 72^\circ$) through one of the laser ports in the "half cell". For most of the data presented here, normal incidence was used. Grazing incidence has the advantage that higher quantum efficiencies can be obtained, but requires corrections on the laser pulse for both a time shear in the amplitude front and ellipticity (see Appendix D).

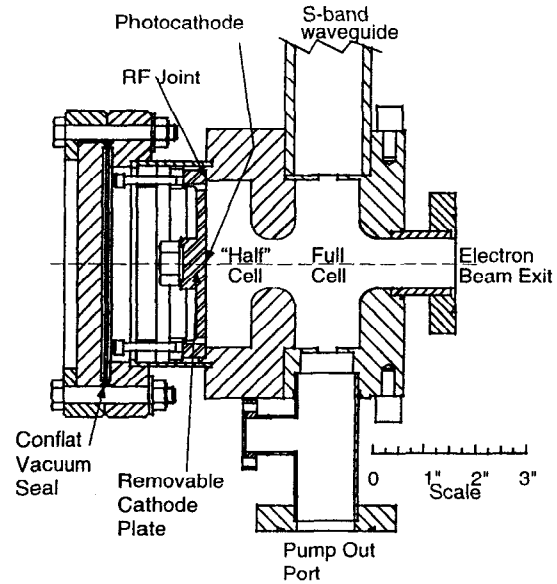


Figure 3.4: Schematic of the 1.6 cell photocathode gun showing waveguide feed and symmetric *pump-out* port.

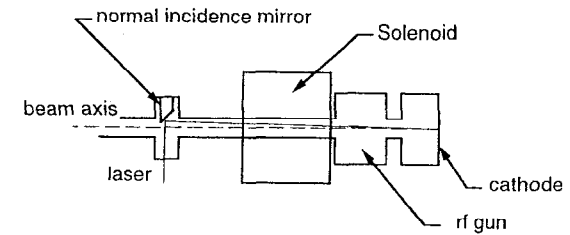


Figure 3.5: Schematic of the normal incidence geometry.

The accelerating mode of the gun is resonant at 2856 MHz ($\lambda \sim 10$ cm) which sets the overall scale of the structure. The first cavity is approximately 0.6 of an rf cell in length (where a cell is 1/2 of the microwave wavelength) while the second cavity is a full cell. The additional length of the "half cell" is included to provide improved rf-focusing during the transit time of the beam in the "half cell" [57] and requires that the resonant mode will consist not only of the TM_{010} mode, but will also include higher spatial harmonics along the cavity axis. The cavity design is symmetric with respect to all of the cavity penetrations which reduces the contribution of dipole and other undesirable higher order modes in the cavity [38].

Power is fed through a waveguide feed in the full cell while a 30 l/s ion pump provides pumping through the waveguide feed. A symmetric port opposite of the waveguide feed is used as a pumping port from which a second 30 l/s pump provides additional pumping. A vacuum of about $5 \cdot 10^{-10}$ Torr is maintained when rf power is not present and about $3 \cdot 10^{-9}$ Torr during operation. In addition to the pump, a capacitive pickup sits outside the gun in the pump-out port. The pickup is used to monitor the power in the gun. Power is coupled to the "half cell" through the beam iris separating the two cells. Because the system is coupled there will be two (lowest order) resonant modes in

the gun: the π mode where the electric field makes a π phase shift between cells and the 0 mode where there is no phase shift between cells. The desired mode for acceleration is the π mode, and thus, the gun is designed to have the π mode resonance coincide with the rf source. The 0 mode is avoided solely by a relatively large separation in the two resonances.

The tuning of the individual cavity frequencies is accomplished mechanically in the "half cell" by pushing on the cathode and with tuning shorts in the full cell. The fields are balanced (the peak field in the "half cell" is equal to the peak field in the full cell) by mapping the longitudinal field using a dielectric bead pull technique [58]. This occurs close to where the mode separation is minimum (technically this is where there are equal stored powers) [38]. The mode separation was measured to be 3.56 MHz using a network analyzer [59]. Small tuning in the resonance frequencies is obtained by changing the temperature of the cavities (and thus the dimensions) through water channels in the gun. The frequency shift due to temperature tuning is about 50 kHz per degree C for both modes [60]. In fact, the difference in the rf wavelength between room temperature at atmospheric pressure and vacuum require that the gun be heated to approximately 40°C for high power operation at the same resonance frequency. The water also serves to regulate the temperature of the gun.

3.1.2 Solenoid

A emittance-compensation solenoid sits immediately downstream of the rf gun. A detailed account of the simulation and design of the prototype magnet (in use at BNL) is given in [38]. The magnet is constructed out of eight copper "pancake" coils and uses 1006 steel flux returns and field straighteners to minimize dipole field contributions

(from the current leads and coil crossovers). The flux return also minimizes the field on axis at the cathode. The magnet is 20 cm in length and has a bore approximately 7 cm in diameter.

Solenoidal focusing is second order in the field, and is always focusing. It results from the angular velocity imparted to the particles in the beam from the fringe field at the entrance, and the resulting radial kick imparted by the longitudinal field in the magnet. The angular kick from the exiting fringe field will then remove the angular momentum imparted on the input if the beam energy is constant through the length of the solenoid. Section 2.4.6 discusses the effects of having a non-zero field at the cathode. Reference [41] gives, for the strength of the focusing,

$$f^{-1} = e^2 \frac{\int_{-\infty}^{\infty} B_z^2 / \gamma(z) dz}{4(\gamma)^2 m^2 c^2}, \quad (3.1)$$

which includes the effect of acceleration inside the solenoidal field. The beam as a whole will rotate about the solenoid axis; the rotation of the beam through the solenoid was $\sim 90^\circ$ for the typical experimental conditions.

Because the focusing depends on the fringe fields of the magnet, there will be an overall dipole kick to the beam if it traverses the magnet off center. The alignment of the gun to the solenoid was achieved mechanically. The mechanical centers of the two being within a few thousands of an inch from one another. In addition the gun body and the face of the solenoid are parallel to within about one mrad. Assuming that the electric axis of the gun and the magnetic axis of the solenoid coincide, the dipole kick can be used as a means of aligning the laser to the center of the cathode (see Section 6.1.1). In reality the laser was aligned to the axis defined by the combination of the solenoid and the gun.

The solenoid magnetic field was mapped for longitudinal and radial fields as a function

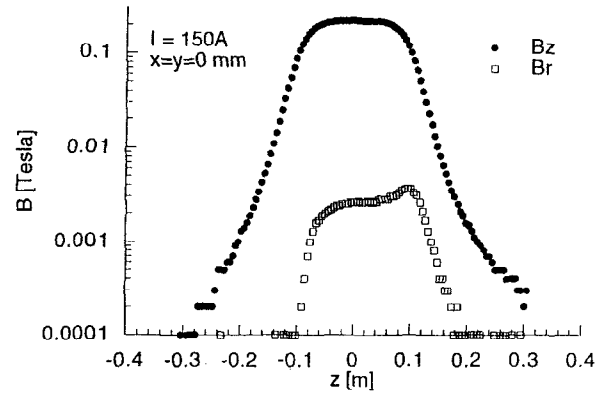


Figure 3.6: Magnetic field map (longitudinal and radial on axis) of the solenoid at an excitation current of 150 A.

of excitation current and on axis z position, for fields on axis, $x = y = 0$, and offsets of ± 5 mm in the x and y axis. The hysteresis was also measured. Measurements were performed by the SLAC magnetic measurements group using a Hall-effect probe. Fig. 3.6 shows the longitudinal (B_z) and radial (B_r) magnetic field of the solenoid on axis for 150 A. The cathode sits at $z = -0.2$ m. At 150 A The maximum longitudinal field is 0.224 T with a field at the cathode of 0.001 T (10 Gauss). The maximum radial field is $3.6 \cdot 10^{-3}$ T (36 Gauss). Because of the relatively low field at the cathode it was determined that the use of a bucking magnet to try and zero the cathode field was not necessary (see Section 2.4.6).

Fig. 3.7 shows the longitudinal field on axis at $z = 0$ versus excitation current and shows no sign of saturation for currents up to 220 A (~ 3.3 kG). The data were taken for 10 cycles of the current and Fig. 3.8 shows that hysteresis in the magnet is negligible.

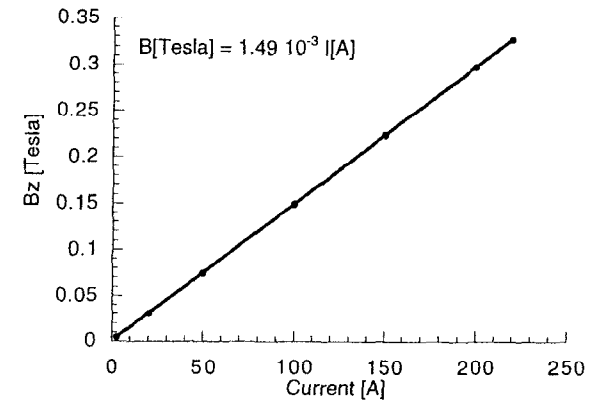


Figure 3.7: Longitudinal field on axis as a function of solenoid excitation current.

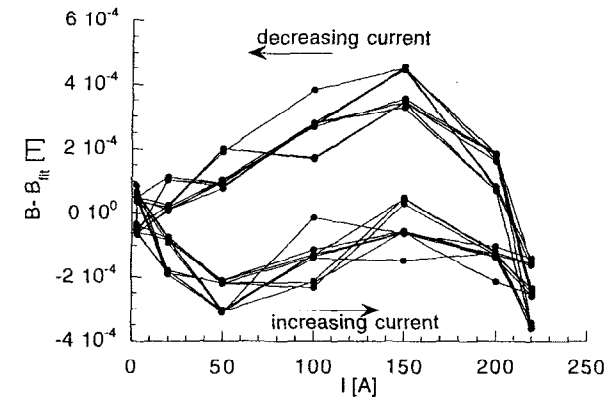


Figure 3.8: Hysteresis in the longitudinal field of the solenoid on axis.

3.1.3 Linac

The linac is a 3 m SLAC style traveling wave structure [61]. The structure is disk loaded to slow the phase-velocity down to the speed of light, such that a relativistic beam will stay in phase with the rf and can experience (essentially) the maximum net acceleration. However, the disk loading also slows down the energy transfer through the structure resulting in a group velocity less than the speed of light. About $\sim 70\%$ of the input power to the linac is lost on the walls of the structure. Because of this the size of the irises changes along the structure such that there is a constant accelerating gradient throughout the structure.

As was the case in the rf gun the input and output irises cause a radial kick on the beam (see Section 2.2.2). For phases appropriate for acceleration the input kick is focusing and the output kick is defocusing. At high energies, when the energy gain is small compared to the initial energy, the kicks are essentially compensating. However, in our case the opposite occurs: the energy gained in acceleration is much larger than the input energy the defocusing kick on the exit does not completely compensate the focusing kick on the entrance to the linac. The net result is a (time dependent) focusing of the beam that plays an important role in the emittance-compensation process [62].

The linac is fed power through a waveguide feed in the side of the first cell, and has a symmetric feed at the exit that is connected to a water cooled load. Because the feed breaks the cylindrical symmetry of the accelerator, it introduces higher order modes into the structure that are predominantly dipole. Unlike the rf gun the waveguide feed is not symmetrized and thus the dipole mode is not suppressed. The beam receives a transverse kick (horizontal) as it enters and exits the linac. At high energies this kick is essentially compensated, as in the focusing case, since the energy gain through the

structure is small compared to the total energy. However, in our case the input energy is ~ 5 MeV and the output is ~ 35 MeV and the net kick can be substantial. Dipole magnets at the input and output of the linac are typically used to reduce the effects of this kick. However, because physical constraints (the input and output coupler) require the magnets be placed approximately 1 foot from the input (output), the input beam to the linac needs to be pre-kicked in order to travel parallel and centered in the linac. No diagnostics were in place to measure the beam positioning in the linac (Beam position monitors are typically used). A combination of steering magnets in the low energy beam line and the dipole magnets on the entrance and exit of the linac were used to try and "cleanly" steer the beam through the linac; however, the method was quite subjective. Higher order mode analysis of the modes excited by the electron beam in passing through the cavity is perhaps the best method for steering the beam through the linac [63].

The electric field and thus the accelerating gradient in the linac depends on the power input to the linac and on the shunt impedance. For a SLAC 3m structure, the energy gain (for an electron on crest) is given by approximately $E[\text{MeV}] = 10\sqrt{P[\text{MW}]}$ [64]. Fig. 3.9 shows the power input to the linac, the power output to the load, as well as the capacitive probe in the gun for timing reference. The average group velocity is roughly $0.01c$ as deduced from the time delay between the input power and the load power ($3\text{ m}/1\mu\text{s}$). In addition, the $\sim 70\%$ loss in the power as the wave traverses the structure can be seen. In Fig. 3.9 the linac klystron's PFN is triggered at the same time as the gun's. The electron beam, which is launched at the peak of the power in the gun, will arrive at the linac just after the power in the front of the linac begins to decay. This is due to the fact that the Q of the linac is considerably lower than the Q of the gun (i.e. the fill time is much shorter) and the PFN pulse is relatively short ($\sim 2.5\mu\text{s}$). Because

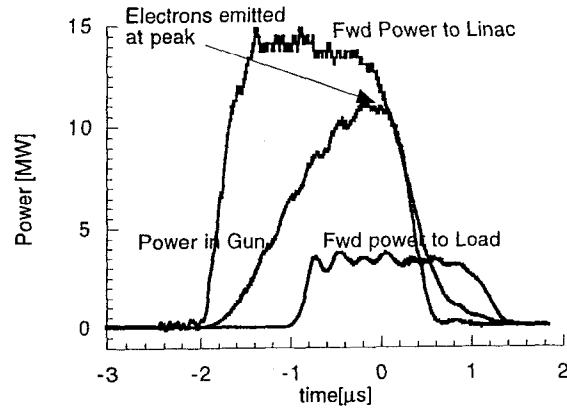


Figure 3.9: rf power in linac and load (with gun power for reference) before PFN delay.

there are separate klystrons for the gun and linac, it was easier to delay the PFN pulse from the linac klystron than it was to lengthen the pulse of the PFN. Fig. 3.10 shows the same rf waveforms as Fig. 3.9 when the linac PFN is delayed $\sim 1 \mu\text{s}$. In this case the delay is almost too much: the electron pulse arrives in the front of the linac before the power decays, but it arrives at the end of the linac almost before it fills. The delay was optimized by maximizing the beam energy out of the linac.

3.1.4 Quadrupoles

Quadrupole magnets (quads) are used for focusing charged particle beams (see for example [47, 46]). A perfect quadrupole will have pole faces shaped like hyperbolas such that the scalar magnetic potential is described by $\Phi_m = B_0xy/r_0$, where B_0 is the field at the pole tips (which for an electro-magnetic quad will depend on the excitation cur-

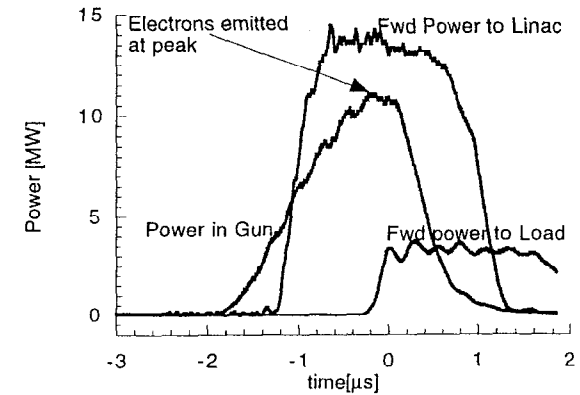


Figure 3.10: rf Power in linac and load (with gun power for reference) after PFN delay.

rent) and r_0 is the minimum distance of the pole tips to the center. The magnetic field from an *upright* quad (pole tips at 45 degrees) is then given by

$$B_x = B_0 \frac{y}{r_0}, \text{ and} \quad (3.2)$$

$$B_y = B_0 \frac{x}{r_0}. \quad (3.3)$$

When combined with the Lorentz force law, this leads to the 2 equations of motion:

$$x'' \pm K^2 x = 0, \text{ and} \quad (3.4)$$

$$y'' \mp K^2 y = 0, \quad (3.5)$$

where $K^2 = \frac{qB_0}{r_0 p}$ (where p is the particles momentum and q is the charge). The solution to the above equations gives one focusing and one defocusing plane for the quadrupole. For a quadrupole with an effective magnetic length l_{eff} the solutions to the equations

of motion can be written as the transfer matrix (see Section 2.3),

$$\begin{pmatrix} \cos Kl_{\text{eff}} & \frac{1}{K} \sin Kl_{\text{eff}} \\ -K \sin Kl_{\text{eff}} & \cos Kl_{\text{eff}} \end{pmatrix}, \quad (3.6)$$

for the focusing plane and

$$\begin{pmatrix} \cosh Kl_{\text{eff}} & -\frac{1}{K} \sinh Kl_{\text{eff}} \\ K \sinh Kl_{\text{eff}} & \cosh Kl_{\text{eff}} \end{pmatrix}, \quad (3.7)$$

for the defocusing plane [45]. Or in the thin lens approximation,

$$\begin{pmatrix} 1 & 0 \\ -\frac{1}{f} & 1 \end{pmatrix}, \quad (3.8)$$

and

$$\begin{pmatrix} 1 & 0 \\ \frac{1}{f} & 1 \end{pmatrix}, \quad (3.9)$$

where $1/f = K^2 l_{\text{eff}}$ is the focal length.

While one quadrupole is focusing in one plane and defocusing in the other, a combination of 2 quadrupoles (rotated 90° and separated by a short distance) can be used to focus the beam in both planes. Such a quadrupole doublet is used to focus the beam after the linac. The location of the quadrupole doublet can be seen in Fig. 3.1. By varying the excitation current in one of the quadrupoles, the effective focal length is varied (and thus the spot size of the beam on a screen down stream of the quads is also varied). This will be the basis of a *quadrupole scan* and is used to measure the emittance of the beam as reported in Section 6.2.

Because the focusing strength is momentum dependent the quadrupole is not, by nature, an achromatic lens; however, because our energy spread is small, $\delta E/E < 10^{-2}$, this results in a small aberration and is neglected.

3.1.5 BeamLine Diagnostics

Beam Profile Monitors

Profile screens are perhaps the most important diagnostic of the electron beam. A typical screen consists of a phosphorescent material that emits visible light when struck by an electron beam (like the phosphor on an analog oscilloscope or CRT based television). The fluorescence is then imaged onto a video camera and the physical beam can be seen and the beam spotsize and relative position can be determined.

The beamline has five phosphor screens as seen in Fig. 3.1: two screens between the solenoid and the linac, two screens between the linac and the spectrometer magnet, and one screen after the spectrometer magnet. The phosphor screen material was SLAC-chromate [65] which is very robust and quite linear. Because the screen intercepts the beam, the measurement is typically destructive to the beam. Therefore all of our phosphor screens were removable from the beam line. The low energy phosphor screens are oriented normal to the beam and the light is reflected off a 45° mirror through a vacuum window to a camera while the high energy screens are rotated 45° in the vertical plane and viewed directly through a vacuum window.

In addition, to the phosphor screens fluorescence from a YAG screen after the linac could be used. The YAG screen has the advantage that it has a very high dynamic range and produces considerable amounts of light as compared to a standard phosphor screen [66]; however, the combination of the thickness of the screen and the 45° angle made the resolution (in the vertical plane) poorer than the smallest spots during a typical emittance measurement and thus the YAG screen was not used.

A transition radiator which consisted of a piece of Aluminum foil can also be used as

a beam profile screen. It has the advantage that the emission is prompt and is planned for use in time resolved emittance measurements using a streak camera (as was done in [67]). Other time resolved measurements have used Thomson scattering of a short laser pulse [68], or a combination of chirping and filtering the beam [69].

Finally a wire scanner after the quadrupole doublet can be used to measure the beam spot size. The resolution can be made better than the typical phosphor screen/camera combination; however, since this requires scanning a wire across the beam, it is not a single shot measurement, and this method was not used.

Faraday Cups

Faraday cups can be used to directly measure beam charge. A simple Faraday cup consists of a block of metal insulated from the beam line. It is a capacitor which charges up with the beam current. The Faraday cup is discharged through a known resistance to ground, and the signal is integrated to yield the beam charge,

$$Q = \int \frac{V}{R} dt. \quad (3.10)$$

The GTF beamline contains three Faraday cups for measuring the beam charge. There is a Faraday cup at the end of the beamline after the spectrometer magnet (FC3) which is a copper block with re-entrant design, and two Faraday cups in the low energy section (FC1 and FC2) which can be remotely inserted or removed from the beam (Fig. 3.1). FC1 and FC2 further also serve as beam profile monitors in the low energy beamline [70]. The cups consist of a SLAC chromate screen at normal incidence with a stainless steel Faraday cup polished at a 45° angle. The Faraday cup doubles as a mirror to reflect the light from the phosphor screen through a vacuum window mounted on one flange of a four-way cross to a video-camera for beam viewing.

The Faraday cup signal is connected through a vacuum feed-through to a ~100 ft RG-223 coaxial cable to the GTF control room for readout on an oscilloscope. The capacitance of the Faraday cups is estimated to be a few pF such that, when combined with the low resistance connection to the cable, the signal contains considerable high frequency components. Large dielectric losses in the cable for high frequencies contribute to an error in measuring the beam charge. For this reason, a low pass filter is installed after the cup (~50 MHz) to ensure that an accurate charge measurement is made (see Fig. 3.11). Since there is no direct path to ground except through the 50 Ω input impedance of the scope all of the charge (collected by the cup) is seen by the scope—i.e., the correct charge is measured. In practice the 20 MHz low pass filter of the scope was also used to minimize overshoot.

In order to determine if the cups are collecting all of the charge, the range, of the electrons in the Faraday cup is estimated. Feather's expression [32] gives the range in g/cm² of aluminum,

$$R = 0.543E - 0.160 \quad E > 0.8\text{MeV}, \quad (3.11)$$

which is valid for ranges much less than the radiation length (i.e., for low enough energy particles). A 6 MeV electron would travel only ~1.1 cm in Aluminum (density = 2.7 g/cm³) compared to its radiation length of 24 g/cm² or 8.9 cm [71] and the thickness at the center of the Faraday cup of ~1.6 cm. Because the Faraday cups are made primarily of iron (which has a density of ~8 g/cm³), their range will be even shorter, and the collection efficiency is essentially a 100%. This was confirmed experimentally by looking at the signal from the downstream Faraday cup (FC2) while the upstream cup (FC1) intercepted the beam.

The "pop-in" Faraday cups were used extensively in characterizing the gun before ac-

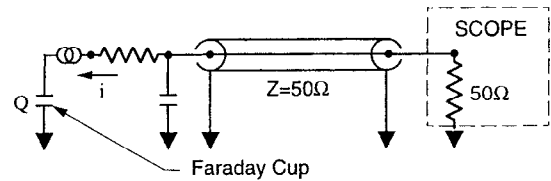


Figure 3.11: Faraday cup connection: circuit equivalent.

celeration; however, for emittance measurements (after acceleration) a toroid, or the laser energy, was used for a beam charge monitor, since the high energy beam profile screens prevented the use of FC3.

Toroids

For non-destructive beam charge measurements toroids (Fast current transformers) are often used. A typical toroid design consists of a ceramic break in the beam line (to interrupt the image current) surrounded by a Ferrite toroid with a number of turns of conductor wrapped around it. Fig. 3.12 shows a schematic of a beam toroid. The toroid acts as a transformer with the beam serving as the primary. An electrostatic shield encloses the toroid which has the effect of both shielding the toroid from external noise and producing a low Q cavity. The toroid is essentially a Voltage source while the Faraday cup is a current source. This means that care must be taken in interpreting the toroid signal. For example, the calibration will change with different bandpass filters or even cables. The toroids can also exhibit saturation effects due to the ferrite. The saturation level will be lowered in the presence of DC field (for example from being located too close to the solenoid or a quad).

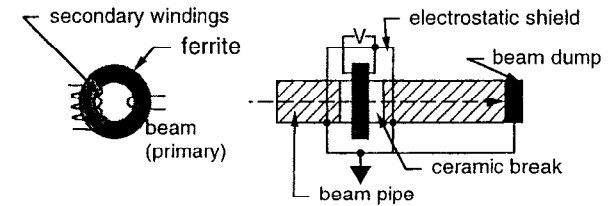


Figure 3.12: Schematic of a beam toroid.

A number of different Toroids were used at the GTF; their locations are shown in Fig. 3.1. Three SSRL style toroids were used as average current monitors for ionizing radiation safety considerations (ACM 1-3) and two diagnostic toroids—one located in the low energy beam line [72] and the other in the high energy line [73]. Due to observed saturation characteristics with bunch length, the toroids were typically only used as a current monitor when non-destructive means (a Faraday cup) could not be employed.

Chapter 4

Drive Laser

4.1 Gun Drive Laser Requirements

The requirements on the drive laser for the photoinjector [74] are determined primarily by the frequency of the rf gun, the cathode material and the desired pulse structure (single pulse for the LCLS) and repetition rate of the machine.

The laser pulse must be short compared to the rf period such that the beam exits the gun with a well defined energy. The rf period for the accelerating frequency is approximately 350 ps with electrons being able to gain enough energy to escape the gun during approximately 90 ps. However, due to the low energy spread requirements a laser pulse on the order of 10 ps is desired. The actual pulse length will be a trade off between long pulses for lower beam densities (and thus a smaller space-charge force) and short pulses for smaller non-linear rf forces. The laser should, in fact, be capable of producing considerably shorter pulses in order to be able to control the longitudinal profile of the bunch (through the longitudinal shaping of the laser pulse). The rf period also sets the time scale for the relative timing jitter between the laser and the rf. The jitter should be less than the pulse length to keep the shot to shot energy jitter and energy spread low. Because the LCLS utilizes bunch compression, the correlated energy spread (chirp) must be constant in order to keep the bunch length constant at the undulator. This puts an even tighter requirement on the timing jitter.

Finally, the rf frequency determines the physical dimensions of the laser. The longitudinal electric field must be independent of the radial position across the laser spot. Again there is a trade off between the beam density and the non-linear rf forces. For the S-band gun the spotsize should be on the order of one millimeter in radius. All of these requirements will scale inversely with the wavelength of the rf source.

The work function of the photocathode determines the frequency (wavelength) of the

laser. The laser photons must have sufficient energy to liberate the electrons from the cathode; however, not so much that the uncorrelated energy spread (thermal emittance) becomes too large. For most metals the work function requires UV photons. The quantum efficiency of the cathode will then determine the number of laser photons required to produce the desired charge. The quantum efficiency of metals is typically poor and depends greatly on the cathode preparation technique and cleanliness. For a copper cathode, the quantum efficiency is seldom better than $5 \cdot 10^{-5}$ electrons/photon for $\lambda \sim 250$ nm and the harsh environment of an rf gun. This requires approximately 0.1 mJ of laser energy to produce 1 nC of charge. In addition contingency for lower quantum efficiencies, transport losses, and losses due to transverse and longitudinal pulse shaping result in a requirement for considerably more laser energy.

The final requirement in determining the appropriate laser system is the repetition rate. This sets the average power required from the laser system as well as the heat removal requirements. Thermal properties of different laser materials vary greatly. The repetition rate of the Klystrons at the GTF is 10 Hz (set mainly by the modulator capabilities) which is much less than design rep-rate of 120 Hz for the LCLS. Consequently the GTF can utilize a laser with poorer thermal properties than the LCLS laser.

A frequency quadrupled chirped pulse amplification Nd:glass laser system was chosen for the GTF. Glass lasers have large energy storage capabilities and large bandwidths, however suffer from poor thermal properties [75]. A simple flashlamp pumped regenerative amplifier can produce several mJ of $\lambda \sim 1054$ nm light with enough bandwidth to support 0.5 ps pulses at a rep-rate of a few Hz. High quality non-linear optical crystals can then frequency quadruple the laser with overall efficiencies of about 25%. In this chapter we discuss the laser system which was constructed and used for the measurements reported in the thesis.

Table 4.1: Laser parameters.

Wavelength	1.054 μm quadrupled (0.263 μm)
Energy	2–3 mJ IR, (200–400 μJ UV)
Spot Size @ cathode	0.8 x 1.3 mm (rms Gaussian)
Pulse structure	Single pulse at 1.25 or 2.5 Hz
minimum pulse width	1 ps IR, 4 ps UV (FWHM Gaussian)
timing jitter w.r.t rf gun	<2.5 ps rms

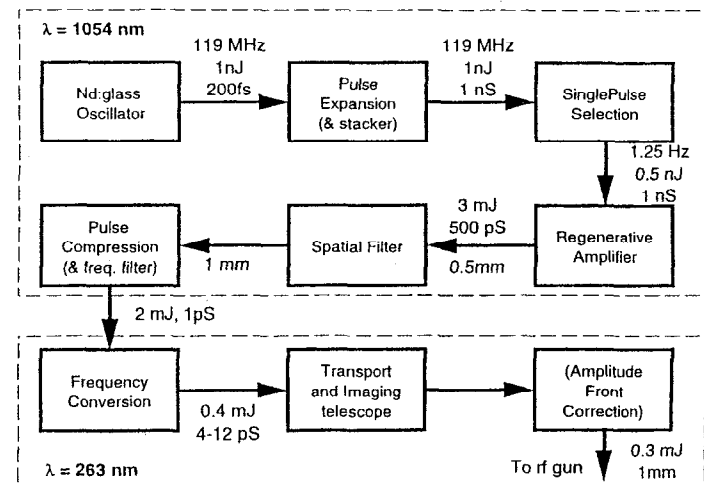


Figure 4.1: Block diagram of the gun drive laser.

Fig. 4.1 shows a block diagram of the GTF photocathode drive laser. The items in parentheses are components that are only used for pulse shaping or grazing incidence. The front end consists of a passively mode-locked, diode pumped, Nd:glass oscillator that produces ~ 200 fs transform limited pulses at 80 mW. The repetition rate of the oscillator is set by the cavity length and is roughly 119 MHz. This is the 24th sub-harmonic of the accelerating rf. The synchronization between the laser and the rf gun is then achieved by using a slow photo-diode (~ 120 MHz) to sample the pulse train from the laser oscillator and frequency multiplying the signal in a phase-locked multiplier [76] to generate the 2856 MHz master rf as described in Chapter 5.

The pulse train from the oscillator is chirped to ~ 270 ps/nm (up to 5 nm bandwidth) in a grating pair expander (to avoid non-linear effects in the amplifier), and then a single pulse is selected at 1.25 or 2.5 Hz for amplification in a Nd:glass regenerative amplifier. The amplified ~ 3 mJ, 1054 nm pulse is compressed to as short a pulse as ~ 1 ps (FWHM) using a grating pair with the opposite chirp of the expander. The pulse is frequency doubled and quadrupled in a 10 mm long KD*P and 5 mm long BBO crystal respectively to generate as much as ~ 500 μ J of 263 nm light (~ 4.7 eV photons). The UV pulse length is as short as ~ 4 ps FWHM, and the pulse is typically imaged onto the cathode at near normal incidence using an 8 m 1:1 telescope. Grazing incidence is also possible (and was used for the cleaning of the cathode) and requires additional correction optics for electron beam production (see Appendix D). Transverse shaping is accomplished by imaging an aperture, after the quadrupling crystal, onto the cathode. Table 4.1 gives typical achieved parameters of the laser system. The remainder of this chapter describes the laser system in more detail.

4.2 Chirped Pulse Amplification

The laser system is based on the technique of chirped pulse amplification (CPA) [29]. The laser required to drive the photocathode gun has a peak power on the order of 1 GW and intensities on the order of tens of GW/cm². These intensities are high enough that non-linear propagation effects occur in most materials. These effects can cause phase front distortion which lead to self-focusing, self-diffraction and other adverse effects on the beam, and at the very least provide a non-linear chirp (self phase modulation) which increases the pulse length (and increases the bandwidth) above the normal lengthening due to the linear dispersion (group velocity dispersion) of the material. These effects are most prominent during the amplification process where a large effective length of material is traversed (in our amplifier the total length traversed through the gain medium is approximately 40 meters). In CPA a frequency chirp (correlation between frequency and time) is imparted on the pulse to expand the pulse before amplification. This chirp is achieved by using a dispersive element such as a prism, optical fiber, or a diffraction grating. In this manner intensities are kept low during the amplification process. After amplification the pulse is then recompressed by imposing the opposite chirp on the beam. The beam should initially be chirped such that the total non-linear phase variations of the beam (the B-integral [48]) is roughly less than 2π .

4.3 Oscillator

The laser oscillator used at the GTF for most of the data presented in this thesis is a cw diode pumped Nd:glass oscillator [77]. The oscillator is passively mode-locked using a semiconductor saturable absorber mirror (SESAM) [78]. Because the oscillator is

passively mode-locked, the repetition rate is determined by the cavity length and was set to ~ 119 MHz (the 24th subharmonic of the 2856 MHz accelerator rf) for laser/rf timing.

The wavelength of the oscillator was tuned slightly off its gain center ($1.06\ \mu\text{m}$) to match the gain center of the regenerative amplifier ($\sim 1.054\ \mu\text{m}$) by use of an intra-cavity slit placed in the dispersion section between two group velocity dispersion (GVD) compensation prisms. These same prisms were adjusted to produce 5.7 nm bandwidth pulses. The pulse width was measured on a scanning autocorrelator [79, 80] to be 230 fs (which is approximately the bandwidth limited pulse width assuming a hyperbolic secant squared pulse [200 fs]).

The output of the oscillator is ~ 80 mW (~ 700 pJ/pulse) and was stable to $< 1\%$ p-p. A Galilean telescope after the oscillator is used to set the spot size (~ 2 mm $1/e^2$) and the collimation for injection into the expansion stage.

4.4 Pulse Expansion Stage

After the oscillator the pulse is temporally expanded in a grating pair expansion stage [81]. The geometry of the expander is shown in Fig. C.2. Appendix C calculates the chirp from the geometry used and discusses the design parameters. The chirp from the expansion stage is set at ~ 270 ps/nm and the bandwidth acceptance due to the finite size of the second grating is 5 nm causing some energy loss. However, due to significant gain narrowing in the amplifier (60 round trips through the gain media), the clipping is not a limiting factor in the final bandwidth of the amplified pulse.

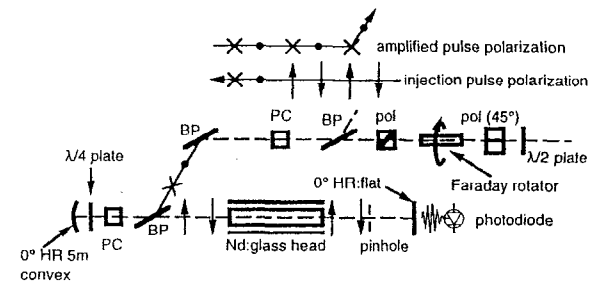


Figure 4.2: Schematic of the regenerative amplifier and injection stage.

4.5 Regenerative Amplifier

After expansion, a single ~ 0.5 nJ pulse of the 119 MHz pulse train is selected by a Pockels' cell (switched to $\lambda/2$ retardation) and a polarizer to seed the regenerative amplifier (regen) see Fig. 4.2. The regen uses a flash lamp pumped 1/4" diameter 6" long Nd:glass rod inside a half-symmetric resonator cavity. No mode matching of the oscillator to the regen is used. This makes the regen less sensitive to pointing jitter on the injection, but requires more power from the oscillator.

The cavity is Q-switched by use of a Pockels' cell, $\lambda/4$ plate, and thin film polarizer (Brewster plate). The Pockels' cell is aligned so that there is no retardation along the cavity axis when no Voltage is applied. The Q of the cavity is intentionally spoiled by rotating the polarization 90° on each pass, (by use of the $\lambda/4$ plate and curved mirror), until a suitable population inversion is produced inside the rod. This is timed to coincide with the seed pulse that is injected into the cavity by reflection off the (intra-cavity) Brewster plate. The pulse is then trapped in the cavity by stepping the Q-switch Pockels' cell to $\lambda/4$ retardation.

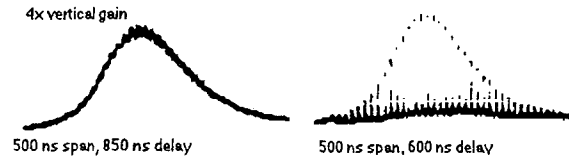


Figure 4.3: The Q-switch pulse inside the regen both with and without an injected pulse from the oscillator.

After approximately 60 passes, the seed pulse is amplified to ~ 3 mJ and the Q of the cavity is again spoiled, by stepping the Pockels' cell to $\lambda/2$ wave retardation, in order to "kick" the amplified pulse out of the regen. The amplified pulse is then switched out of the cavity off the Brewster plate. It travels along the same optical path as the input until it is picked off by another Brewster plate on the injection side of the injection Pockels' cell (which is now off: i.e. no retardation). A Faraday Isolator is also used before the injection Pockels' cell to avoid coupling any of the amplified pulse back into the oscillator. In addition, a $\lambda/2$ plate on the injection side of the isolator provides control of the amount of light injected into the regen.

The round trip time in the regen is ~ 12 ns as opposed to the 8.4 ns separation in the oscillator pulse train to aid in the system timing. A \sim GHz photodiode can easily resolve this difference, and one samples the pulse in the regen for use in setting the Pockels' cell timing (injection, Q-switch, and switch-out). Fig. 4.3 shows the regen pulse Q-switched with and without an injected pulse from the oscillator. The trace on the left is the Q-switched pulse and the trace on the right is with the injected pulse being amplified. The horizontal span is 500 ns and the Q-switched pulse is delayed 250 ns. In the injected case the pulse would normally be switched out of the cavity when it reaches saturation. Also the vertical gain on the Q-switched pulse is four times that of the injected pulse

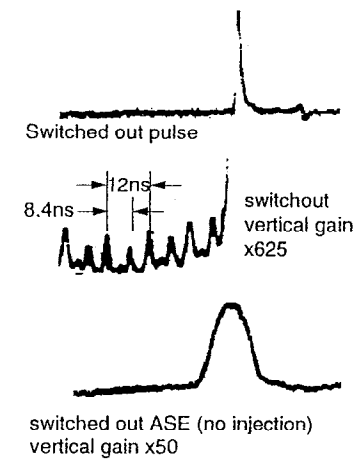


Figure 4.4: Regen contrast ratio. Top: The switched out pulse from the regen expanded and normal scale. Bottom: The switched out pulse from the regen and the switched out Q-switch pulse when no injection is present.

trace. When the oscillator pulse is injected the regen saturates much sooner than when starting up from spontaneous emission.

A photodiode can also be used to measure the contrast ratio of the pulses as shown in Fig. 4.4. The figure shows (top to bottom) the switched out amplified pulse (normal and expanded scale), and the switched out ASE (when no amplified pulse is present). The horizontal span is 100 ns and the vertical scale is magnified a factor of 625 in the upper trace and 50 in the lower trace. The contrast ratio between the main pulse and any pre- or post-pulses is in excess of 750:1. The switched-out pulse from amplified spontaneous emission (ASE) when no injection is present carries $< 15\%$ of the total energy

when the injection is present. When the injection is present the ASE is considerably reduced, and the background is almost entirely due to leakage from the cavity due to imperfect polarization optics.

The laser repetition rate was limited to 1.25 or 2.5 Hz due to thermal considerations in the Nd:glass laser rod [75]. At higher repetition rates thermal lensing prevents stable cavity operation of the regen. Before this limit is imposed, the regen shows stronger astigmatism possibly due to an increased thermal birefringence. No compensation for either thermal lensing or birefringence was used—other than limiting the repetition rate of the laser.

After amplification, the laser was spatially filtered in a 2:1 Newtonian telescope with a $600\ \mu\text{m}$ pinhole at the focal plane. The spatial filter is shown schematically in Fig. 4.5. The purpose of the spatial filter is to remove any high spatial frequency noise on the laser that may cause damage to the optics when the pulse is recompressed. The image in the focal plane of the laser is essentially the Fourier transform of the spatial frequency before the first lens. High frequency components focus to larger spot sizes and do not pass through the pinhole. The pinhole was chosen to be many times the diffraction limited spotsize of the TEM_{00} mode to avoid high frequency noise in the far field profile (due to diffraction from the pinhole) [48] as well as to avoid damage to the pinhole.

4.6 Pulse Compression Stage

After the beam is spatially filtered, it is then compressed in the double pass grating pair compressor [82]. The geometry is shown in Fig. C.1 and more details are given in Appendix C. The compressor is designed to have the same input and output angles

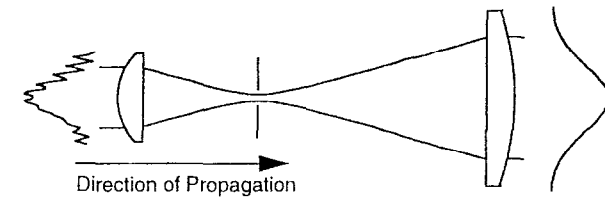


Figure 4.5: 2:1 Spatial filter

as the expander such that it imparts the exact opposite chirp of the expander. In this manner, in the absence of additional chirp imparted on the beam (for example due to non-linear effects in the regen), the compression completely undoes the expansion. The compression/expansion is to first order linear in the grating separation such that this symmetry is only necessary in trying to remove higher order, non-linear, chirp.

4.7 Frequency Conversion

The non-linear polarization of some materials (typically a uniaxial crystal) can be used to create harmonics from a high intensity electric field. This non-linearity is used to convert an infra-red pulse from the laser amplifier to an UV pulse capable of driving the copper cathode. The frequency conversion from the infra-red to the UV, fourth harmonic, is obtained by a two step process of doubling the infra-red to green utilizing one crystal and doubling the green to UV utilizing another.

The analysis of frequency conversion is relatively simple for long pulses even when saturation due to the depletion of the input is included [49]. Before depletion, the harmonic signal is proportional to the n^{th} power of the intensity (where n is the harmonic

number). For second harmonic production this signal is therefore proportional to the square of the intensity. For Gaussian pulse shapes, this non-linearity results in pulse lengths and transverse sizes decreasing by a factor of $\sqrt{2}$ at each step; however, once the crystals are run into saturation, both the pulse length and the transverse spot sizes will again lengthen.

For short pulses and large bandwidths frequency conversion becomes more complicated and simulations are typically required. Typically shorter crystals are required in order to avoid effects such as pulse lengthening due to the group velocity mismatch (and dispersion) between the fundamental and its harmonic. These effects also can alter the temporal profile of the harmonic pulse such that the infra-red pulse shape is not necessarily preserved (or even scaled) during the frequency conversion process. The doubling and quadrupling crystals used in producing the UV pulse are 10mm type II KD*P and 5mm type I BBO respectively. The doubling crystal is mounted with AR coated windows while the BBO is AR coated without windows. Fig. 4.6 shows doubling efficiency results as a function of input intensity. The results were taken using a fiber chirped Nd:YLF oscillator [83], before the Nd:glass oscillator was available. The intensity is inferred assuming a spot size at the crystal of $\sigma_{x,y} = 1$ mm and a pulse duration of 2 ps FWHM. The energy is read off with a Joule meter and is assumed to include $\sim 15\%$ background from ASE and pre- and post-pulses. An overall error in the intensity determination will expand or shrink the horizontal scale of the data with respect to the simulation. The simulations are from [84].

Fig. 4.7 shows the green and UV energy for various IR pulse lengths. The different pulse lengths were obtained by under-compressing the pulses in the compressor and were measured using a scanning autocorrelation technique. The green energy peaks near 10 ps. This is probably due to the group velocity walk-off effects and reconversion

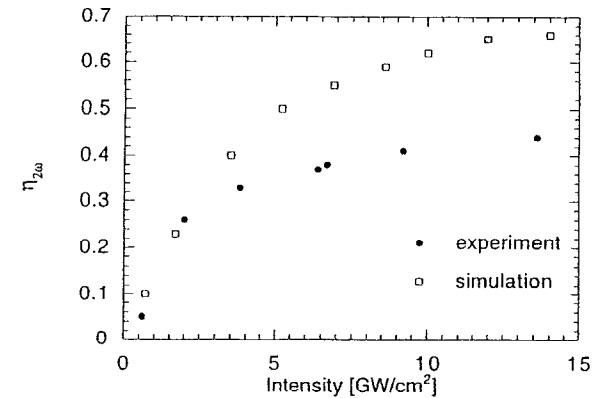


Figure 4.6: Frequency doubling efficiency for a 2 ps pulse through 1 cm thick KD*P. The circles are experimental results, and the diamonds are simulations.

limiting the conversion efficiency for shorter pulses in the KD*P crystal. Also shown in Fig. 4.7 is the efficiency in the conversion from green to UV light. Conversion efficiencies as high as $\sim 55\%$ have been obtained from the KD*P, and $\sim 45\%$ in the BBO (for the shorter pulse lengths) which have produced as much as $500 \mu\text{J}$ of UV light corresponding to an overall efficiency of 25%. Typically, however closer to $300 \mu\text{J}$ of UV was produced for delivery of up to $200 \mu\text{J}$ to the cathode.

4.8 Imaging and Transport System

The laser transport system used at the GTF is an evacuated ~ 8 m long 1:1 telescope (see Fig. 4.8). The transport is evacuated to avoid optical breakdown due to potentially large intensities at the focus. Because of the loose tolerances required, no adjustments were

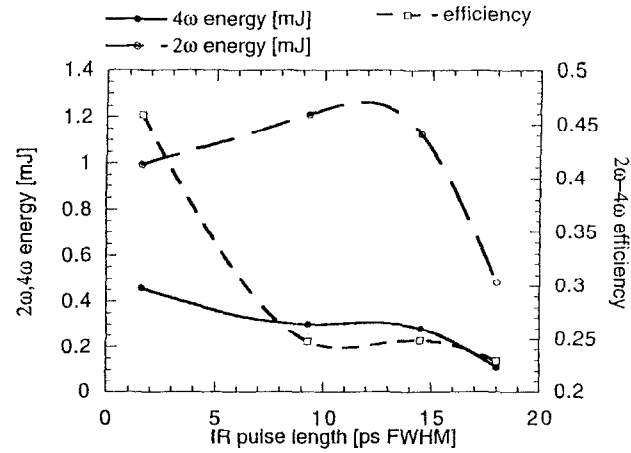


Figure 4.7: Green and UV yield and Green to UV efficiency vs. IR pulse length.

built into the system. The transport tube consists of several rigidly attached sections of 3" ID vacuum pipe with two, 4 m focal length, AR coated, UV grade fused silica lenses which also served as vacuum windows. A "tee" and vacuum valve allow for evacuation of the tube using an adsorption pump to a base pressure of ~ 1 mtorr. The pump was decoupled from the system after pumping to avoid coupling wall vibrations to the transport tube. The tube was evacuated *roughly* once every two months when the pressure had increased to ~ 1 Torr. The tube was evacuated to reduce turbulence effects and to prevent air breakdown at the focus for large input beams (small focus).

The advantage of using a telescope in the laser transport is that a location in the laser room can be imaged directly onto the cathode to help minimize both pointing jitter and diffraction effects. A telescope with two lenses f_1, f_2 separated by a distance $f_1 + f_2$

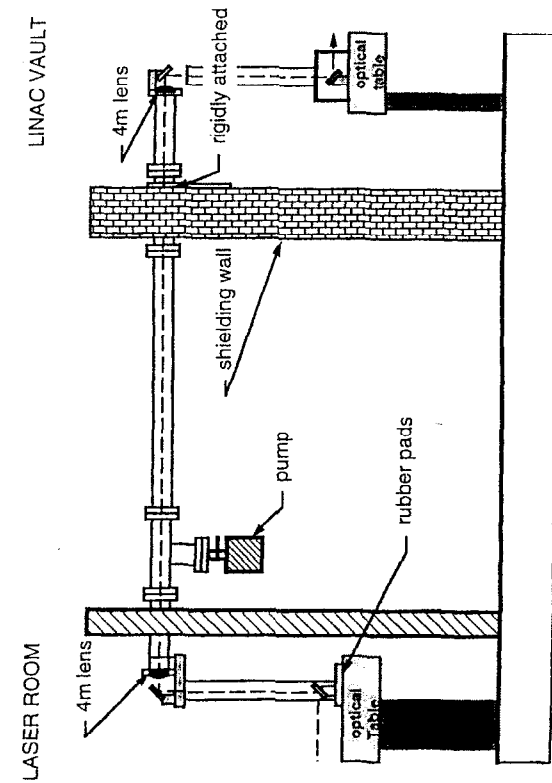


Figure 4.8: Schematic of the GTF laser transport system.

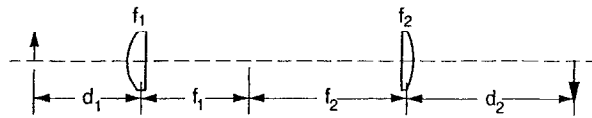


Figure 4.9: A simple telescope.

will image a point d_1 to d_2 (Fig. 4.9) according to

$$d_1 \frac{f_2}{f_1} + d_2 \frac{f_1}{f_2} = f_1 + f_2. \quad (4.1)$$

In the case of the 1:1 telescope ($f_1 = f_2 = f$) eq. (4.1) reduces to $d_1 + d_2 = 2f$. For the GTF, it was decided to use the symmetric case of $d_1 = d_2 = f$.

The transport tube is configured horizontally approximately 3 feet above the laser table. It is attached rigidly to the shielding wall in the linac vault, and is supported in the laser room with a 3" diameter aluminum stand. This stand sits on rubber vibration isolation pads to avoid coupling vibrations to the laser table. 2" diameter UV dielectric stack mirrors (with HeNe undercoats) are used for periscope mirrors on both the input and the output of the transport. The two output periscope mirror mounts are motorized for remote control from the GTF control room. Two quadrant diodes on the output of the transport sample a co-injected HeNe alignment laser if remote alignment is necessary. However, as long as the linac vault had reached thermal equilibrium, remote alignment was unnecessary.

Damage to the lenses of the transport tube, at fluences orders of magnitude less than the manufacture's reported damage threshold, led to replacement of the lenses on two occasions. The damage was discovered after transmission dropped and spatial distortions were noted on the beam. Eventually, the transport tube was disassembled, and it was found that the tube was not properly cleaned before installation. Damage to the

lenses was consistent with a thin layer of oil being deposited on the inside surface of the lenses. The transport tube was then cleaned as well as possible; however, some oil remained due to the fact that the spool piece that penetrates the linac vault could not be removed and had to be cleaned *in situ*. Therefore, it was decided not to evacuate the tube, but instead to backfill it with clean N_2 from liquid Nitrogen "boil off". The peak intensity at focus is roughly less than 10 GW/cm^2 which is an order of magnitude less than the estimated threshold for breakdown [85]. With the Nitrogen backfill, a ~5–10% attenuation of the laser energy through the transport was observed. Additional losses due to the input window, two pickoff wedges (for energy and spotsize diagnostics), and an Al mirror (the final mirror used for near normal incidence illumination of the cathode) gave an overall transmission of ~65%.

4.9 Longitudinal Pulse Shaping

Longitudinal pulse shaping of a short laser pulse can be accomplished using both time-domain and frequency-domain techniques. The emittance data presented in this thesis use a frequency domain technique to vary the pulse length from about 5 ps to 11 ps by varying the chirp in the compression stage. The pulses are approximately Gaussian for the shorter pulse lengths and become more flat top (with considerable structure) for longer pulse lengths. By altering the pulse spectrum nearly arbitrary pulse shapes can be made (within the bandwidth of the input pulse). A simple filtering of the pulse spectrum will be discussed which when combined with a linear chirp can provide near flat-top pulses.

In the time domain, a Michelson interferometer can be used to delay and recombine multiple pulses. Data from two pulse recombination is shown utilizing a low cost 50%

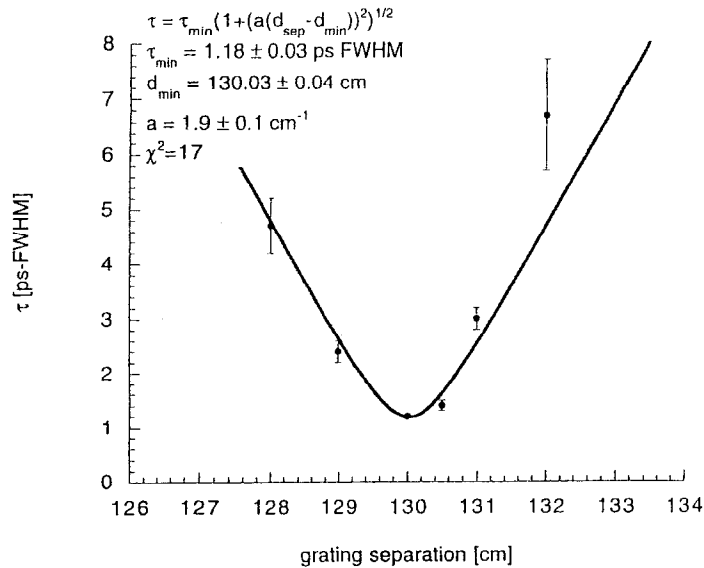


Figure 4.10: Autocorrelation measurements of the IR laser as a function of grating separation.

Fig. 4.10 shows the measured pulse width of the compressed amplifier pulse as a function of small changes in the grating separation in the compressor. By this manner, the best compensation for the expansion (and any other introduced chirp) is found. The fit is to a hyperbola as given by eq. (4.9). The corresponding minimum IR pulse width is approximately 1.2 ps. The pulse length was measured using a single-shot autocorrelator re-configured to be used as a scanning autocorrelator in order to improve the dynamic range. Since in an autocorrelation the details of the pulse shape are not uniquely determined, a Gaussian pulse is assumed. Error estimates are based on the error in the individual pulse width fits.

4.9.2 Pulse Shaping Utilizing the Chirp in the Compressor

Most of the data reported in this thesis were obtained with variable Gaussian temporal pulse widths by adjusting the chirp in the optical compressor. Pulse length measurements in the UV are plotted as a function of grating position as shown in Fig. 4.11. Pulses as short as 4.6 ps (FWHM) in the UV have been measured using a sub-picosecond resolution streak camera [86] and include $\sim 1\text{--}2$ ps/mm spatial chirp across the beam as can be seen in Fig. 4.12. This spatial chirp will be transferred to the electron beam and can lead to spatial correlations in both the non-linear rf and space-charge emittance contributions that can not be readily compensated. A grating scan was also performed with the green pulses and is given in Fig. 4.13. These pulses also show the spatial chirp. While in the interpretation of the autocorrelator data, a pulse shape must be assumed, the streak camera data give a *direct* measure of the pulse shape.

Fig. 4.14 shows a sample of 3 different UV pulses used in the emittance data presented in Section 6.2 along with Gaussian fits. The pulse on the left (8.2 ps) and the pulse in the middle (4.6 ps) are well described by Gaussian profiles; however, the pulse on the right (11.5 ps) shows considerable structure. This could be caused by a combination of the small bandwidth acceptance of the BBO crystal coupling with the relatively large residual chirp from the compressor similar to the effect shown in Fig. 4.15.

In addition, single shot autocorrelations [87] were performed in the green, but since the autocorrelation is not sensitive to spatial chirp, a shorter pulse duration of ~ 2 ps is measured. It is possible that the IR pulses carry this spatial chirp as well, and that it could come from a misalignment in the compressor. However, because the phosphor in the streak camera is not sensitive in the IR, no streak camera measurements of the IR pulses were made. An attempt at aligning the compressor by minimizing the astigmatism was made, but no significant improvement was seen.

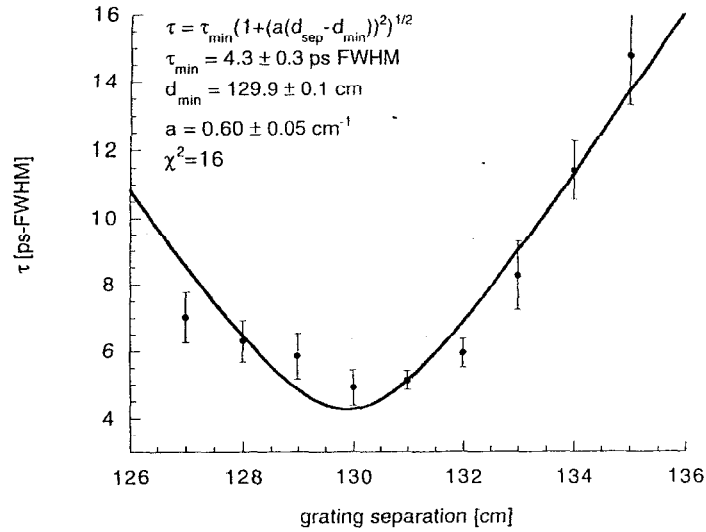


Figure 4.11: Streak camera measurements of the quadrupled laser as a function of grating separation.

4.9.3 Other Methods for Pulse Shaping

In order to obtain a more uniform temporal profile, two other methods of pulse shaping have been used at the GTF (in addition to adjusting the chirp in the expansion/compression stages). The first method involves spectral shaping in the compression stage to alter the Fourier transform (and thus the temporal shape) of the pulse. The other method uses a Michelson interferometer based pulse stacker (similar to the design in reference [88]) to temporally stack multiple pulses.

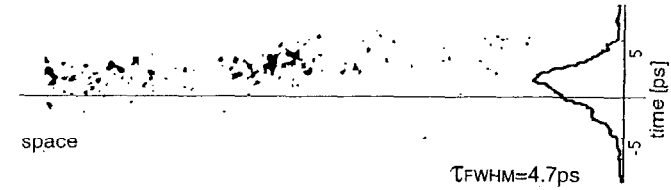


Figure 4.12: UV streak camera pulse showing 4.7 ps pulse with roughly 2 ps/mm spatial chirp.

Frequency Domain Pulse Shaping

Various elements can change the shape of a laser pulse by changing the spectral content or distribution of the pulse. These effects can either be caused by changing the phase (group velocity dispersion and self-phase modulation in a fiber, B-Integral effects in a laser amplifier, etc.) or amplitude (gain narrowing) components of the spectral distribution. One possible method to produce “arbitrary” pulse shapes (at least within the available bandwidth of the pulse) is to selectively filter the spectrum [89]. This could be accomplished by placing amplitude filters or masks within a dispersive element such as the expansion or compression gratings where spectral content is mapped to spatial content.

A simple amplitude mask in the compressor can produce near flat top pulses when combined with a residual chirp. The output pulse of a clipped Gaussian (spectral) pulse will be a convolution of the Fourier transform of the unclipped spectral (field) distribution with the Fourier transform of the aperture. Thus for a clipped Gaussian pulse, output field profile is a sinc ($\sin(\omega t)/\omega t$) convolved with a Gaussian,

$$E(t) \sim \int_{-\infty}^{\infty} e^{-(a-ib)T^2} \text{sinc} \frac{\omega_{\max}(t-T)}{\omega_{\max}} dT. \quad (4.11)$$

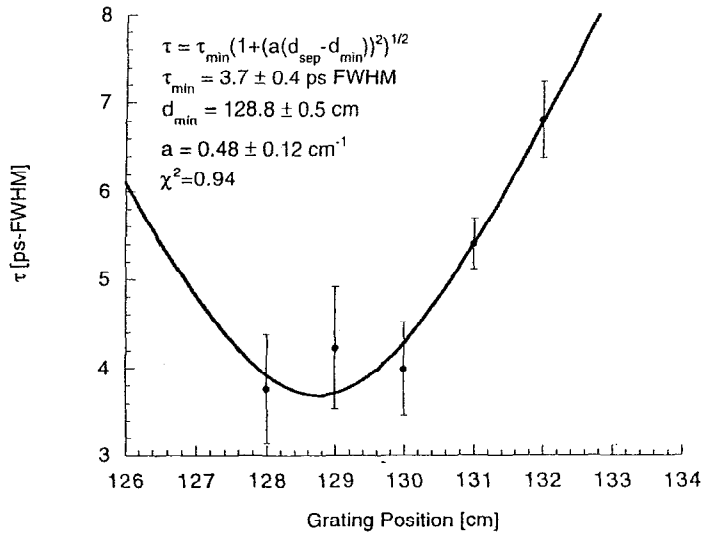


Figure 4.13: Streak camera measurements of the doubled laser as a function of grating separation.

Fig. 4.15 shows the (calculated) intensity pulse for a Gaussian pulse clipped at $\omega_{max} = 0.7 \cdot \omega_{FWHM}$ for both an unchirped and a chirped ($b/a=10$) pulse.

Temporal Pulse Stacker

A low cost 16 pulse Michelson interferometer based pulse stacker was constructed for use in the infra-red. A schematic of the pulse stacker is shown in Fig. 4.16 and is similar in design to ref. [88]. The pulse stacker works by varying the delay between successive pulses through the use of translation stages. The geometry allows for two output beams each of which has 50% of the input energy. A single beam-splitter is used both to keep

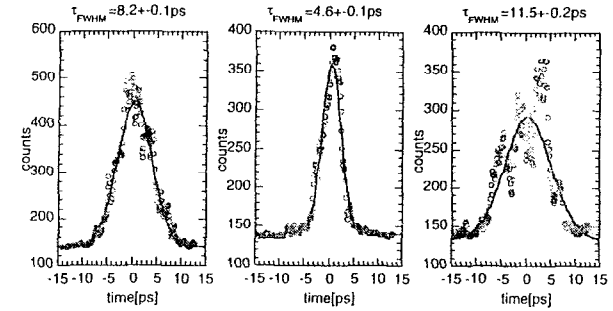


Figure 4.14: Sample streak camera data for the 3 different UV pulses with Gaussian fits. The different pulses lengths are obtained by varying the chirp in the compression stage.

costs down and to ease the alignment. Also, to ease alignment, 180° prisms are used to retro-reflect the beams. The pulse stacker was designed to go before the regenerative amplifier where the 50% losses can be tolerated. Also in this manner the tolerances on alignment are relaxed (because the input beam is not mode-matched to the regen cavity). The damage threshold of the optics also is not a limiting factor.

Because the electric fields of the individual pulses are added (not the intensities), interference effects are present in the output pulse shape. The combined electric field from two identical linearly chirped Gaussian pulses separated in time by T is

$$E_{tot}(t, T) = E_0 \left(e^{-(a-ib)t^2} e^{i\omega_0 t} + e^{-(a-ib)(t-T)^2} e^{i\omega_0(t-T)} \right). \quad (4.12)$$

Thus the intensity is

$$\begin{aligned} I_{tot}(t; T) &= \sqrt{\frac{\mu_0}{\epsilon_0}} E_{tot}(t; T) E_{tot}^*(t; T) \\ &= I(t) + I(t-T) + 2\sqrt{I(t)I(t-T)} \cos(\omega_0 T + bT^2 + 2btT) \\ &= I(t) + I(t-T) + 2\sqrt{I(t)I(t-T)} \cos(\phi_0 + 2btT), \end{aligned} \quad (4.13)$$

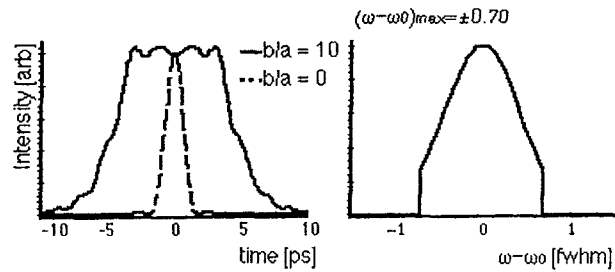


Figure 4.15: Calculated clipped Gaussian spectrum (intensity) and resulting temporal (intensity) profile for both a chirped ($b/a=10$) and unchirped ($b/a=0$) pulse.

where $I(t)$ is the intensity of the individual pulse in absence of the other pulse, and ϕ_0 is an overall *constant* phase term. For a transform limited pulse ($b=0$) the combined intensity will be the sum of the two intensities if $\phi_0 = (n + \frac{1}{2}) \frac{\pi}{2}$. Fig. 4.17 shows the addition of two pulses for various phases. The horizontal scale is normalized such that the FWHM value of the unchirped pulse is 1. In the unchirped case, when the separation is set to twice the rms value (σ), the phase can be set in order to get a flat top pulse with a rising edge comparable to the initial pulse. However, small changes in the phase result in a drastic change in the pulse shape. In order to keep the phase difference stable to even $\frac{\pi}{4}$ would require keeping the path length fixed to $\frac{\lambda}{8}$ or ~ 130 nm which is impractical at the current facility. However, if there is a residual chirp on the beam, the beating frequency of the interference is increased (as also shown in Fig. 4.17). The interference features are on the order of the single pulse transform limited width while the rising edge is also given approximately by the single pulse chirped width.

The pulse separation can be measured by using spectral interferometry [90]. The

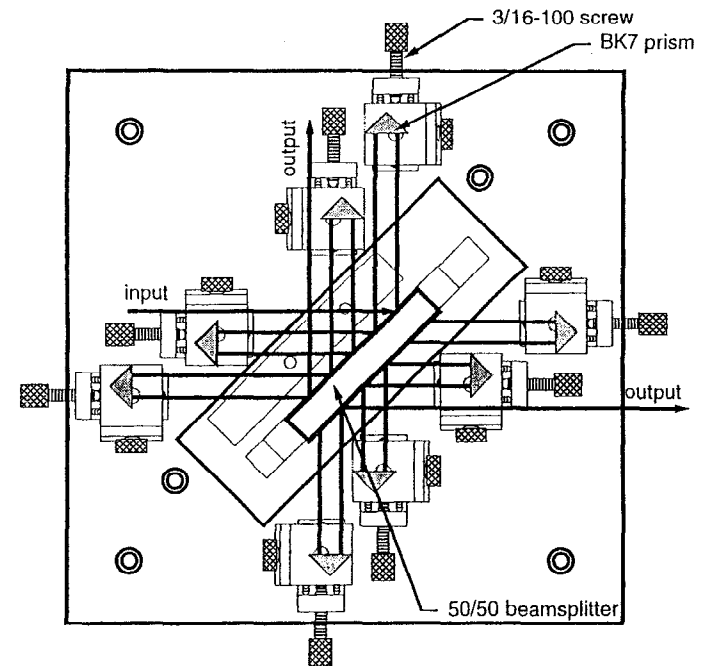


Figure 4.16: A schematic of the 16-pulse stacker. Translation stages with 100 threads per inch screws enable fine variations in the delay between pulses while a single beamsplitter and retro-reflectors ease alignment.

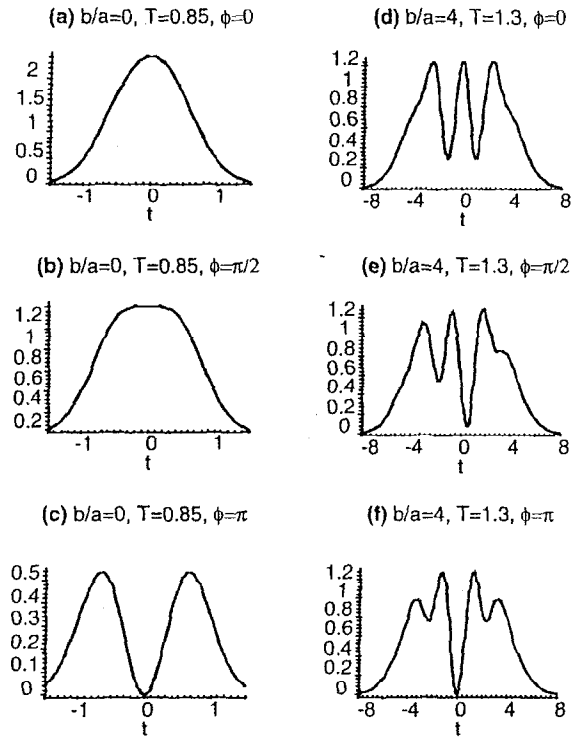


Figure 4.17: The calculated results of the interference between two pulses separated by approximately the single pulse duration in both an unchirped and 4 times chirped case. In the unchirped case (a-c) the pulses are separated by 2 sigmas, and in the chirped case (d-f) by 1.3 FWHM. The results are shown for various phases: $\phi_0 = 0$ (a,d), $\pi/2$ (b,e), and π (c, f).

spectrum of two identical pulses (with electric field given in eq. (4.12)), separated by a time, T , will exhibit interference fringes that depend on the pulse separation. The Fourier transform of eq. (4.12) is

$$E_{tot}(\omega; T) \sim \int_{-\infty}^{\infty} \left(e^{-(a-ib)t^2} e^{i\omega_0 t} + e^{-(a-ib)(t-T)^2} e^{i\omega_0(t-T)} \right) dt \\ \sim (1 + e^{i(\omega - \omega_0)T}) E(\omega), \quad (4.14)$$

where $E(\omega)$ is the Fourier transform of the single pulse (as given in eq. (4.5)) so that the power spectrum,

$$I_{tot}(\omega; T) = \sqrt{\frac{\mu_0}{\epsilon_0}} E_{tot}(\omega; T) E_{tot}^*(\omega; T) \\ = 2(1 + \cos((\omega - \omega_0)T)) I(\omega) \\ = \cos^2\left((\omega - \omega_0)\frac{T}{2}\right) I(\omega), \quad (4.15)$$

where $I(\omega)$ is the (intensity) spectrum of a single pulse, eq. (4.7). Thus, from the fringe spacing in the measured spectrum, the separation of the two pulses can be determined. This technique can be used even to measure the separation of pulses separated *in time* by more than their pulse durations (i.e. no temporal interference outside the spectrometer)—without violating the uncertainty principle. This is due to the fact that the spectrometer physically separates the pulses into their component frequencies such that the pulse is necessarily lengthened inside the spectrometer. The upper limit on the pulse separation is therefore given by the resolution of the spectrometer, while the lower limit is given by our ability to resolve a single fringe. Any chirp on the two pulses is canceled as long as they are identical. The data presented here was taken with the highly chirped pulse out of the expansion stage.

A commercial spectrometer [91] was used to measure the spectrum of the two pulses combined together in the temporal pulse stacker as described above. The pulses were

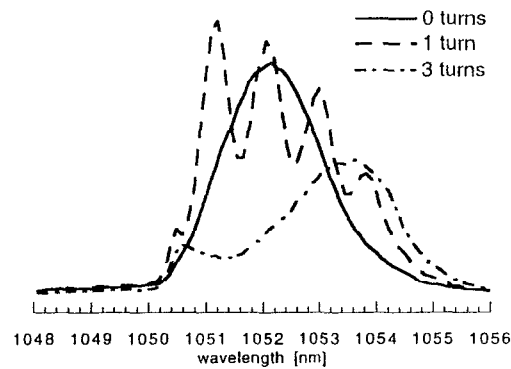


Figure 4.18: A sample of measured spectra for two pulses with different separations. The separation is given in turns of a 100 pitch screw.

pre-stretched in the expansion stage and therefore the spectrum is limited to the ~ 5 nm bandwidth limited by clipping of the spectrum in the expander. This technique was used to one, verify the pitch of the screws (100 threads/inch) in the translation stages, and two, to find the “zero” separation between the pulses. Fig. 4.18 shows a sample of three different measured spectra, while Fig. 4.19 shows the number of fringes as a function of the number of turns of the screw across the measured bandwidth (~ 3.7 nm). An error of $\pm \frac{1}{2}$ fringe is estimated and the bandwidth is assumed to be the same in all cases. Assuming the error in the bandwidth is 0.3 nm, then the number of thousandths of an inch (mil) per turn is given by $9.4 \pm 0.8 \pm 0.6$ mils/turn (The errors are from the estimated errors in the bandwidth and number of fringes respectively Figs. 4.18 and 4.19). This is consistent with the expected pitch of 10 mils/turn (about 1.5 ps/turn roundtrip) for a 100 pitch screw. Once the pitch was verified, the desired pulse separation was obtained by counting turns of the screw. It was later determined that the fiber that coupled the

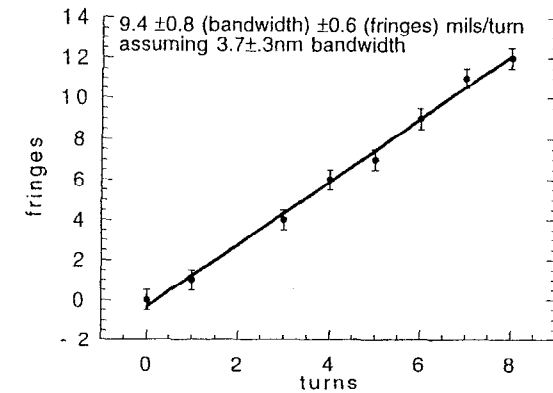


Figure 4.19: The number of fringes measured in the spectrum of two pulses stacked in the temporal pulse stacker versus pulse separation counted in turn of the adjustment screw. From this the pitch of the screw is calculated to be around 9.4 mils/turn.

light to the spectrometer was not a single mode fiber at 1054 nm (as specified). This could explain some of the problems seen in the spectrometer (changes in the spectral shape as the fiber was moved) as different modes will have different phase velocities in the fiber (and thus will result in multiple pulses interfering inside the spectrometer as a function of the length of the fiber and the total induced stress birefringence in the different modes).

The stacked pulses have also been amplified, recompressed, and frequency converted to the UV. Fig. 4.20 shows a sample of streak camera measurements made in the UV for various delays between 2 temporally stacked pulses. The pulse width of a single UV pulse is approximately 4 ps FWHM and significant interference can be seen until the separation approaches 3 FWHMs. The separation is estimated by counting turns with

respect to the 16 ps measured separation where negligible interference is shown as the spectrometer was not available during this measurement.

A conceptual design for an improved pulse stacker working in the UV has also been made (see Fig. 4.21). It allows for flat-top pulses by effectively adding the pulse intensities. This is accomplished by alternating the polarization of each successive pulse to be orthogonal to each of its nearest neighbors. This limits the interference to every other pulse and is negligible because of the long delay between these pulses. This design also allows for 100% throughput of the light from the pulse stacker by multiplexing the two output pulses. The alignment issues are alleviated by imaging the prisms onto the cathode. However, this scheme is not readily compatible with the grazing incidence design because the diffraction grating used for the spatial and temporal correction acts as a good polarizer (the p-polarization efficiency is considerably higher than the s-polarization efficiency). In principle, the relative strength of the two different polarizations could be adjusted to account for both the low efficiency of the grating for s-polarized light and the difference in the quantum efficiency for the different polarizations; however, this will lead to significant energy loss. It may seem that the easy solution would be to adjust the input polarization to the grating, such that the successive pulses have a net equivalent efficiency; this will result in a non-orthogonal polarization after the grating and thus interference between the pulses.

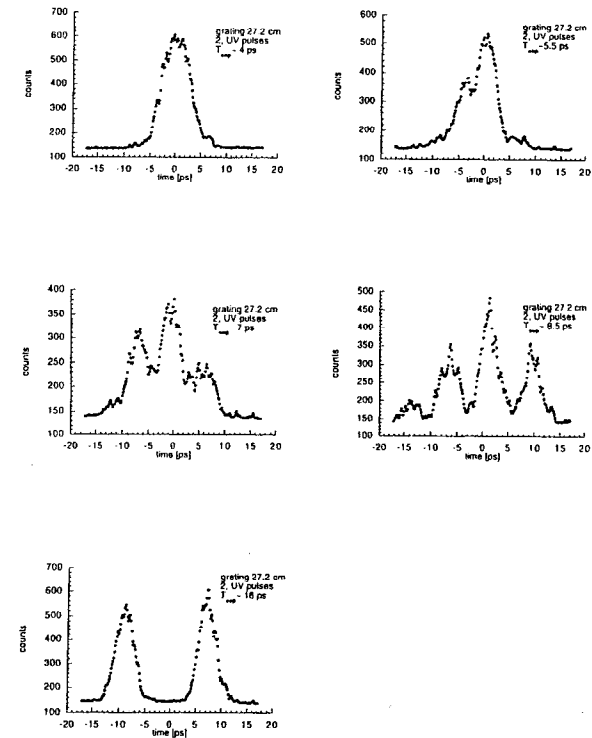


Figure 4.20: Measured UV pulse for two temporally stacked pulses for various pulse separations.

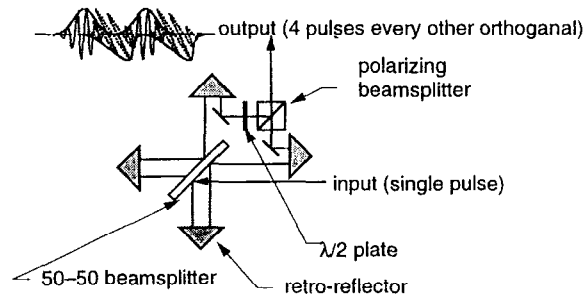


Figure 4.21: Schematic for 100% throughput UV pulse stacker with minimal interference.

Chapter 5

rf Systems and Timing Measurements

In this chapter we discuss the rf system that powers the gun and linac and present measurements of the relative phase jitter of the rf and a convolved measurement of the timing jitter between the single amplified laser pulse and the steady state phase in the rf gun.

Two high power klystrons power the gun and linac each capable of producing ~ 20 MW at 2856 MHz. This is enough power to achieve ~ 6 MeV acceleration from the gun and an additional ~ 45 MeV from the linac. In order to maintain a strict phase correspondence between the laser and the accelerating rf, the master rf is derived from an integer harmonic of the laser oscillator frequency. In this manner the relative phase between the laser and the gun can be maintained independently of laser timing jitter; the rf jitters in phase with the laser. There are some limits on how well the rf can follow the laser which will be discussed.

The effect of the jitter depends on its source as well as on the operating conditions of the accelerator. Slow drifts caused by changes in the length of the laser cavity, cable delays, or the gun resonance frequency and fast jitter caused by the pulse to pulse stability of the laser must be distinguished. The slow drifts may change the relative phase between the linac and the gun either coherently in the case of cable length changes, or incoherently in the case of changes in the laser and/or gun frequency.

The timing stability of the system should be of the order of a fraction of the laser pulse length (regardless of the source) to maintain a stable energy and energy spread. For example, the bunch compressors in the LCLS are very sensitive to the energy and chirp of the electron pulse; small changes can result in a different electron pulse width and hence peak current at the undulator. For the LCLS an rms timing jitter on the order of < 0.5 ps for a 10 ps pulse out of the injector is considered necessary [3]. The

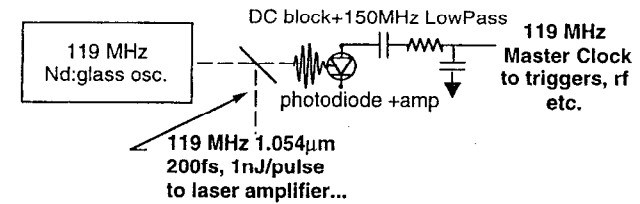


Figure 5.1: The 119 MHz source.

exact number depends on the phases chosen for linac and gun operations. For example, operation near crest in the linac will be very insensitive to phase in terms of the energy gain; however, if the linac is run far from crest in order to impart an energy chirp on the pulse the effect will be much greater. For the GTF, these requirements are slightly relaxed; however, the jitter should still be less than the pulse width to have well defined beam parameters as well as a beam which is easier to tune at any phase.

5.1 rf System

5.1.1 Low Level rf

The master clock of the GTF is derived from the repetition rate of the laser oscillator. The low frequency rf generation is shown schematically in Fig. 5.1. The repetition rate of the oscillator is set by the cavity length and is roughly 119 MHz, the 24th sub-harmonic of the accelerating rf; there is no external source for the rf. Low timing jitter (< 2.5 ps rms: see Section 5.2) has been achieved by using a slow photo-diode (~ 120 MHz) to sample the pulse train from the laser oscillator and frequency multiplying the signal in a phase-locked multiplier [76] to generate the 2856 MHz master

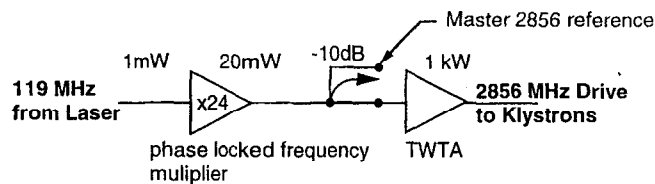


Figure 5.2: The 2856 MHz master clock and 1 kW drive.

rf (with ~ 13 dBm, 20 mW, output). A 10 dB coupler is used to split a fraction of the master clock power for diagnostic purposes. The balance of the rf is used as the input to a traveling wave tube amplifier as shown in Fig. 5.2.

5.1.2 High Power rf

The power for the linac and gun is derived from high power klystrons. Each tube is capable of 20 MW output power. The power to the klystron comes from a pulse forming network (PFN) that provides a roughly 2 microsecond 20 kV pulse triggered by a thyratron switch. Fig. 5.3 shows a schematic of the high power rf system. The output from the 1 kW amplifier is split in a 3 dB coupler to produce independent drives for the two klystrons. Voltage controlled phase shifters in the drive signal provide the amplitude and phase control of the klystron output. An isolator and a directional coupler are at the input to the klystron. The directional coupler provides -30 dB signal for diagnostic of the drive power and phase. The input to the klystron is limited to 300 Watts due to insertion and cable losses.

The output of the klystrons is fed to the linac and gun via evacuated waveguide. Because the gun is a standing wave structure, there is a large transient reflection during

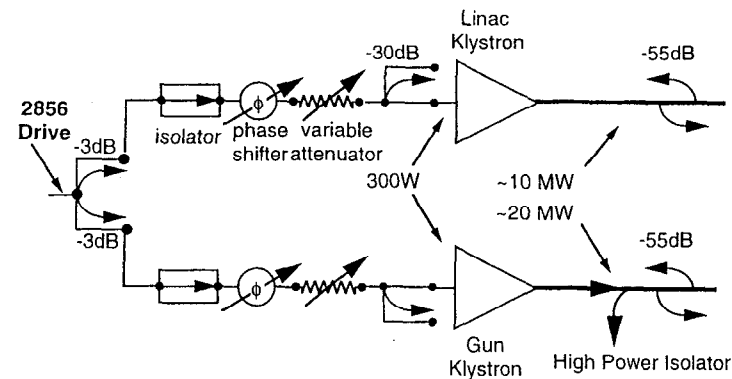


Figure 5.3: High power rf system.

the filling of the gun. Therefore, a high power isolator (pressurized SF₆ gas) is used to protect the gun's klystron. However, the transient reflection from the linac is small enough that an isolator is not required. Directional couplers provide signals to monitor the forward and reflected powers to the gun and linac.

5.1.3 rf Diagnostics

The rf diagnostics systems of the GTF allow for simultaneous measurements of both the amplitude and phase of two different rf signals. These signals include the drive power to each klystron, the forward and reflected powers for each klystron, the power flow to and from the gun and the load on the linac, and the power in the gun which is sampled by a capacitive probe in the pump out port of the half cell. Each signal is sent along 3/8" or 1/2" heliax to one of two rf switches. At the input of each switch the signals are attenuated to the \sim mW level. The various signals are selected either manually or

via the GTF controls program through a custom switch control unit. Each signal is split in a 10 dB splitter, the -10 dB signal is sent to a crystal detector and the rest is sent to the rf input of one of two phase detectors. The output of the crystal detector is then amplified and impedance matched to drive a 50Ω line so that it can be read out via an oscilloscope into the GTF data-acquisition computer. Each crystal detector/amplifier was calibrated using a known source, and each signal has been calibrated to include the loss in the cable, any additional attenuators and the individual couplings.

Fig. 5.4 shows typical forward and reflected power to and from the gun as well as the power in the gun as a function of time. From this figure it can be seen that the gun never quite reaches steady state due to the finite pulse duration of the forward pulse. The large transient response in the reflected power is also seen. This, combined with the forward power, can lead to large peak fields at the klystron and possible damage if an isolator were not used. The dark current background emitted from the gun under these conditions is also shown.

The phase detectors were constructed using a double balanced mixer [92] as a phase bridge to measure shot to shot variations in the phase of different rf signals relative to the 2856 MHz master clock. In this configuration the mixer takes two signals: a reference signal on the local oscillator port and the input signal on the rf port, and it outputs the sum and difference frequencies onto the intermediate frequency (IF) port. A low-pass filter is used so that the difference in phase can be determined from the resulting "DC" signal.

The mixer output can be calibrated by varying the phase difference between the local oscillator or the rf input using a calibrated phase shifter. As long as the mixer is not saturated the output will depend on the sine of the phase difference. The phase detector

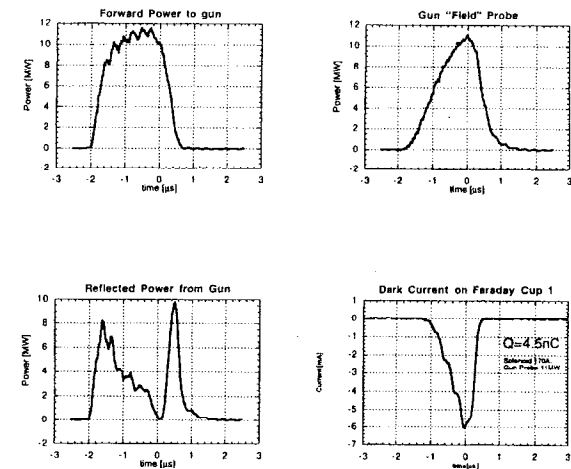


Figure 5.4: rf diagnostic signals showing the forward, reflected and stored power in the rf gun, and dark current collected on a Faraday cup under these conditions.

is then used near the zero crossing of the sine wave such that there is an approximately linear voltage to phase correspondence. Typically there are small DC offsets which are input level and temperature dependent that lead to a small error in determining the absolute phase [93]. These effects are small for a good double balanced mixer, and are ignored here since it is only the shot to shot phase differences that matter.

The calibration is reasonably constant over a wide range of input levels to the rf port. Each mixer has an independent voltage controlled phase shifter capable of swinging 180° on the rf input for use in zeroing the phase difference. These phase shifters are controlled with a 0–10V signal via the controls computer and are low pass filtered on the input to avoid unwanted phase shifts due to noise. The typical calibration for the mixer in the linear regime was 1.75 mV/degree for the data presented in this experiment. This was periodically checked by measuring the peak to peak signal swing and assuming a sine wave. Timing jitter measurements using the double balanced mixer as a phase detector are presented in Section 5.2. Fig. 5.5 shows the mixer output as a function of phase for approximately 14 dBm input power to the rf port and ~ 2 dBm input power to the local oscillator port. The calibration shows an amplitude of 114 ± 1 mV with no signs of saturation. This leads to a calibration in the linear regime of 2.0 mV/degree. This compares to the calibration of 1.75 mV/degree taken at slightly different conditions. The calibration was repeated with approximately 17 dBm on the rf port with the same result (showing the relative insensitivity to the rf input power). This is approximately the same power as is used for the input in the gun phase measurement.

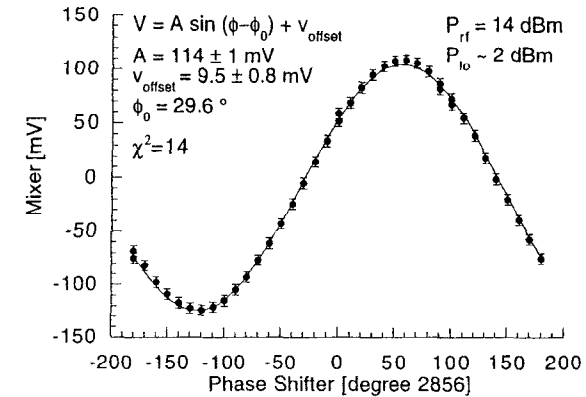


Figure 5.5: Phase detector output as a function of input phase.

5.2 Timing Measurements

Measurements of the timing jitter at the GTF were conducted using the double balanced mixer to measure shot to shot variations in the phase of different rf signals relative to the 2856 MHz master clock derived from the laser. The total jitter between the steady state phase in the rf gun and this master clock was found to be $\sim 0.5^\circ$ rms over a few minutes with negligible contributions from the klystron and its drive. Since 1° of 2856 = 0.97 ps, this corresponds to ~ 0.5 ps of timing jitter. It is estimated that this jitter comes from a shot to shot change in the difference between the drive frequency and the gun resonance and could be produced from either ~ 100 Hz noise in the laser oscillator or ~ 0.05 degree C change in the gun temperature.

The jitter between the 2856 MHz master clock and the 119 MHz from the laser was measured with a fast sampling scope and found to be < 2 ps rms where the upper limit

is set by the trigger jitter of the scope [94]. The amplified laser pulse was found to be stable to <2 ps rms by phase comparing the bandpass filtered output of a photodiode to the 119 MHz again using a double balanced mixer. A potential problem is the long term drift between the laser and the gun. This can be on the order of tens of picoseconds in the course of a day but in principle could be eliminated with a slow feedback on the laser cavity length, the gun temperature, or on the drive phase shifter. This was not a significant problem for the measurements reported here.

No direct measurement of the laser arrival time at the cathode has been made. However, the stability of all the major subsystems has been investigated. The correlation between the jitter of the various subsystems is not always known with the desired degree of precision. The resulting overall timing jitter is estimated to be $0.5 \text{ ps} < \sigma_t < 2.5 \text{ ps}$.

5.2.1 High Power rf Phase Stability

The phase stability of the gun and linac klystron were measured using the double balanced mixer technique discussed in Section 5.1.3. A schematic of the experiment is shown in Fig. 5.6. The phase was measured with respect to the 2856 MHz from the master rf, so care must be taken in the interpretation; this is not necessarily correlated with the laser. Fig. 5.7 shows histograms of the measured phase of the forward power from the gun klystron, and the drive to the gun klystron. Also shown is a correlation plot of the klystron phase versus the drive phase. A total of 100 shots were logged over the course of a few minutes. The klystron was seen to have an rms jitter of approximately 0.32 degrees for a drive phase jitter of 0.26 degrees. The phase difference between the two has an rms jitter of 0.13 degrees showing that the two phases are strongly correlated. The estimated resolution of the phase detector is approximately 0.1 degrees as

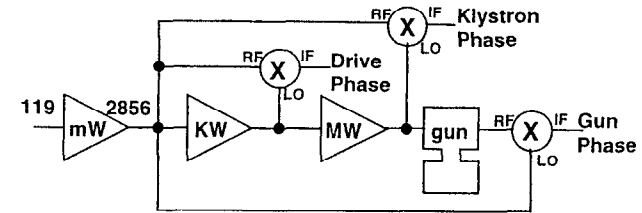


Figure 5.6: Schematic of the phase jitter measurements.

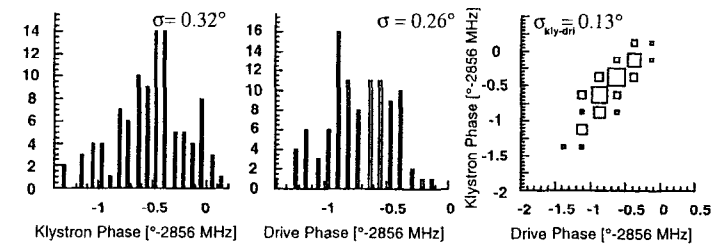


Figure 5.7: Histograms of the phase of the gun klystron, its drive, and the difference logged for 100 shots over a few minutes. Correlation Plot of the klystron phase and drive phase showing the klystron phase to follow the drive phase without introducing significant jitter.

measured by taking the master rf splitting it in a 3 dB hybrid and mixing the two signals with respect to one another. It is therefore concluded that the klystron essentially follows the phase on the input and that any phase jitter originates in the KW amplifier. Similar results were obtained for the linac klystron.

The Gun phase, however, was not seen to be as strongly correlated to the drive phase as can be seen in Fig. 5.8. The rms jitter in the gun was found to be 0.47 degrees for an rms jitter in the drive of 0.23 degrees. The jitter in the difference is 0.37 degrees and the correlation plot shows that the gun phase is almost independent of the drive phase.

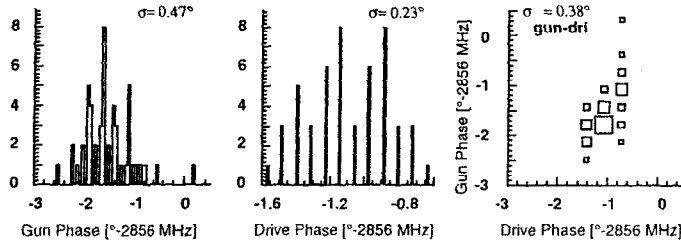


Figure 5.8: Histograms of the phase of the gun, the klystron's drive, and the difference logged for 50 shots over a few minutes. Correlation plot of the gun phase and drive phase showing that the gun contributes to an uncorrelated jitter.

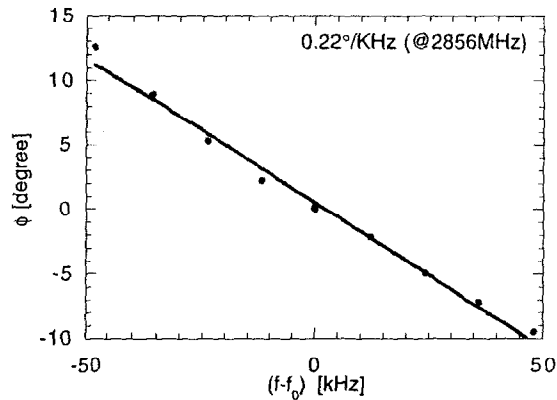


Figure 5.9: Steady state gun phase shift as a function of frequency offset.

The larger jitter in the gun is explained by the relatively high loaded Q_L of the cavity i.e., the combined Q of the gun and waveguide network. The gun acts as a very narrow bandpass filter. Q_L was measured to be 4760 that corresponds to a 3 dB bandpass of ~ 600 kHz. A relatively small changes in the difference between the shot to shot input frequency and the gun resonance can have a strong effect on the steady state phase of the gun. The phase shift near resonance is given by

$$\begin{aligned} \frac{d\phi}{d\omega} &= \tau_{fill} \approx \frac{2Q_L}{\omega}, \text{ or} \\ \frac{d\phi}{df} &= \frac{2Q_L}{f_0}, \end{aligned} \quad (5.1)$$

Where τ is the fill time of the cavity, and $Q_L = \frac{\omega_0}{\Delta\omega_0} = \frac{f_0}{\Delta f}$ is the loaded Q . This leads to a phase shift of $0.19^\circ/\text{kHz}$ for the measured Q_L of 4760.

Fig. 5.9 shows the measured steady state phase shift (at high power) as a function of the difference in the instantaneous frequency. The data were obtained using a low noise synthesizer [95] as the 119 MHz source to the frequency multiplier and making small changes about the gun resonance. Each point is an average of 50 shots. A least squares fit to the data shows a phase shift of 0.22° at 2856 MHz per kHz. Therefore, a 0.5° phase shift in the gun corresponds to a ~ 2.3 kHz change in the resonance frequency. This can either be caused by a ~ 100 Hz change in the laser or approximately 0.05°C change in the gun temperature assuming the frequency changes 50 kHz per degree C [60]. Indeed, in the following section, we will see that there is a significant amount of noise at 100 Hz in the laser; however, similar jitters were measured in the gun when the rf was derived from the low phase noise synthesizer. The cooling water to the gun was found regulated to 0.2°C p-p such that slow drifts on the water temperature will give rise to an approximately 0.5 ps jitter; however the time constant is long compared to the measurement time. Finally, at this level the shot to shot fluctuations in the power to the gun may begin to effect the timing stability and future studies are in order.

5.2.2 Low Level rf and Laser Stability

The stability of the frequency multiplier with respect to the laser rf has been measured using a fast sampling oscilloscope. The 119 MHz from the laser is used to trigger the scope and the jitter in the rising edge of the 2856 MHz from the multiplier was observed. The measurement resulted in an rms jitter of 2.7 ps. The scope trigger jitter was measured slightly higher at 3 ps (measured by splitting the trigger signal and observing the jitter on the input signal). The lower jitter on the 2856 is attributed to the sampling errors. Therefore, the jitter from the frequency multiplier with respect to the laser is ≤ 3 ps and possibly much less.

Using both the laser and a low noise synthesizer as the source resulted in similar jitters in the gun (using the double balanced mixer technique) even though the synthesizer has better phase noise characteristics. Phase (and amplitude) noise appears as side-bands on the fundamental in the spectrum of the rf [96]. For example, the phase noise of the laser at 100 Hz is approximately -80 dBc while the frequency synthesizer is approximately -115 dBc and at 10 Hz the laser is -50 dBc compared to -100 dBc on the synthesizer; however for frequencies less than 10 Hz no comparison could be made. The low frequency noise (on the reference) will likely become the limit in the effectiveness of any external feedback on the laser. The spectrum of the 119 MHz from the laser is shown in Fig. 5.10. Significant side bands exist at 10 Hz and its harmonics up to approximately 120 Hz. These are mostly due to acoustics from a large transformer that ramps the magnets in the booster cyclotron to SPEAR and that operates at 10 Hz. Also shown in Fig. 5.10 is the spectrum of the laser when a piezo-electric driven feedback is present on the cavity length. This feedback is referenced to the low noise synthesizer. It is shown to significantly reduce the sidebands; however, the feedback was unavailable

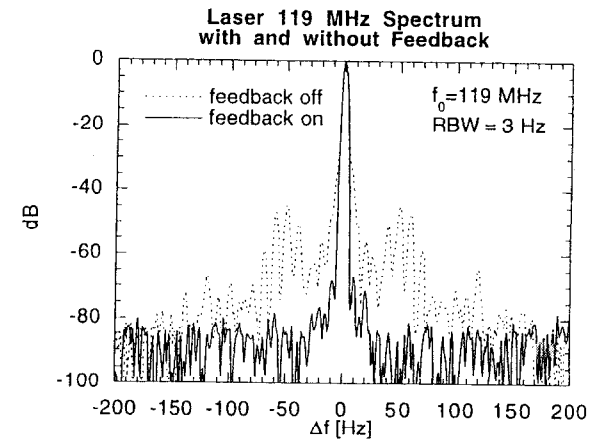


Figure 5.10: Spectrum of the 119 MHz from the laser photodiode both with and without feedback on the cavity length.

at the time of the electron beam measurements, and the timing measurements presented here are thus made without it.

Comparing the spectrum of the 2856 output from the multiplier with that of the 24th harmonic of the laser shows that there are no significant differences in the spectral content of the two (see Fig. 5.11). The exception is that the noise floor is higher on the laser's spectrum as the total power available for the measurement was ~ 80 dB less than from the multiplier. From the absence of any new spectral content in the multiplier signal, it is inferred that the multiplier follows the laser quite well.

The jitter of the laser can be inferred by spectral analysis techniques using the times 24 multiplier's spectra and assuming that the uncorrelated jitter between the laser and the 2856 is small. Fig. 5.12 shows the spectrum of the multiplier for a slightly large

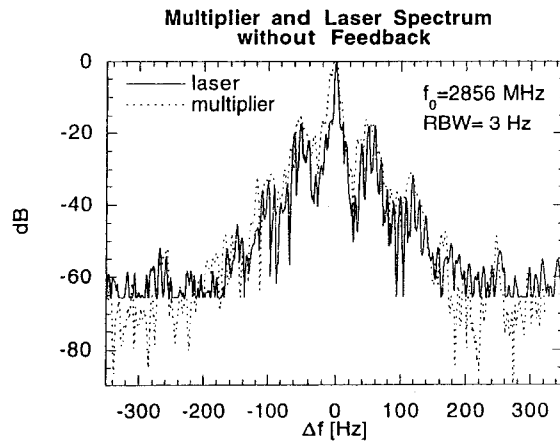


Figure 5.11: Spectrum of the 2856 from the multiplier and the laser on a fast photodiode.

span. Using even larger spans no other side bands are detected above the noise floor of the spectrum analyzer. Assuming a Gaussian noise distribution, the timing jitter can be calculated by [96]

$$\sigma_t = \frac{1}{n\omega_0} \left(\frac{1}{\pi} \int_{\omega_{low}}^{\omega_{high}} L(\omega) d\omega \right)^{\frac{1}{2}}, \quad (5.2)$$

where n is the harmonic number, the integration is over the frequency offset from the n^{th} harmonic, $L(\omega)$ is the ratio of the peak amplitude to the sideband amplitude, and $\omega_{low,high}$ are the low and high frequency components (offsets) over which the measurement was made. $\omega_{low,high}^{-1}$ corresponds to roughly the maximum and minimum measurement time which over which the jitter is calculated. The spectral density $L(\omega)$ is corrected for the resolution bandwidth of the measurement as well as for any filtering due to the spectrum analyzer electronics. For offsets $30 < f < 780$ Hz, the jitter is

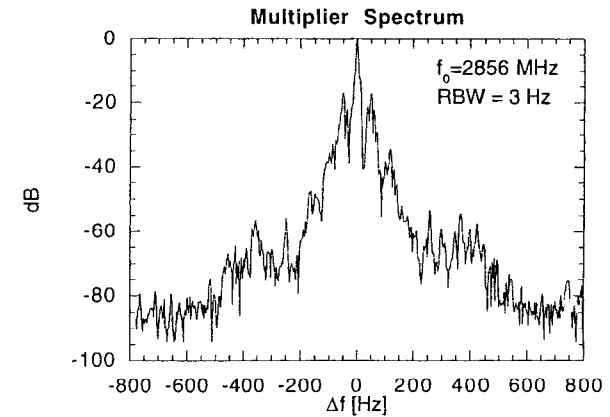


Figure 5.12: Spectrum of the 24 times frequency multiplier when driven with the free running laser.

estimated at 45 ps. This is much greater than even the worst estimate on the timing jitter by other means and indicates that the Klystrons, gun and linac do, to a great extent, jitter in phase with the laser.

5.2.3 Other Timing Measurements

None of the measurements discussed so far tell us about the jitter of the individual laser pulse compared to the phase in the gun (or linac). Fig. 5.13 shows the experimental setup for determining the electron beam phase as it exits the gun. The phase is determined using the electrical signal from the Faraday cup and filtering it at 119 MHz to make a phase measurement with respect to the laser 119 MHz. The result for an operating phase in the gun of 48 degrees (50 degrees is used in the emittance measurements)

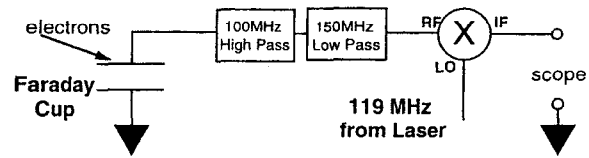


Figure 5.13: Experimental setup for beam phase measurement.

is ~ 0.8 ps rms. While at 0 degrees, ~ 3 ps of jitter was measured, and at 24 degrees ~ 2 ps of jitter is measured. The measurement using a very low Q bandpass filter comprised of a 100 MHz high pass filter and a 150 MHz low pass filter. This combined with the fact that 1 ps $\sim 1/24$ of one degree at 119 MHz led to an estimated uncertainty of approximately 2 ps.

In addition, the same experimental setup was used to measure the phase of the single UV pulse with respect to the 119 MHz (except that a photodiode was used instead of a Faraday cup). The result was 2 ps rms with the same estimated 2 ps uncertainty.

5.2.4 Summary

The results of the various phase measurements are presented in Table 5.1. While all of the correlations are not known, it can be assumed that the worst case for the individual laser pulse to the gun phase is

$$\sigma_t = \sigma_{\text{gun}} + \sigma_{\text{UV}} + \sigma_{x24},$$

Source	rms timing jitter	Method
Gun to 2856	0.5 ps	DBM
Klystron to 2856	0.3 ps	DBM
KW drive to 2856	0.25 ps	DBM
2856 to laser 119	< 3 ps	sampling scope
UV to laser 119	< 2 ps	DBM
Electron beam to 119	< 1 ps	DBM

Table 5.1: Summary of timing jitter results.

or approximately < 5.5 ps. Assuming that the multiplier is not contributing significantly to the jitter, $\sigma_t < 2.5$ ps. The lower limit is the jitter which was measured in the gun, $\sigma_{\text{gun}} = 0.5$ ps. The timing jitter measurements presented here were obtained without feedback on the laser oscillator. A slow feedback on the oscillator has since been incorporated into the system, and significant reduction in the laser phase noise has been shown. It is expected that a combination of the slow feedback on the laser will reduce the timing jitter to that of the the values given for the gun and drive; however a more stable source and better temperature regulation may be required to significantly reduce the jitter in the gun.

Chapter 6

Results

In this chapter we present the electron beam measurements. This includes the measurement of the quantum efficiency (at both grazing and normal incidence) of the copper cathode. Initially the efficiency of the cathode was too poor to produce a 1 nC beam with the available laser energy. In addition, the uniformity of the cathode was poor on the scale of the typical transverse laser size. Results of laser cleaning of the cathode are presented for both the efficiency and uniformity. The quantum efficiency depends on the electric field at the cathode at the time of the laser injection. A scan of the efficiency as a function of the laser injection phase is given, and will be used in the determination of the phase for the emittance measurements. Also from this data, a measurement of the transverse and longitudinal thermal emittance of the beam is given. Finally, rms horizontal emittance measurements are made using a quadrupole scan technique. These measurements are made for various laser pulse widths and as a function of charge and transverse profile. In addition, at each condition the emittance is measured as a function of the emittance-compensation solenoid field strength in order to determine the lowest emittance.

6.1 Quantum Efficiency Measurements

As described in Section 2.1.4, the quantum efficiency is defined as the number of electrons emitted from the gun per *incident* number of incident laser photons, $\eta = N_e / N_\gamma$. The laser energy is measured on each shot using a pyro-electric detector [97] by picking off a small portion of the laser pulse by reflection off of a fused silica wedge. The signal from the detector is amplified and recorded by the data acquisition system. The amplified signal was cross-calibrated by using another pyro-electric detector (with known calibration) in the main portion of the beam. The UV energy was changed over many

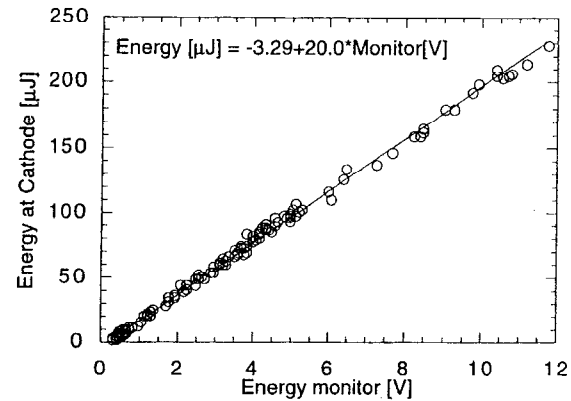


Figure 6.1: Calibration of the laser energy monitor. The calibration is valid for normal incidence and includes a combined transmission of 0.81 from the vacuum window and normal incidence mirror

orders of magnitude by using a half-waveplate to vary the polarization to the doubling crystal. This is essentially equivalent to varying the input intensity to the crystal. The calibration was found to be linear up to at least 240 μJ . Fig. 6.1 shows the results of a typical calibration. Included in the calibration is a factor of $\sim 20\%$ loss measured from the UV window and normal incidence mirror before installation. The calibration shows a residual noise of ~ 200 mV in the amplifier. When the rf system is on this can be increased to ~ 500 mV and leads to a large systematic error in the energy measurement especially at low energies. Because of the differences in noise under different conditions, a calibration of $20 \mu\text{J}/\text{V}$ is used and the signal is typically background subtracted to reflect the background at the time of the measurement.

Section 3.1.5 describes the Faraday cups used for charge measurement. Typically a 14 dB attenuator was included in the charge measurement on the Faraday cups to pre-

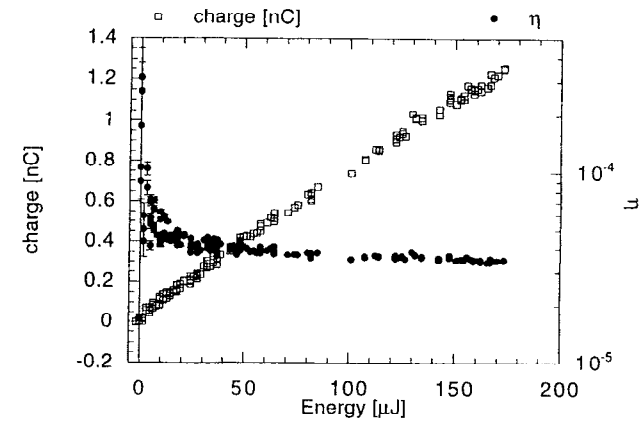


Figure 6.2: The charge and quantum efficiency versus laser energy incident on the cathode.

vent damage to the scopes during a “super-charge” emission from the cathode (see Section 6.1.1). Fig. 6.2 shows charge measured on Faraday cup 2 as a function of laser energy. The data was taken after “laser cleaning” of the cathode that is discussed in Section 6.1.1. The charge is background subtracted to remove the dark current contribution and laser energy is determined as previously discussed. The plot suggests an error in the background subtraction for low values of charge and/or laser energy; however, for laser energies above $50 \mu\text{J}$ the quantum efficiency is roughly constant at $\sim 3.5 \cdot 10^{-5}$.

The quantum efficiency depends on the polarization of the laser for non-normal incidence angles. Table 2.2 on page 23 summarizes the reflectivity for normal and grazing (72°) incidence. The UV laser pulse is produced with linearly polarization. By use of a $\lambda/2$ waveplate, the polarization angle of the laser may be changed and thus the mixture of s and p-polarizations. Fig. 6.3 shows the quantum efficiency measured as a function

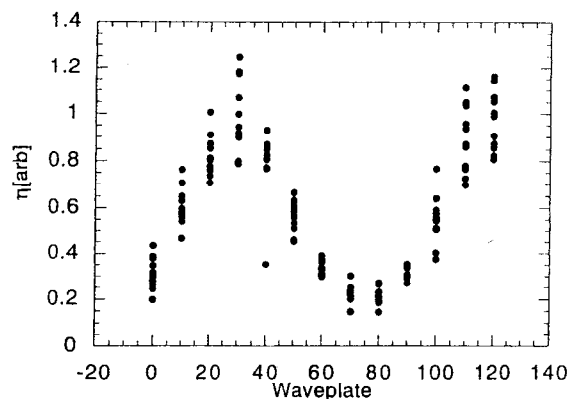


Figure 6.3: Quantum efficiency as a function of waveplate angle for grazing incidence.

of the (relative) angle, θ , of rotation about the optic axis of the $\lambda/2$ plate. For each 45° rotation about the optic axis, the polarization is rotated by 90° . According to the differences in reflectivity there should be ~ 2.5 times higher efficiency for p-polarized light than for s; however, a value of $\sim 5-6$ is seen. The discrepancy is likely explained due to additional Schottky lowering of the work function due to the electric field of the laser for p-polarization as discussed in Section 2.1.4.

6.1.1 Cathode Uniformity

Because of the initially low quantum efficiency ($\sim 5 \cdot 10^{-6}$ electron/photon) and large scale ($\sim 100\%$) non-uniformity of our copper cathode (see Fig. 6.4), the cathode was cleaned *in-situ*. A relatively high intensity ($\sim 2 \cdot 10^9$ W/cm 2) laser pulse was incident on the cathode in the presence of ~ 100 MV/m electric field. An attempt to clean the

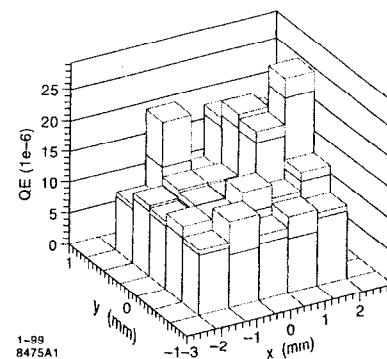


Figure 6.4: Quantum efficiency across cathode before “laser cleaning”. The stacked blocks represent the statistical error.

cathode in the absence of rf power failed to make any noticeable improvements. During the cleaning process, $\sim 1 \mu\text{C}$ of charge on each (laser) shot is extracted from the cathode in ~ 50 ns depleting the stored energy in the gun. Fig. 6.5 shows a Faraday cup signal attenuated by 48 dB and the gun field probe during such an event. From this $\sim 0.6 \mu\text{C}$ of charge is estimated to be emitted which extracts ~ 0.65 MeV = 3 J of energy out of the gun. This is not too far off of the estimated 5 J stored in the gun (from the shunt impedance and the measured Q). The laser intensity at which such an event is initiated is within an order of magnitude of the standard operating conditions, such that a poor quantum efficiency cannot be overcome simply by brute force.

The enhanced emission during this process appears to be the same as previously reported [98] and was achieved by focusing the laser onto the cathode at grazing inci-

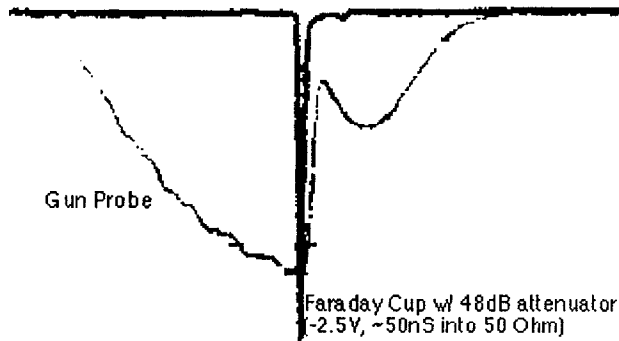


Figure 6.5: A "super-charge" event as seen on the gun field probe and a Faraday cup.

dence to roughly $1 \times 0.3 \text{ mm}^2$. The cathode was "cleaned" by continuously scanning the laser across an area of roughly $5 \times 3 \text{ mm}^2$. The area was scanned in passes along the short axis of the laser at a rate of 22 shots/mm while maintaining the enhanced emission throughout each pass and with an overlap of 0.3 mm between passes. The cleaning resulted in a larger quantum efficiency (typically $2\text{--}3 \cdot 10^{-5}$ at our normal operating conditions; see Fig. 6.2) and a more uniform cathode ($\sim 0.3 \text{ mm}$ scale) as shown in Fig. 6.4 (before) and Fig. 6.6 (after). However, the dark current (field emission) from the cathode also increased by roughly an order of magnitude.

The electrical center of the cathode (i.e., the point where the electrical axis of the gun intersects the cathode) was found in this and the other measurements in the same manner. The solenoid is used to focus the beam onto one of the phosphor screens in the low

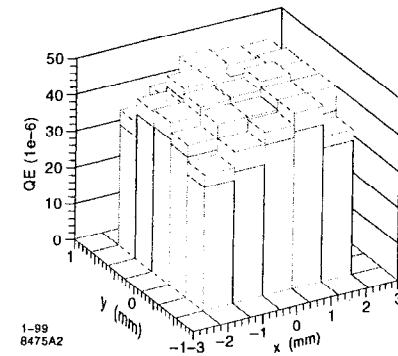


Figure 6.6: Quantum efficiency across cathode after "laser cleaning". The stacked blocks represent the statistical error.

energy beam line. The laser is scanned across the cathode and the solenoid field and/or the phase in the gun is varied. The center of the cathode is presumed to be where no deflection of the beam occurs. Technically the combined axis of the gun and the solenoid is determined. Changing the phase in the gun gives a time dependent kick on the exit as well as changes the beam energy (which changes the focusing from the solenoid). If the axes are well aligned, either changing the phase in the gun or changing the solenoid strength suffices to determine the center.

The cleaning process appears to cause a micro-roughening of the cathode surface. By scanning a HeNe laser across the cathode from near normal incidence and looking at the amount of light scattered at oblique angles, the "cleaned" area is easily discerned from the "un-cleaned" area due to the increase in scattered light. This roughening

may explain the increase in dark current by creating areas of increased localized field. The increase in the quantum efficiency may be from removal of copper oxide or other contaminants from the cathode surface in addition to the localized field enhancement. During the scans, the vacuum gauges in the gun were monitored, and the pressure was found to increase roughly two orders of magnitude while the enhanced emission was occurring.

Fig. 6.7 shows a Fowler-Nordheim plot (Section 2.1.3) of the dark current extracted from the cathode for three cases: the initial cathode, the cathode after a single damage site occurred, and the cathode after "laser cleaning". The effective microscopic field at the cathode can be determined from the slope in Fig. 6.7 using eq. (2.10) on page 21. In addition to nearly approximately an order of magnitude more current, the microscopic field at the cathode has nearly doubled after laser cleaning. This is consistent with the *micro-roughening picture* although it should be noted that due to the strong non-linearity in the field emission current, that the enhancement could be dominated by a few "sharp" features on the cathode. In addition, a slight increase in the microscopic field after a single damage site on the cathode can be seen. The origin of the damage is not known but may have been caused by a single "super-charge" event. All data were taken after extensive rf processing of the gun.

6.1.2 Schottky Scans

The electron yield/photon was measured as a function of the laser phase (Schottky scan) on a Faraday cup just after the emittance-compensation solenoid. Assuming a 100% collection efficiency this is equivalent to measuring the quantum efficiency as a function of phase (and thus cathode field) as defined in Section 2.1.4. A typical scan

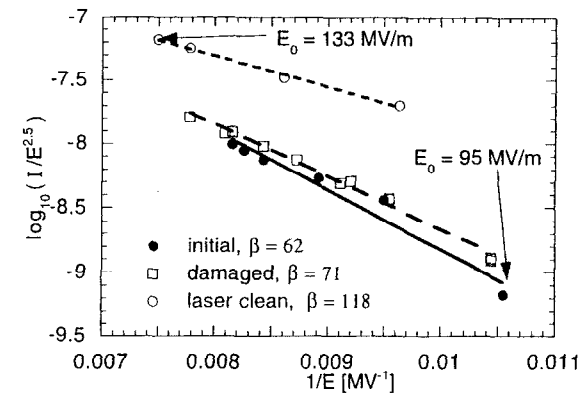


Figure 6.7: Fowler Nordheim plot of the dark current before and after "laser cleaning".

is shown in Fig. 6.8. The data were obtained at a single solenoid setting for phases below 100°, but due to a significantly decreased energy and increased energy spread, the solenoid had to be varied for phases above 100° to optimize charge collection on the Faraday cup. Not shown on the plot is the rapid decrease in the charge for phases above ~120° as the emitted electrons fail to be captured by the accelerating field.

The scan is used to determine the operating phase by observing where emission first takes place. Due to the finite duration of the laser pulse, the error in determining this phase is on the order of the pulse duration. For the emittance scans, the zero phase was taken to be a few degrees into emission to try and account for the finite pulse duration. This also ignores the non-zero efficiency for negative phases due to the excess energy between the photon and the work function. In addition to these systematic errors in the phase determination, there is a statistical error in the phase due to the shot to shot variation in the arrival time of the laser. The rf phase of the gun is recorded on each shot

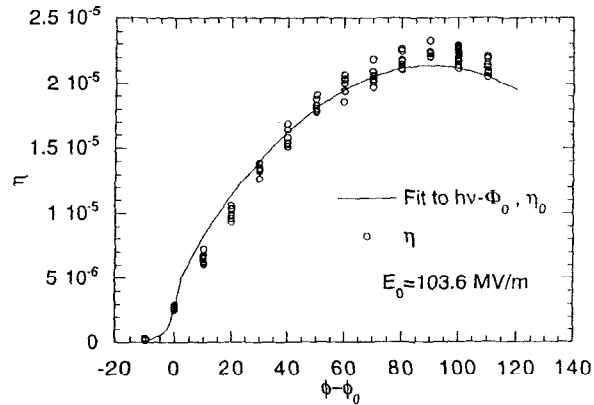


Figure 6.8: A typical schottky scan from which the laser phase relative to the gun and the thermal emittance are estimated. The quantum efficiency is determined from the charge measured on the Faraday cup (with the average dark-current background subtracted) and is normalized to the number of laser photons.

and the phase variation was found to be small compared to the systematic error. The scans were repeated to make sure that the effects of long term drift were understood.

6.2 Emittance Measurements

6.2.1 Thermal Emittance Measurement

The Schottky scan of Section 6.1.2 can also be used to determine the thermal emittance of the electron beam as the electric field and thus the work function at the cathode are varied over a wide range of values.

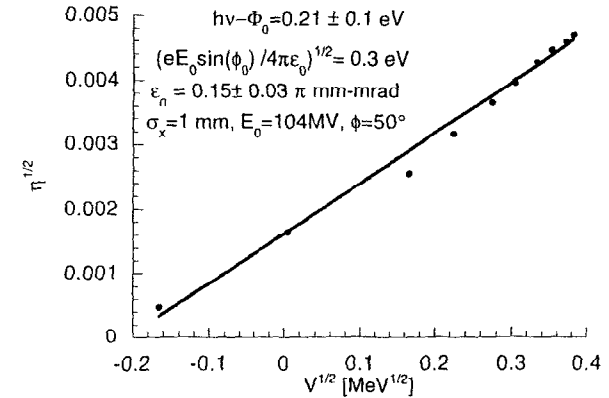


Figure 6.9: Thermal emittance plot.

The field at the cathode is given by $E = E_0 \sin \phi_0$ where E_0 is the peak field on the cathode (determined from the power measured from the gun field probe). Assuming that the quantum efficiency varies as $\eta/\eta_0 = (\hbar\omega - \Phi_0 + e\sqrt{eE_0 \sin \phi_0 / 4\pi\epsilon_0})^2$ for small changes in the quantum efficiency, one can fit a line to $\sqrt{\eta}$ as a function of $\sqrt{V_c}$, where $V_c = e\sqrt{eE_0 \sin \phi_0 / 4\pi\epsilon_0}$ is the Schottky lowered potential at the cathode in eV. This is presented, in Fig. 6.9, for the data of the Schottky scan shown in the Fig. 6.8. Only the data corresponding to phases, $\phi_0 \leq 100^\circ$ were included due to the uncertainties in the charge collection for phases over 100° as already discussed. From the fit, one determines the difference between the laser energy and the zero applied field work function to be 0.2 ± 0.1 eV. The fit has the zero phase fixed, and the error is estimated by changing this phase $\pm 5^\circ$. With the photon energy of 4.7 eV this corresponds to a zero field work function $\Phi_0 = 4.5 \pm 0.1$ eV consistent with the lowest value of the work function given in Table 2.1 on page 17. From eqs. (2.56) and (2.58), substituting

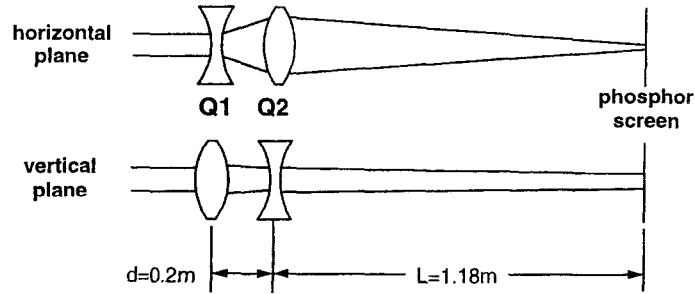


Figure 6.10: Lattice used in emittance measurements.

$\sigma_x = 1$ mm for the rms beam size, and using 4.7 eV for the photon energy, the thermal emittance is $0.15 \pm 0.06 \pi$ mm-mrad for emission at 50° , consistent with the estimate made in Chapter 2.

6.2.2 Quadrupole Scans

The horizontal emittance of the electron beam is measured, after acceleration in the 3 m linac, using a quadrupole scan technique. In a quadrupole scan the spotsize of the electron beam is measured as a function of the focusing strength of a quadrupole. A schematic of the lattice used is shown in Fig. 6.10. The second quadrupole, Q2, is varied such that the electron beam spotsize at the phosphor screen varies through a wide range about the minimum spotsize. The strength of the first quadrupole, Q1, is kept constant and is set such that one can produce roughly the smallest possible spots in the horizontal plane while maintaining a small (and roughly constant) spotsize in the vertical plane. The transfer matrix of the lattice is given generically by eq. (2.39),

$$\begin{pmatrix} A & B \\ C & D \end{pmatrix},$$

and the beam matrix is given by eq. (2.45),

$$\begin{pmatrix} \sigma_{11} & \sigma_{12} \\ \sigma_{12} & \sigma_{22} \end{pmatrix}.$$

The evolution of the square of the spotsize, σ_{11} , can be determined from the transfer matrix from the second quadrupole to the screen. It is a function of the focusing strength of the quadrupole and the drift space, and is a quadratic function in A and B,

$$\sigma_{11}(f) = A^2(f)\sigma_{11}^{Q2} + 2A(f)B(f)\sigma_{12}^{Q2} + B^2(f)\sigma_{22}^{Q2}, \quad (6.1)$$

where σ_{ij}^{Q2} is the beam matrix before Q2 and $A = 1 - L/f$, $B = L$ in the thin lens approximation (however, the lattice is treated with the quadrupole as a thick lens). A least squares fit to the measured spot sizes then yields the beam matrix, σ_{ij}^{Q2} , from which the emittance is calculated using eq. (2.47),

$$\epsilon_{geom} = \sqrt{\sigma_{11}^{Q2}\sigma_{22}^{Q2} - (\sigma_{12}^{Q2})^2},$$

and the normalized emittance is given (knowing the normalized beam energy γ and velocity β) by eq. (2.43),

$$\epsilon_n = \gamma\beta\epsilon_{geom}.$$

To avoid hysteresis effects in the magnets, the quadrupoles were standardized before each scan. In addition, during the scan, the quadrupole was varied always in the same direction. A typical scan consists of 10–12 current settings with 5 signal and 1 background image acquired at each setting. Fig. 6.11 shows the results of a typical quadrupole scan. The data is from the 1 nC, 5 ps, 2.1 kG scan. The spotsize squared is

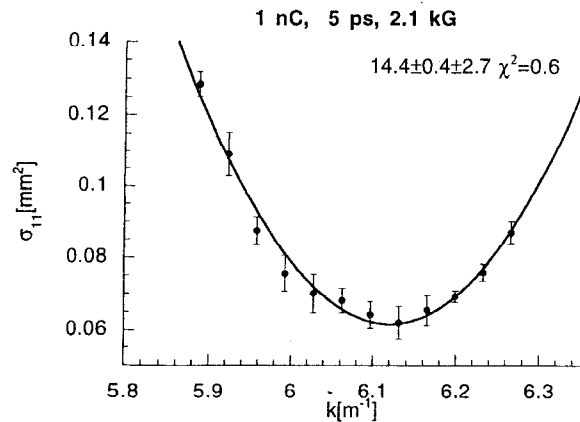


Figure 6.11: Sample quadrupole scan with least squares fit to thick lens plus drift.

plotted as a function of the focusing strength parameter of the second quadrupole, K_{Q2} . The solid circles are from the measured spotsizes, and the error bars represent the rms spread in the data while the solid line is the result of the least squares fit.

In principle the vertical emittance can be obtained using the corresponding transfer matrix as well, but in practice the vertical spotsize does not vary enough (during a horizontal scan) to give a reasonable precision. Therefore, in order to measure the vertical emittance either Q1 is varied as Q2 is kept constant, or the lattice should be rotated 90° .

The above discussion assumes that the effects of space-charge do not significantly alter the beam as a result of the measurement process; the emittance determines the spot-size i.e., the beam is emittance dominated. While measurements were made at peak currents of up to 200 A, simulations indicate no appreciable increase in the calculated emittance [99, 100]; thus, space-charge effects in the measurement process are ignored.

6.2.3 Spotsize Determination

Image Acquisition

The beam profile is obtained by imaging the phosphor screen onto an 8-bit CCD camera [101]. The full 2D image was acquired using a commercial frame grabber [102] (at approximately a 0.5 Hz acquisition rate) and analyzed "off-line" to determine the spotsizes. Because of a relatively large dark current background, background subtraction was performed on the images. Five "signal" and one "background" images were acquired at each quadrupole setting. Because only one background image was acquired, it was assumed that it is typical. This is justified since the background conditions are fairly constant except during an electrical breakdown in the gun (these events are ignored). However, for events with poor signal to noise ratio, the fluctuations in the background can cause a larger background than the signal (also ignored).

For each quadrupole scan, the beam was first focused to the smallest possible size, and the camera was examined for saturation. The intensity was set such that there was a reasonable signal to noise ratio without saturation. The intensity was controlled using cross polarizers such that the depth of field, and thus the resolution, remained constant. The polarizers were not adjusted during the course of a scan. The pixel calibration was determined using a $125 \mu\text{m}$ wire as a fiducial. The calibration yielded 16 pixels for $125 \mu\text{m}$ with an estimated resolution of 3 pixels [53] or $7.81 \pm 1.47 \mu\text{m}/\text{pixel}$ in the horizontal plane. In the vertical plane because the screen was oriented at 45° the calibration is reduced by a factor of $1/\sqrt{2}$.

Beam Moment Calculation

The first and second moments of the beam profile are

$$\langle x \rangle = \frac{\int_{\Omega} x f(x, y) dx dy}{\int_{\Omega} f(x, y) dx dy}, \quad (6.2)$$

$$\langle y \rangle = \frac{\int_{\Omega} y f(x, y) dx dy}{\int_{\Omega} f(x, y) dx dy}, \quad (6.3)$$

$$\langle (x - \langle x \rangle)^2 \rangle = \frac{\int_{\Omega} (x - \langle x \rangle)^2 f(x, y) dx dy}{\int_{\Omega} f(x, y) dx dy}, \quad (6.4)$$

$$\langle (y - \langle y \rangle)^2 \rangle = \frac{\int_{\Omega} (y - \langle y \rangle)^2 f(x, y) dx dy}{\int_{\Omega} f(x, y) dx dy}, \text{ and} \quad (6.5)$$

$$\langle (x - \langle x \rangle)(y - \langle y \rangle) \rangle = \frac{\int_{\Omega} (x - \langle x \rangle)(y - \langle y \rangle) f(x, y) dx dy}{\int_{\Omega} f(x, y) dx dy}, \quad (6.6)$$

where $f(x, y)$ is the background subtracted pixel amplitude as a function of the screen position, and the integration is over the extent of the beam Ω which is yet to be determined. The pixel amplitude is on a scale of 0–255 for an 8-bit camera (–255–255 when background subtracted). The second moments determine a rotated ellipse (see Appendix B) about the first moments, and the second moments will henceforth utilize a coordinate system centered about the first moments.

A two dimensional analysis for determining the beam parameters is used because of its relative insensitivity to random errors as compared with an analysis utilizing a single slice through the image (line-out). These errors may be due to “snow” from ionizing radiation striking the CCD or thermal noise in the CCD. Other less random errors arise from local non-uniformities in the phosphor or CCD. The phosphor and CCD are assumed to be globally uniform. The effects of snow were investigated by writing a digital filter that removed any portion of the image that had features less than the camera resolution (often removing as much as a few percent of the image) and the rms calculations were found to be robust. Based on Monte Carlo simulation with a pseudo-random noise

background, the technique was found to be able to reconstruct the rms of a Gaussian with (peak) signal to noise ratio approaching unity.

Due to the very non-symmetric beams that were often produced during the quadrupole scans, it was determined to be unsatisfying to base a measurement on such a small fraction of the beam as would be done if a line-out were used. In this manner, the two dimensional analysis averages over beam imperfections such as “hot-spots” that could artificially produce too small of a calculated spotsize. However, due to the disproportionate number of pixels used in the wings of the beam compared to the center, the two dimensional approach is much more sensitive to any residual background than the lineout (or one dimensional approach). Errors from residual background can thus be potentially large.

If there is a residual background, say from improper background subtraction, instead of measuring the real $\langle x^2 \rangle$,

$$\begin{aligned} \langle x_{meas}^2 \rangle &= \frac{\int x^2 (s(x, y) + b(x, y)) dx dy}{\int (s(x, y) + b(x, y)) dx dy} \\ &= \langle x_{true}^2 \rangle \frac{\bar{s}}{\bar{s} + \bar{b}} + \frac{\bar{b}}{\bar{s} + \bar{b}} \frac{\int_{\Omega} x^2 dx dy}{\int_{\Omega} dx dy} \\ &= \langle x_{true}^2 \rangle \frac{\bar{s}}{\bar{s} + \bar{b}} + \frac{\bar{b}}{\bar{s} + \bar{b}} \frac{a^2}{4} \end{aligned} \quad (6.7)$$

is measured where \bar{s} is the average signal pixel value, \bar{b} is the average residual background value, and a is the size of the horizontal axis of the ellipse over which the measurement is taken. For simplicity it is assumed that the ellipse is upright, and it is further assumed that the residual background is randomly distributed such that it may be factored out of the integral. Finally, it is assumed that there are no errors from artificially clipping the beam. The error in determining the spotsize is then given to

lowest order by

$$E(\langle x^2 \rangle) \approx \frac{\bar{b}}{\bar{s}} \left(\frac{a}{2} \right)^2 \quad (6.8)$$

and similar errors for $\langle y^2 \rangle$, etc. This was typically on the order of a few percent of the calculated moment and was neglected.

In order to determine the beam spotsize, it must first be determined which parts of the profile should be included in the integration of eq. (6.2) through eq. (6.6). Initially the extent of the beam, Ω , is taken over the entire screen (480 vertical by 640 horizontal pixels). To determine the beam boundaries, a similar ellipse is constructed whose axes are scaled by a factor of $n > 1$ (i.e., the area by a factor of n^2) from the rms values. This larger ellipse defines the beam boundaries for the purpose of the calculations given here. The moment calculations are then repeated for pixels lying inside of this larger ellipse. Anything outside of the ellipse is considered "residual" background while anything inside the ellipse is considered signal plus "residual" background. An average background pixel and average signal pixel are then calculated. The process is iterated until either all values converge to within the pixel resolution, or *either* the average signal fails to increase *or* the average background fails to decrease. This method was found to be robust in determining the beam moments either when starting with the entire screen and working inwards or starting with an arbitrarily small spot and working outwards. In fact, for low signal to noise images with small spots, negative $\langle x^2 \rangle$ or $\langle y^2 \rangle$ could be calculated in the first step in which case the moments were determined working from a small spot outwards (note that negative $\langle xy \rangle$ is physical).

The value of n was determined as a compromise between the inclusion of excessive noise and the exclusion of excessive signal. A value of 3 was used which typically includes >95% of the beam as defined with $n = 4$ but includes approximately half as

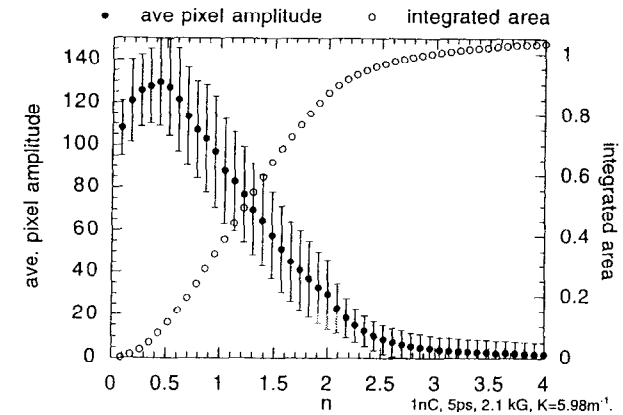


Figure 6.12: Radial profile and integrated signal for a typical electron beam image.

many pixels. For example, Fig. 6.12 shows the average pixel amplitude as a function of n (solid circles) for one of the beam images. The error bars are the rms spread about the average. Also shown (open circles) is the integrated signal normalized to the $n = 3$ area. In this instance increasing the beam extent from 3 to 4 σ increases the integrated signal only 3%. Fig. 6.13 shows a logarithmic plot of the pixel amplitude distribution for both the signal and residual background of this sample image. A fit to the background (solid line) shows that the noise is well described by a Gaussian distribution with an rms of 4.1 (compared to the calculated rms of 4.7).

In Fig. 6.14, histograms of the average signal, background, and edge amplitude are shown for all of the background subtracted images of a sample quadrupole scan for different definitions of the beam extent. The average edge is defined here as the average pixel value of the outer 3% of the beam as defined above. The figure indicates that in

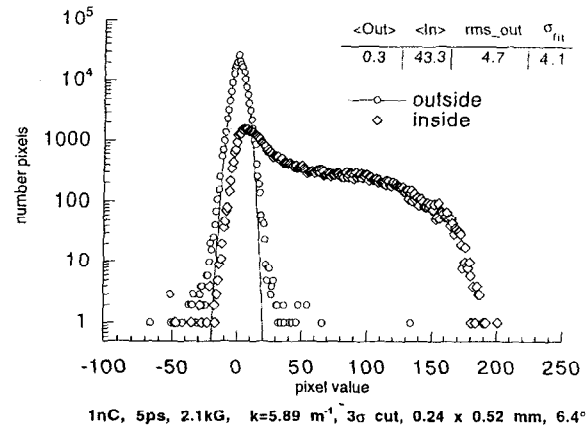


Figure 6.13: Logarithmic plot of signal and background pixel amplitudes for a typical electron beam image.

the case of the 2.25 and 2.5σ cuts considerable amounts of beam are excluded from the image due to the large amplitude at the beam edge as compared to the background. In the 3σ cut there is some beam being lost in the cut although the value at the edge is within the rms of the background (which is of the order of $\sim 4-5$). The 4σ definition shows the edge of the beam and the background as essentially indistinguishable. Fig. 6.15 shows the same quadrupole scan as Fig. 6.11 but analyzed as a function of the four beam extent definitions given above. As the beam is cut more into its core, smaller spots and hence smaller emittances are calculated as is to be expected when less and less of the beam is included. However, more interesting is the shift in the shape of the quadrupole scan from a very symmetric scan at hard cuts to a quite asymmetric scan at soft cuts. This indicates that the beam consists of a relatively large halo whose phase space evolves considerably differently than the bulk of the beam. Because of the

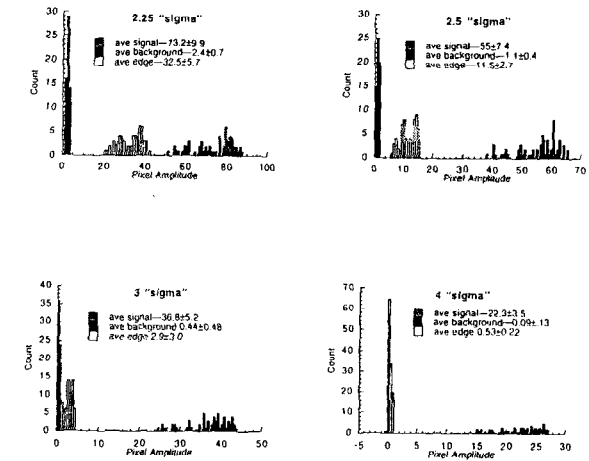


Figure 6.14: Histogram of signal, background and beam edge pixel amplitudes for all the images of a typical quadrupole scan.

different evolution of the halo, it cannot simply be removed from the measurement; at different focusing strengths of the quadrupole the halo may be included more into the beam core while at others it may be more at the beam edges.

Horizontal-Vertical Coupling

In order that the emittance be described in terms of the determinant of the two by two beam matrix, eq. (2.47), the six dimensional phase space should be factorable into three independent two dimensional phase spaces. The coupling of the longitudinal to transverse phase spaces leads to a larger measured transverse emittance due to the lack of time resolution in the measurement. In this sense the quadrupole scan is measuring the time projected transverse emittance. Emittance-compensation occurs when the trans-

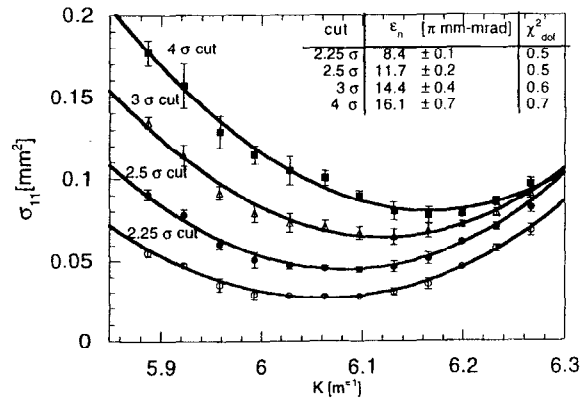


Figure 6.15: Sample quadrupole scan as a function of the definition of the electron beam extent.

verse phase spaces of the various temporal slices of the beam are at their *best* alignment. Because the quadrupole scan using a phosphor screen lacks temporal resolution, the emittance is measured as a function of the solenoid field to try and experimentally find the best compensation.

Much as the transverse and longitudinal spaces can be coupled, so too can the two transverse spaces. This was indeed the case for much of the data taken here. Fig. 6.16 shows an image where the correlation is approximately 20° . The image has been corrected for the aspect ratio, cropped to 2 mm square, and adjusted for brightness and contrast for display purposes. Since the correlation angle varies with the quadrupole strength, it is known that the observed image is not a simple rotation between the quadrupole and the camera pixels.

Because of the coupling between the horizontal and vertical planes, the horizontal emit-

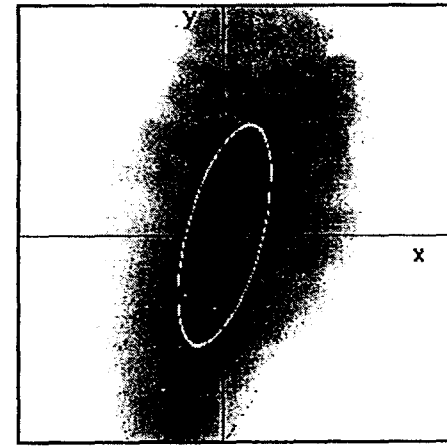


Figure 6.16: Sample beam image.

tance calculated utilizing the horizontal rms spotsize will be a projected emittance along the vertical. The vertical emittance could be calculated in the same way. The consequence is that the product of these two emittances will not (necessarily) be constant with respect to rotations of the quadrupoles about the beamline axis (i.e., the definition of vertical and horizontal axes) if the phase space is not azimuthally symmetric.

In principle this could be solved by the addition of a skew quadrupole to remove the coupling in the beam (analogous to the use of the solenoid to try to remove the transverse-longitudinal coupling). Or, if the source of the coupling were known, steps could be taken to try to remove it.

There are a number of possible explanations for the coupling. The solenoid couples the transverse planes. Poor steering through the linac or the gun can also lead to non-linear rf effects which can couple the beam and which would give rise to a time dependent

coupling. Other factors could include wake fields, a spatial chirp in the laser, and non-uniform emission from the cathode.

Definition of Beam Size in the Presence of Cross Plane Coupling

Given the correlation that is evident in the beam, it is important to determine the most physical interpretation of the spot size. This is especially important since the experimental conditions did not allow for a precise determination of the full four by four transverse beam matrix. If the origin of the coupling were known, the appropriate interpretation of the horizontal spot size would be easier to determine. One choice would be to reorient the ellipse axes in its unrotated coordinates; however, since the (net) effect of the quadrupoles is mainly in one plane (and the rotation changes with quad strength), this appears to be inappropriate. If the coupling can be described by a rotation in the phase space (such that the skew quad could completely remove its effect) *before* the quadrupole, then the distance from the beam center to the "one σ " contour is probably the best description of the beam size. This will be the definition that the emittance measurements reported here will be based on. This definition will be referred to as *on-axis* spot size. It is equivalent to the rms spot size of a single slice of the beam taken through the first moment about the orthogonal axis for a self similar beam. The spot size squared will be referred to as σ_{11}^{2D} in contexts where it may be confused with σ_{11} of the full transverse phase space (namely $\langle x^2 \rangle$).

Fig. 6.17 shows graphically the difference between the rms spot size and our definition of σ_{11}^{2D} for a correlated beam. It should be stressed that if a four by four beam-matrix were used, coupling between the planes could be correctly included. Then the true second moment would be the correct definition of the spot sizes, and the determinant of

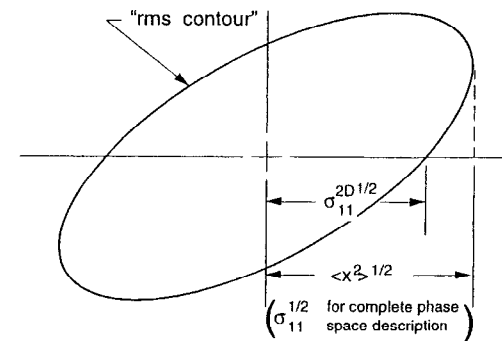


Figure 6.17: Spot size definition.

the four by four beam matrix would give us the product of the vertical and horizontal emittances. In Appendix B more details on rotated ellipses are to be found.

6.2.4 Operating Parameters

Many parameters determine the beam emittance. Some can be readily varied such as the gun gradient and phase, the linac gradient and phase, the solenoid strength, the beam charge, and, of course, the transverse and longitudinal profile of the laser. Parameters which are difficult to vary include the distance between the gun and the linac and the cathode material. Parameters which essentially cannot be changed include the rf frequency, the laser frequency, and the gun design.

The operating gradients and phases of the linac and the gun were fixed for the data reported here. The gradient in the gun was chosen at approximately 110 MV/m as a

balance between a high gradient and a “reasonable” dark current. The “reasonable” dark current level was determined both by an experimental consideration (the background on the phosphor screen) and by a practical consideration (keeping the average current below the radiation safety “trip” levels). The gun phase was chosen to be 50° with respect to the zero crossing as determined in Section 6.1.2. This was chosen to be as far ahead of crest as was reasonable while still maintaining a reasonable quantum efficiency as well as to be near the maximum energy and minimum energy spread condition. It was felt that using the QE rather than the energy for determining the operating position yielded more reproducible results.

The gradient in the linac was chosen to be ~ 10 MeV/m and the phase was chosen at approximately 10° ahead of the crest (compression). These values were chosen mainly from an operational point of view. The linac phase was determined by assigning the maximum energy gain to the crest. The beam energy as measured by a dipole spectrometer was 35 ± 0.25 MeV under these conditions. Simulations suggest that lower gradients in the linac will tend to produce lower emittance beams (for the current gun to linac distance). And, indeed, the lowest emittance measured to date at the GTF has been at approximately 6 MeV/m [100]. However, at larger energies the energy spread was considerably smaller making the absolute phase measurement easier.

The laser parameters were chosen to vary the density of the electron beam by changing the length, the charge (by changing the energy in the laser pulse), and the transverse profile (either Gaussian or clipped Gaussian). This included the following conditions: The transverse spot size was fixed at 0.8 x 1.3 mm Gaussian (or clipped at 1 mm) as measured by a CCD camera. The astigmatism in the regen and the pulse compressor in combination with the frequency doubling process seem to cause the non-unity aspect ratio. The longitudinal profile of the laser was 5 ps and 8 ps (Gaussian) and 11 ps

Table 6.1: Experimental conditions for emittance data.

τ_{laser} [ps FWHM]	$\sigma_{x,y}^{laser}$ [mm]	charge [nC]
5 ps ^a	1.3 x 0.8 ^b	1
8 ps ^a	1.3 x 0.8 ^b	1
11 ps ^c	1.3 x 0.8 ^b	0.7 ^d
5 ps ^a	1.3 x 0.8 ^b	0.5
8 ps ^a	1.3 x 0.8 ^b	0.5
5 ps ^a	1.3 x 0.8 ^e	0.5

All data at 110 MeV/m 50° gun, 10° linac, 35 MeV.

Solenoid 1.8–2.3 kG in steps of 0.1 kG.

^a Gaussian longitudinal

^b Gaussian transverse

^c “Quasi-flat” longitudinal

^d 1 nC for 1.8, 1.9 kG

^e Clipped at 1 mm transverse

(quasi-flat) as measured on a streak camera (Section 4.9.2). The charge was ~ 0.5 , 0.7, and 1.0 nC as determined periodically with a Faraday cup, and monitored using the Laser energy and a toroid after the linac. The Solenoid was varied in steps of 7 A (~ 0.1 kG) over seven settings for each condition in order to observe the best emittance-compensation. Not all combinations of the above conditions were performed. Table 6.1 summarizes the experimental conditions.

6.2.5 Beam Cuts

In addition, to the image, on each "shot" a number of parameters were measured to determine if the beam conditions have changed. A Joule meter was used to sample the laser energy, and a toroid after the linac the beam current. The field and phase in the gun as well as the phase in the linac were measured to determine the rf stability. For each scan a histogram of all measured parameters was produced and cuts were determined based on deviations from the average values. Conditions were, for the most part, quite stable and few events needed to be cut. A single cut on the gun probe (power) was placed for events which fell that $\pm 1\%$ of the average for the entire data. This cut removed any events that were likely to coincide with an electrical breakdown in the gun. The gun phase was stable to within $2\text{--}3^\circ$ peak-peak, and the linac phase was stable to better than 2° for the events that survived the field cut such that no additional cut was placed on the phase. For most conditions a $\pm 10\%$ cut on the average laser energy was used. The two exceptions are the 0.5 nC clipped Gaussian case where a 15% cut was utilized, and the 1 nC, 11 ps data which suffered from a droop in the laser energy from the low solenoid setting to the high. Separate cuts were placed on the 1.8 kG, 1.9 kG and 2.0–2.3 kG data—in this case the first two cuts were approximately 1 nC and the latter was approximately 700 pC. No cuts were placed on the beam toroid.

All of the parameters that met the beam cuts were then processed according to the method given in Section 6.2.3. Additional cuts were placed if the beam was not completely within the bounds of the screen in the horizontal plane, if the calculated moments were unphysical, or if the integrated background image was greater than the integrated signal image.

Table 6.2: Projected transverse emittance summary.

charge [nC]	τ_{laser} [ps FWHM]	$\epsilon_{n,\text{rms}}$ [π mm-mrad]	χ_{dof}^2	solenoid [kG]	spotsizes [mm]	note
1	5 ps	$12.9 \pm 0.5 \pm 2.4$	3.3	2.2	0.45	^a
1	8 ps	$13.5 \pm 2.1 \pm 2.5$	0.33	2.0	0.53	^a
1	11 ps	$12.2 \pm 0.2 \pm 2.3$	2.4	2.1	1.3	^{a,b}
0.5	5 ps	$10.5 \pm 0.2 \pm 2.0$	1.3	2.0	0.50	^a
0.5	8 ps	$8.0 \pm 1.3 \pm 1.5$	0.68	2.0	0.44	^a
0.5	5 ps	$15.6 \pm 3.1 \pm 2.9$	2.1	2.0	0.55	^c

^a 0.8 x 1.3 mm Gaussian at cathode

^b 0.7 nC at minimum

^c $\sim 1\sigma$ clipped transverse

6.2.6 Horizontal Emittance Results

The projected transverse emittance was measured as a function of pulse width and charge. The solenoid was varied in steps of 7 A (~ 0.1 kG) for each condition to try and experimentally determine the best emittance-compensation, and a quadrupole scan was performed at each solenoid setting. In Table F.1 of Appendix F, the data for each scan (obtained from a least squares fit to the individual quadrupole scans) is summarized while Table 6.2 summarizes the minimum emittance for each condition.

The emittance is the normalized rms-transverse emittance where the "on-axis" width is used for the spotsizes, as defined in Section 6.2.3. The first error is the estimated error from the "error-matrix" obtained from the least squares fit and are not scaled to the reduced chi-square, the second error is the systematic error due to uncertainties in the

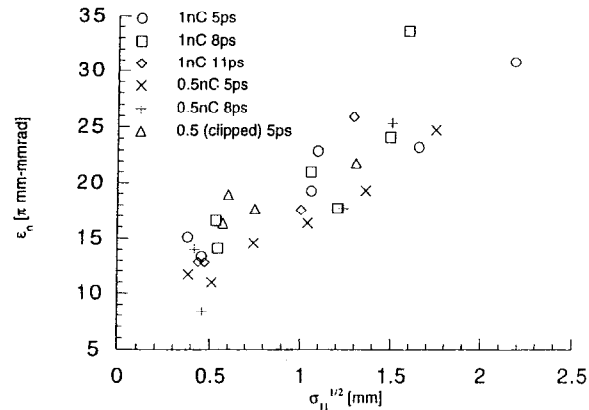


Figure 6.18: Emittance as a function of spot-size before the first quadrupole for all beam conditions.

pixel calibration, and χ_{dot}^2 is the reduced chi-square. Additional systematic errors due to the beam energy measurement, the field gradient and the drift distance are small and are neglected here. Fig. 6.11 on page 141 shows the results of a typical quad scan. The results of the quadscans minimum emittances are given in Appendix F.

The spotsize before the first quadrupole (Q1) was calculated (by projecting the calculated beam ellipse from Q2 backwards) for all of the data. Fig. 6.18 shows the emittance as a function of the spotsize before the first quadrupole for all of the data taken. The figure shows that the minimum emittance occurs near the minimum spotsize.

Emittance as a Function of Laser Pulse Length

Fig. 6.19 shows the results of the measured emittance versus solenoid focusing strength for various laser pulse lengths at 1 nC of charge. Within the error bars of the measure-

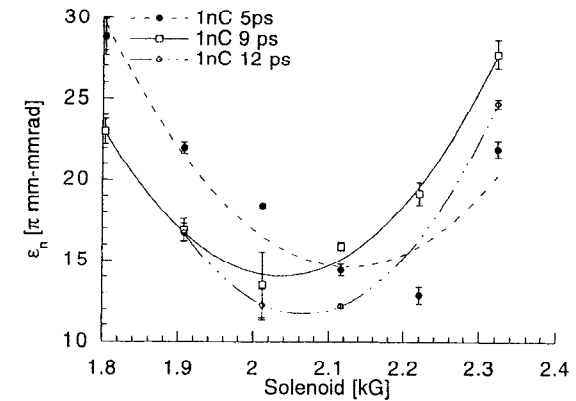


Figure 6.19: Emittance as a function of solenoid field for 1 nC of charge and different pulse widths.

ment no significant change was seen by lengthening the pulse from ~ 5 ps to ~ 8 ps; however, it is noticed that the minimum emittance in the 8 ps case occurs at a lower field in the solenoid. This is consistent with less defocusing due to the longitudinal space-charge force for the longer beam. The 11 ps data also shows this trend and perhaps a slightly lower emittance than the 8 ps; however the charge may have been as low as 700 pC in this case. The minimal effect of the pulse length on the emittance (at 1 nC) suggests that either our emittance is not dominated by space-charge (the gain in lowering the space-charge contribution to the emittance was balanced by an increase in the non-linear rf emittance), or possibly that the beam has quickly (due to the stronger space-charge) reordered itself to similar densities.

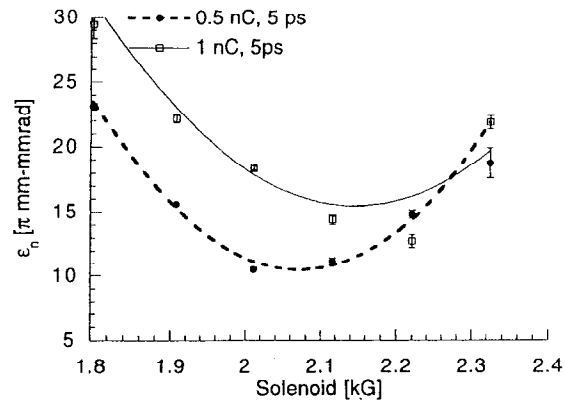


Figure 6.20: Emittance as a function of Solenoid for the 0.5 and 1 nC, 5 ps data.

Emittance as a Function of Charge

The emittance is shown as a function of charge in Fig. 6.20 for the 5 ps data and Fig. 6.21 for the 8 ps data. For both pulse lengths, a decrease in the minimum emittance is seen as the charge is reduced from 1 nC to 0.5 nC. In the 5 ps case, the emittance decreases from $12.9 \pm 0.5 \pi$ mm-mrad to $10.5 \pm 0.2 \pi$ mm-mrad, and in the 8 ps case the emittance decreases from $13.5 \pm 2.1 \pi$ mm-mrad to $8.0 \pm 1.3 \pi$ mm-mrad. It is also seen for the 5 ps case that less focusing is required by the solenoid for the lower density beam.

Emittance as a Function of Transverse Laser Profile

In Fig. 6.22, the rms emittance as a function of the solenoid focusing strength is shown for 0.5 nC charge but two different transverse (laser) profiles. The open circles use

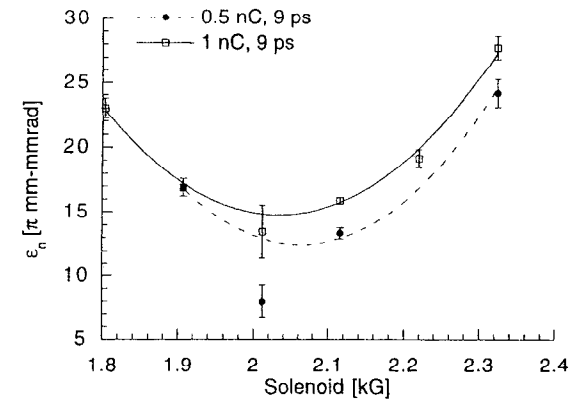


Figure 6.21: Emittance as a function of Solenoid for the 0.5 and 1 nC, 8 ps data.

the full Gaussian transverse profiles ($\sim 0.8 \times 1.3$ mm) of the laser while the solid squares utilize a 1 mm clipped Gaussian. Here the emittance is increased from $10.5 \pm 0.2 \pi$ mm-mrad to $15.6 \pm 2.9 \pi$ mm-mrad when replacing the full Gaussian with the clipped Gaussian. Because the total charge is the same in each case the electron beam produced by the clipped Gaussian will have an initially higher charge density. This leads one to believe that the higher space-charge force may account for the difference. However, the clipped Gaussian has the same initial charge density as the central ($\sim 50\%$) core of the 1 nC data where the emittance was measured at $12.9 \pm 0.5 \pi$ mm-mrad. While the two are within the errors of each other, one would expect a lower emittance in the clipped Gaussian case due to the more uniform space-charge forces. One possible source of the discrepancy lies in the definition of the rms emittance: namely the difference in the number of particles included for different beam profiles; for example, for the same volume in phase space a uniform distribution will have twice the charge as

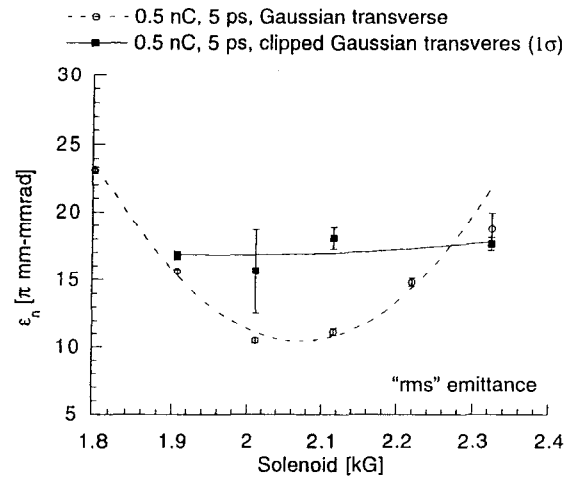


Figure 6.22: Emittance (rms) as a function of solenoid field for 0.5 nC for the transverse Gaussian and clipped Gaussian data.

a Gaussian when the volume is determined by the rms spotsize and divergence. This can be seen in Fig. 6.23 which is the same data analyzed utilizing a spotsize which includes 39% of the beam. If the beam distribution were Gaussian this should be equivalent to the rms emittance. In this case, the full transverse Gaussian emittance has increased slightly to $12.9 \pm 0.5 \pi \text{ mm-mrad}$ while the clipped Gaussian emittance is decreased to $8.7 \pm 4.1 \pi \text{ mm-mrad}$. Table 6.3 summarizes the minimum emittance for each case.

6.3 Conclusions

The horizontal emittance of the electron beam was measured after acceleration to 35 MeV, using a standard quadrupole scan for a variety of parameters. At each condition, the

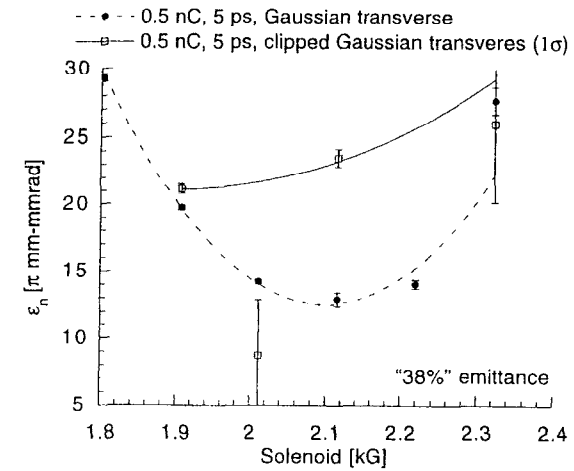


Figure 6.23: Emittance (39%) as a function of solenoid field for 0.5 nC for the transverse Gaussian and clipped Gaussian data.

solenoid field was varied such that the minimum emittance due to emittance-compensation could be observed. The measured minimum emittances for 1 nC of charge at various laser pulse are almost identical in value. Changing the pulse length from 5 ps to 8 picoseconds resulted in less need for focusing in order to obtain the corresponding minimum. This indicates that, either the emittance is not dominated by space-charge effects, or that the reduction of space-charge was accompanied by an equivalent increase in the rf effects on the emittance. PARMELA simulations run under similar conditions¹ show a similar trend with emittances of $8.3 \pi \text{ mm-mrad}$ at 2.2 kG and 5 ps and $7.6 \pi \text{ mm-mrad}$ at 2.1 kG[55] for 8 ps. However, any possible bunch lengthening effects are not contained in the model. Summaries of these simulations are given in Table 6.4.

¹except $\sigma_x = \sigma_y = 1.4 \text{ mm}$

Table 6.3: Projected transverse emittance for the data analyzed with a definition of the emittance based on 39% of the beam.

charge [nC]	τ_{FWHM} [ps]	$\epsilon_{n,39\%}$ [π mm-mrad]	χ_{dof}^2	solenoid [kG]
1	5 ps	$11.9 \pm 0.9 \pm 2.2$	1.1	2.2
1	8 ps	$19.1 \pm 2.7 \pm 3.6$	0.5	2.0
1	11 ps	$12.2 \pm 0.2 \pm 2.3$	5.0	2.0
0.5	5 ps	$12.9 \pm 0.5 \pm 2.4$	2.5	2.0
0.5	8 ps	$12.6 \pm 2.4 \pm 2.4$	0.7	2.0
0.5	5 ps	$8.7 \pm 4.1 \pm 1.6$	2.2	2.0

If the beam emittance were dominated by non-linear space-charge forces, decreasing the charge would have a large effect on the emittance. The 5 ps data showed an approximately 20% decrease in the emittance as the charge was decreased by a factor of two, while the 8 ps data showed an approximately 40% decrease. The larger effect that reducing the charge had on the 8 ps data contrasts with the possibility that non-linear rf forces may have been counteracting the space-charge decrease in the 1 nC data. Again, simulations were run that showed a decrease of 23% in the 5 ps case and 24% in the 8 ps case.

Finally, comparison of the clipped transverse profile to the full Gaussian profile showed an approximately 33% decrease in the 39% emittance, presumably due to the more uniform transverse profile. However, the rms emittance of the clipped Gaussian profile increased by almost a factor of two from the difference in the profiles of the electron beams, and this suggests that non-linear transverse forces are not the dominant cause of increased beam emittance.

Table 6.4: Comparison of selected emittance measurements (transverse Gaussian) with simulation [55].

charge [nC]	τ_{laser} [ps FWHM]	$\epsilon_{n,rms}^a$ [π mm-mrad]	solenoid [kG]	$\epsilon_{n,rms}^{simulation}$ [π mm-mrad]	solenoid [kG]
1	5 ps	$12.9 \pm 0.5 \pm 2.4$	3.3	8.34	2.2
1	8 ps ^b	$13.5 \pm 2.1 \pm 2.5$	2.0	7.58	2.1
0.5	5 ps	$10.5 \pm 0.2 \pm 2.0$	2.0	6.65	2.1
0.5	8 ps ^b	$8.0 \pm 1.3 \pm 1.5$	2.0	5.78	2.05

^a Simulation has $\sigma_{x,y} = 1.4$ mm.

^b Simulation at 9 ps.

The results presented here yield larger effects than the estimated values given in Chapter 2, and are 40–80% larger than simulations. It is believed that this is due to a large contribution of the emittance from a relatively small portion of the beam (the halo). This halo was seen to evolve differently from the bulk of the beam and could not be removed in the data reduction. Non-linear rf and space-charge forces acting on the tails of the beam can contribute to the halo. The discrepancy cannot be explained completely by tails in the transverse profile as can be seen by the data taken with the transversely clipped laser. Nonetheless, any non-linear force acting on the beam will tend to produce a beam halo. The longitudinal pulse shaping described in Chapter 4 should therefore prove valuable in any future development of this work.

The conditions reported here were not optimal from a theoretical perspective but were considered necessary from an operational point of view. For example, optimal emittance-compensation is anticipated for fields around 140 MV/m [56]. PARMELA simulations indicate that, for the present distance between the gun and linac, more efficient

emittance-compensation is achieved for a lower linac gradient. This is believed to be due to better matching of the rf-focusing in the linac at lower gradients [100]. The phase in the gun may also not have been optimal. In fact, steps were taken to minimize the longitudinal phase space out of the gun which would tend to increase the transverse phase space. However, this is not enough to explain the discrepancy in the measurements. It is possible that a significant halo is formed through wakefields from either the laser mirror or poor steering through the linac. Unfortunately, rf effects in the linac were also not explored.

Non-uniformities in the photocathode can contribute to an increased emittance. The "laser cleaning" process was found to increase the localized field at the cathode. This has an effect on the thermal emittance of the beam as electrons emitted at a site of large enhancement will have larger energy spread. With the measured enhancement, the difference between the photon energy and the work function can be as much as 4 eV. The thermal emittance of these electrons will be $\sim 4 \pi$ mm-mrad per millimeter. In addition, the localized field enhancement can cause hot-spots in the beam, leading to a much higher localized space-charge field that cannot be fully compensated.

Laser related background causes emission outside of the main electron bunch. Because the emittance measurements are not temporally resolved, it is likely that this background could cause an apparent increase in the emittance. Pre- or post-pulses on the laser can be neglected, as long as the Pockels' cell timing is set correctly. This appears to be the case as the measured contrast ratio of the laser pulse in the IR is well over 750 to 1 (see Fig. 4.4). In addition, there is further improvement in the contrast ratio from the non-linearity of the frequency conversion process. The laser pulse reflected off of the cathode does not contribute to additional emission from the gun, because it is unlikely that the light makes it back to the center of the cathode. It is possible, however,

that an etalon in one of the crystals, in the laser transport lenses, or in the laser window can make it to the cathode. Because all of these optics are anti-reflection coated, etalon effects should be minimal; however, if the pulse is sufficiently off temporally or spatially, it is conceivable that it can have a finite effect on the measured emittance. In addition to laser related background caused by photoemission, there can be increases in the thermal emission from the cathode due to localized heating. For the laser energies, and spotsizes used here this effect is expected to be negligible.

In order to meet the goals of the LCLS, a more detailed search of the parameter space is needed. Work has begun on measuring the full 6-Dimensional phase space at the GTF. Streak camera images of the longitudinal profile of the electron beam will enable time resolved emittance measurements and will help clarify if there is any laser related background outside of the main pulse. The framework for more sophisticated longitudinal shaping of the laser is in place and will enable measuring the emittance not only as a function of longitudinal pulse length but also of pulse shape. It has been shown that best emittance-compensation emittance occurs near the waist of the beam. This should help in the search the parameter space in the future; however, because there are so many correlated parameters, a single-shot measurement of the emittance would be perhaps the most useful addition to the instrumentation.

Work is also in progress in determining the best technique for preparation of the photocathode. This is important, both for a uniform emission from the cathode, and for reducing the field-emitted backgrounds, while maintaining a high quantum efficiency. The current gun is tentatively scheduled to be moved to an off axis injector site on the SLAC linac in early 2001, at which time new guns could be tested at the GTF. This gun could be another standing wave TM cavity based gun or, for example, be plane-wave transformer or pulsed diode gun, both of which show promise as low emittance sources.

References

- [1] LCLS parameters from [3].
- [2] M. Cornacchia. Performance and design concepts of a free electron laser operating in the X-ray region. In *SPIE, Free-Electron Laser Challenges*, volume 2988, pages 90–96, San Jose, 1997.
- [3] The LCLS Design Study Group. LCLS design study report. Technical report, SLAC-R-521, 1998.
- [4] M. Borland. A high brightness thermionic microwave electron gun. SLAC-R-0402.
- [5] R. Alley et al. The stanford linear accelerator polarized electron source. *Nucl. Instrum. Meth.*, A365:1–27, 1995.
- [6] R.L. Sheffield. Photocathode rf guns. In *Physics of Particle Accelerators*. AIP, 1992.
- [7] H. Winick. The linac coherent light source LCLS: a fourth-generation light source using the SLAC linac. *Journal of Electron Spect and Related Phen.*, 76:1–8, 1995.
- [8] B.E. Carlsten. New photoelectric injector design for the Los Alamos National Laboratory XUV FEL Accelerator. *Nucl. Instrum Methods Phys. Res.*, A285:313, 1989.
- [9] Using a 2 screen method [38] finds $4.74 \pm 0.24 \pi$ for 1 nC.
- [10] M. Hernandez et al. Emittance measurements for the SLAC gun test facility. In *IEEE Particle Accelerator Conf.*, 1997.
- [11] D.T. Palmer et al. Emittance Studies of the BNL/SLAC/UCLA 1.6 cell Photocathode rf Gun. In *IEEE Particle Accelerator Conf.*, 1997.
- [12] X. Ding et al. The development of S band plane wave transformer photoinjector. In *IEEE Particle Accelerator Conf.*, New York City, 1999.

- [13] T. Srinivasan-Rao et al. Simulation, generation and characterization of high brightness electron source at 1 GV/m gradient. In *IEEE Particle Accelerator Conf.*, New York City, 1999.
- [14] Luis R. Elias et al. Observation of stimulated emission of radiation by relativistic electrons in a spatially periodic transverse magnetic field. *Physical Review Letters*, 36(13):717–720, 1976.
- [15] OK-4 FEL, Duke University.
- [16] UVSOR Facility, Institute for Molecular Science, Okazaki, JAPAN.
- [17] NIJI-I, VETL, Tsukuba, Japan.
- [18] Free Electron Laser Research Institute, Inc.(FELI), Osaka, Japan.
- [19] FOM-Institute for Plasma Physics Rijnhuizen, The Netherlands.
- [20] Tel Aviv University, Israel.
- [21] Compact Free Electron Laser, Frascati, Italy.
- [22] A list of operational Free Electron Lasers is maintained on the World Wide Web at <http://sbfel13.ucsb.edu/www/v1.fel.html>.
- [23] R.H. Pantell. Comparisons between the FEL and the conventional laser. *Nucl. Instrum. and Meth.*, A304:798–803, 1991.
- [24] C. Pellegrini and J.B. Murphy. Introduction to the physics of the free electron laser. In *Laser Handbook*, volume 6. North-Holland, 1990.
- [25] J.D. Jackson. *Classical Electrodynamics*. John Wiley and Sons, 2 edition, 1975.
- [26] R. Bonifacio, Pellegrini C., and Narducci L.M. Collective instabilities and high gain regime in a free-electron laser. *Opt. Commun.*, 50(6), 1985.
- [27] M. Xie. Design Optimization for an X-ray Free Electron Laser Driven by SLAC Linac. Presented at 16th IEEE Particle Accelerator Conference (PAC 95) and International Conference on High Energy Accelerators (IUPAP), Dallas, Texas, 1-5 May 1995.
- [28] J.F. Schmerge et al. SLAC RF photocathode gun test facility. In *SPIE, Free-Electron Laser Challenges*, volume 2988, pages 2–14, San Jose, 1997.
- [29] D. Strickland and G. Mourou. Compression of amplified-chirped optical pulses. *Opt. Comm.*, 55:447, 1985.

- [30] E. D. Palik. *Handbook of Optical Constants of Solids II*, chapter 7. Academic Press, Inc., Harcourt Brace Jovanovich, 1991.
- [31] C. Kittel. *Introduction to Solid State Physics*. John Wiley & Sons, Inc., 6th edition, 1986.
- [32] A. C. Melissinos. *Experiments in Modern Physics*. Academic Press, Inc., 1966.
- [33] J. W. Wang. Rf properties of periodic accelerating structures for linear colliders. SLAC-0339.
- [34] R.H. Fowler and L.W. Nordheim. *Proc. Roy. Soc. (London)*, A(119):173, 1928.
- [35] M. Cardona and L. Ley. Photoemission in solids I. In *Topics in Applied Physics*, volume 26. Springer Verlag, 1980.
- [36] R.H. Fowler. *Phys. Rev.*, 39:45, 1931.
- [37] R. Gomer. *Field Emission and Field Ionization*. Harvard University Press, 1961.
- [38] D. T. Palmer. *The Next Generation Photoinjector*. PhD thesis, Stanford University, 1998.
- [39] Born and Wolf. *Principles of Optics*. Cambridge University Press, 6th corrected edition, 1997.
- [40] K Kim. RF and space-charge effects in laser-driven RF electron guns. *Nucl. Instrum Methods Phys. Res.*, A275:201–218, 1989.
- [41] E.R. Colby. *Design, Construction, and Testing of a Radiofrequency Electron Photoinjector for the Next Generation Linear Collider*. PhD thesis, University of California, Los Angeles, 1997.
- [42] Field map from SUPERFISH courtesy of D. T. Palmer.
- [43] P. B. Wilson. High energy electron linacs: Applications to storage ring rf systems and linear colliders. Technical report, SLAC-PUB-2884, 1982. The shunt impedance is defined here without the factor of 2.
- [44] D.A. Edwards and M.J. Syphers. *An Introduction to the Physics of High Energy Accelerators*. John Wiley and Sons., 1993. The shunt impedance is defined here without the factor of 2.
- [45] K.L. Brown, F. Rothacker, D. Carey, and Ch. Iselin. *Transport*. SLAC-91,CERN-73-16,NAL-91, 1977.
- [46] H. Wiedemann. *Particle Accelerator Physics*. Springer Verlag, 1993.

- [47] D. Carcy. *The Optics of Charged Particle Beams*. Harwood Academic Publishers, 1987.
- [48] A.E. Siegmann. *Lasers*. University Science Books, 1986.
- [49] A. Yariv. *Optical Electronics*. CBS College Publishing, 3rd edition, 1985.
- [50] K.-J. Kim. Quantum fluctuations in beam dynamics. In P. Chen, editor, *Quantum Aspects of Beam Physics*. World Scientific, 1999.
- [51] J.E. Clendenin and G.A. Mulhollan. High quantum yield, low emittance electron sources. In *15th ICFA Advanced Beam Dynamics Workshop*, 1998.
- [52] PARMELA, Lloyd Young, Los Alamos National Lab.
- [53] Hernandez, M. private communication.
- [54] D. T. Palmer et al. Microwave measurements of the bnl / slac / ucla 1.6 cell photocathode rf gun. Presented at 16th IEEE Particle Accelerator Conference (PAC 95) and International Conference on High Energy Accelerators (IUPAP), Dallas, Texas, 1-5 May 1995.
- [55] PARMELA simulations are provide courtesy of M. Hernandez. The conditions were the same as in the experiments except that a 1.4 mm symmetric Gaussian is used for the transverse profile. The numbers given are for the optimum solenoid fields. Future studies will be included as part of M. Hernandez's PhD. thesis.
- [56] M. Hernandez et al. Emittance measurements for the SLAC gun test facility. In *IEEE Particle Accelerator Conf.*, 1997.
- [57] D. T. Palmer and E. Colby, private communications.
- [58] see ref. [38], for example.
- [59] HP 8510, Network Analyser.
- [60] J. N. Weaver. Effect of temperature, barometric pressure, and relative humidity on a resonant cavity frequency. Technical Report HEPL-TN-68-4, High Energy Physics Laboratory, Stanford University, 1968.
- [61] P. B. Wilson. High energy electron linacs: Applications to storage ring rf systems and linear colliders. Technical report, SLAC-PUB-2884, 1982. See for example.
- [62] Mike Hernandez private communication May 1999.
- [63] M. Siedel et al. Absolute beam position measurement in an accelerator structure. *Nuclear Instrum and Meth.*, A404:231–236, 1998.

- [64] This result can be found, for example, in [46].
- [65] S. Yenko and D.R. Walz. A high resolution Phosphor screen beam profile monitor. *IEEE Trans.*, 32:2009–2011, 1985.
- [66] W. S. Graves. A high resolution electron beam profile monitor. In *IEEE Particle Accelerator Conf.*, 1997.
- [67] S. Gierman, 1999. Ph.D. dissertation to be submitted to the University of California, San Diego.
- [68] W. P. Leemans, R. W. Schoenlein, P. Volfbeyn, A. H. Chin, T. E. Glover, P. Balling, M. Zolotarev, K. Kim, S. Chattopadhyay, and C. V. Shank. X-ray based subpicosecond electron bunch characterization using 90 degrees Thomson scattering. *Physical Review Letters*, 77:4182, 1996.
- [69] X. Qui, K. Batchelor, I. Ben-Zvi, and X.-J. Wang. Demonstration of emittance compensation through the measurement of the slice emittance of a 10-ps electron bunch. *Phys. Rev. Letters*, 76(20):3723–3726, 1996.
- [70] FC1 and FC2 are based on a design at use at the Accelerator Test Facility at Brookhaven National Lab.
- [71] American Institute of Physics. Particle physics booklet, 1996.
- [72] Bergoz Toroid FCT 082-5:2.
- [73] SLAC style beam toroid.
- [74] J.B. Rosensweig. rf photoinjectors: A guide to performance requirements and demands on laser systems. In *Lasers for rf Guns*, 1994.
- [75] W. Koehler. *Solid-State Laser Engineering*. Springer Verlag, 3rd edition, 1992.
- [76] Magnum Model TLS22-06.
- [77] Time-Bandwidth Products, model GLX-200, Zurich.
- [78] U. Keller et al. Semiconductor saturable absorber mirrors SESAMs for femtosecond to nanosecond pulse generation in solid-state lasers. *JSTQE*, 1996.
- [79] J. Jansky, G. Corradi, and R.N. Gyuzalian. On a possibility of analysing the temporal characteristics of short light pulses. *Optics Commun.*, 23(3):293–298, 1977.
- [80] K.L. Sata, A. Kenney-Wallace, and G. E. Hall. CW autocorrelation measurements of picosecond laser pulses. *IEEE Journal of Quantum Electronics*, QE-16(9):990–996, 1980.

- [81] O.E. Martinez et al. *J. Opt. Soc. Am.*, A1:1003, 1984.
- [82] E. B. Treacy. Optical pulse compression with diffraction gratings. *IEEE J. Quantum Electronics*, QE-5(9):454–458, 1969.
- [83] C. Bamber et al. *Laser Physics*, 7:135, 1997.
- [84] Simulations provided by Steve Craxton, University of Rochester, Laboratory for Laser Energetics, Rochester, NY.
- [85] From the treatment in [103] scaled from data on 50 ns ruby laser.
- [86] Hamamatsu, model FESCA-500, streak camera, UV optics courtesy of B. Cieslik, Hamamatsu.
- [87] F. Salin, P. Georges, G. Roger, and A. Brun. Single-shot measurement of a 52-fs pulse. *Applied Optics*, 26(21):4528–4531, 1987.
- [88] C.W. Siders and A.J. Taylor. High-energy pulse train and shaped pulse generator using a “100%” throughput 2nd-pulse Michelson interferometer. In *Ultrafast Opt. Conf.*, Monterey, CA, 1997.
- [89] A. M. Weiner, J. P. Heritage, and E. M. Kirschner. High-resolution femtosecond pulse shaping. *Journal of the Optical Society of America*, B5:1563, 1988.
- [90] X.D. Cao, L. Zheng, and D.D. Meyerhofer. Measurement of group-velocity walk-off of short pulses in nonlinear crystals: a novel method. *Opt. Lett.*, 20(4):392–394, 1995.
- [91] Ocean Optics, S2000 spectrometer.
- [92] Watkins Johnson, Model MIG.
- [93] S. R. Kurtz. Mixers as phase detectors. Technical report, Watkins-Johnson Co., 1978.
- [94] T. Kotseroglou et al. Picosecond timing of terawatt laser pulses with the SLAC 46-GeV electron beam. *Nucl. Instrum. Meth.*, A383:309–317, 1996.
- [95] Hewlett Packard 8662A low noise synthesiser.
- [96] M.J.W. Rodwell, D.M. Bloom, and K.J. Weingarten. Subpicosecond laser timing stabilization. *IEEE Journal of Quantum Electronics*, 25(4):817–827, 1989.
- [97] Moletron, J409 laser pyroelectric energy meter.
- [98] X.J. Wang et al. Intense electron emission due to picosecond laser produced plasmas in high gradient electric fields. *J.Appl.Phys.*, 72(3):888–894, 1992.

- [99] M. Reiser. *Theory and Design of Charged Particle Beams*. Wiley, New York, 1994.
- [100] D. A. Reis, M. Hernandez, J. F. Schmerge, H. Winick, and M. J. Hogan. Transverse emittance measurements from a photocathode rf gun with variable laser pulse length. Contributed to 20th International Free Electron Laser and 5th Free Electron Laser Users' Workshop (FEL 98), Williamsburg, VA, 16-21 Aug 1998.
- [101] Pulnix Model TM-7EX.
- [102] Data Translation Model DT 3852-8.
- [103] Y. R. Shen. *The Principles of Nonlinear Optics*. John Wiley and Sons, Inc., 1984.
- [104] O. E. Martinez. Grating and prism compressors in the case of finite beam size. *J. Opt. Soc. Am. B.*, 3(7):929-934, 1986.

Appendix A

LCLS Design Requirements

Table A.1: LCLS design parameters [1]

Undulator Type	planar NdFe:B	
Wavelength	1.5	Å
Norm. RMS Emittance	1.5	π mm mrad
Peak Current	3.4	kA
Electron Energy E	15	GeV
Average β -Function	18	m/rad
σ_E/E	0.021	%
Pulse Duration (FWHM)	280	fs
Pulses per macropulse	1	
Repetition Rate	120	Hz
Undulator Period	3.0	cm
Peak Field	1.32	T
FEL parameter ρ	0.47	10^{-3}
Power Gain Length	5.8	m
Saturation Length	94.1	m
Peak Power	9.2	GW
Average Power	0.28	W
Coherent Energy per Pulse	2.3	mJ
Coherent Photons per Pulse	1.8	10^{12}
Peak Brightness	6.1	10^{32} *
Average Brightness	2.8	10^{21} *
Transverse RMS Photon Beam Size	31	μ m
Transverse RMS Photon Beam Divergence	0.39	μ rad

* photons/(s,mm²,mrad²,0.1%BW)

Appendix B

Description of Beam Ellipses

Ellipses are used throughout accelerator physics because of their mathematical simplicity. The various phase spaces of the beam are described as ellipses which scale with the rms beamsizes and divergence angles. The entire phase space of the beam is described by a 6-Dimensional “hyper-ellipse”. It is often supposed that this 6-Dimensional ellipse can be broken up into 3, 2-Dimensional sub-spaces described by 3 different 2-Dimensional ellipses—the phase space volume then being the product of the areas of the 3 ellipses. If the phase spaces are coupled, then this statement is not true. The various areas of the ellipses are then representative of a projected phase space area.

For example, the emittance measurement based on a quadrupole scan utilizing a phosphor screen lacks sufficient temporal resolution to measure the beam width as a function of longitudinal coordinate. The result is that the measurement gives a time (and energy) projected emittance. The emittance-compensation solenoid can remove (or add) correlation and thus changes the temporally projected transverse emittance—but *not* the phase space density. Likewise, coupling between the two transverse planes will lead to a projected emittance if the full rms beam size is used.

Regardless of correlations, the 2-Dimensional ellipse is an important tool. The ellipse can be used to not only describe the (x, x') phase space but also the (x, y) transverse space. There are many different mathematical ways to describe an ellipse. In this appendix a number of the different descriptions are reviewed and how the various parameters are related. Fig. B.1 shows a rotated ellipse for reference. The two coordinates, x and y are used; however the results are, of course, general to any two coordinates.

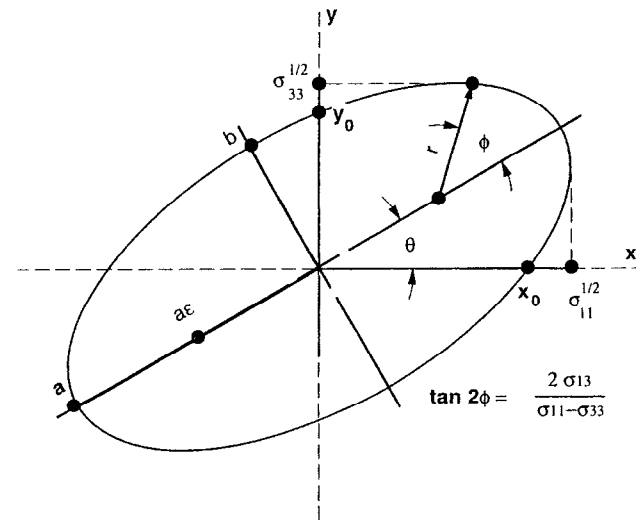


Figure B.1: Rotated ellipse.

B.1 Upright Ellipse in Cartesian Coordinates

The equation for an upright ellipse in cartesian coordinates is given simply by

$$\left(\frac{x}{a}\right)^2 + \left(\frac{y}{b}\right)^2 = 1$$

where for convenience $2a > 2b$ is taken as the major and minor axes, and the ellipse centered at $x = y = 0$. It is often convenient to describe the above in the matrix equation,

$$\begin{pmatrix} x & y \end{pmatrix} \begin{pmatrix} a^2 & 0 \\ 0 & b^2 \end{pmatrix}^{-1} \begin{pmatrix} x \\ y \end{pmatrix} = 1. \tag{B.1}$$

The matrix, σ_{xy} , is defined by

$$\begin{pmatrix} a^2 & 0 \\ 0 & b^2 \end{pmatrix} \equiv \sigma_{xy} = \begin{pmatrix} \sigma_{11} & 0 \\ 0 & \sigma_{33} \end{pmatrix}. \tag{B.2}$$

A notation where the coordinates (x, y, x', y', z, z') are labeled by 1-6 is used. The ellipse has area

$$\text{Area} = \sqrt{\det \sigma_{xy}} = \pi ab,$$

and x and y rms's given by

$$\begin{aligned} \langle (x^2) - \langle x \rangle^2 \rangle^{\frac{1}{2}} &= \frac{a}{2} \\ \langle (y^2) - \langle y \rangle^2 \rangle^{\frac{1}{2}} &= \frac{b}{2}. \end{aligned}$$

B.2 Rotated Ellipse in Cartesian Coordinates

With the matrix definition of the ellipse given in eqs. (B.1) and (B.2), it is straightforward to transform the ellipse into a rotated coordinate system by multiplying σ on the

right and left by the unitary matrix

$$\begin{pmatrix} \cos \theta & \sin \theta \\ -\sin \theta & \cos \theta \end{pmatrix}$$

and its transpose. The new matrix will have non-zero (but symmetric) off diagonal elements, σ_{13} . The matrix is given by

$$\begin{aligned} \sigma_{11} &= a^2 \cos^2 \theta + b^2 \sin^2 \theta \\ \sigma_{33} &= b^2 \cos^2 \theta + a^2 \sin^2 \theta \\ \sigma_{13} &= (a^2 - b^2) \cos \theta \sin \theta, \end{aligned}$$

where a and b are the major and minor axis ($a^2 = \sigma_{11}, b^2 = \sigma_{33}$ in the unrotated coordinate system).

If the sigma matrix is known, the major and minor axis can be found by

$$\begin{aligned} a^2 &= \sigma_{11} \cos^2 \theta + \sigma_{33} \sin^2 \theta + \sigma_{13} \sin 2\theta \\ b^2 &= \sigma_{33} \cos^2 \theta + \sigma_{11} \sin^2 \theta - \sigma_{13} \sin 2\theta \\ \tan 2\theta &= \frac{2\sigma_{13}}{\sigma_{11} - \sigma_{33}}. \end{aligned}$$

The significance of the sigma matrix is that $\sqrt{\sigma_{11}}$ gives the x-extent of the ellipse projected along y, $\sqrt{\sigma_{33}}$ gives the y-extent of the ellipse projected along x, and of course σ_{13} gives the degree of correlation between the two. In fact, they are related to the 2nd moments of the ellipse by

$$\begin{aligned} \sigma_{11} &= 2 \langle x^2 \rangle \\ \sigma_{33} &= 2 \langle y^2 \rangle \\ \sigma_{13} &= 2 \langle xy \rangle, \end{aligned}$$

where the fact that $\langle x \rangle = \langle y \rangle = 0$ has been used. Note that the moments described here are for the ellipse *itself*! That is

$$\langle x^2 \rangle = \int_{\text{ellipse}} x^2 dx dy, \text{ etc.}$$

If the distribution in x-y is given as $f(x, y)$, and the second moments are weighted by $f(x, y)$ such that,

$$\langle x^2 \rangle = \int_{-\infty}^{\infty} \int_{-\infty}^{\infty} x^2 f(x, y) dx dy, \text{ etc.,}$$

then σ simply represents these (weighted) moments.

If the beam is rotated (as given here) in the x,y space, then the 6-D phase space is not really separable into the 3, 2-D phase spaces. The calculated emittance using a quadrupole scan in say the horizontal (x) dimension will give the projected emittance if the beam size is given as σ_{11} (or σ_{33} for a vertical scan). Much as the emittance is measured as a function of the solenoid magnetic field strength to try and find the minimum transverse-longitudinal coupling, emittance could be measured as a function of beam rotation to try and minimize the coupling between the the vertical and horizontal plane. Unlike the transverse-longitudinal coupling, however, there is adequate resolution in the projected coordinate to do better. Steps can be taken to try and minimize the coupling (by rotating the coordinate system of the measurement—in reality this is accomplished using a rotated [skew] quadrupole to rotate the beam) or by choosing a more physical definition of the beam width. The latter was the approach made here. The “approximately” uncorrelated spotsizes are defined by their extent about from the ellipse center to its edge along either coordinate. That is,

$$x_0 = \sqrt{\frac{\sigma_{11}\sigma_{33} - \sigma_{13}^2}{\sigma_{33}}}, \text{ and}$$

$$y_0 = \sqrt{\frac{\sigma_{11}\sigma_{33} - \sigma_{13}^2}{\sigma_{11}}}.$$

Note that for a beam ellipse defined by a real distribution $f(x, y)$, that this is the same as the 1-Dimensional moment only if the beam is self-similar (i.e. the 1-D spotsize in one coordinate is independent of the other).

B.3 Ellipses in Polar Coordinates

Sometimes it is convenient to work with an ellipse parameterized by an angle and distance from a focus. This can be especially helpful as it allows us to reduce 2 dimensional integrals into 1 dimensional integrals. the equation in polar coordinates is given by

$$r = \frac{\alpha}{1 + \epsilon \cos \phi},$$

where $0 \leq \epsilon < 1$, r is measured from one of the foci, and ϕ is measured from the major axis. It is straightforward to determine relationship between the cartesian and polar descriptions as

$$a = \frac{\alpha}{1 - \epsilon^2}, \text{ and}$$

$$b = \frac{\alpha}{\sqrt{1 - \epsilon^2}}.$$

Or solving for α and ϵ ,

$$\alpha = \frac{b^2}{a}$$

$$\epsilon = \sqrt{1 - \left(\frac{b}{a}\right)^2}$$

And, the relationship between the coordinates is given by

$$x = r \cos \phi + a\epsilon, \text{ and}$$

$$y = r \sin \phi.$$

The translational portion in x comes from the fact that in the polar case the ellipse is referenced to a focus while in the cartesian case it is with respect to the center.

The integrals for the various moments in $x + a\epsilon$ and y are written as

$$\int_0^{2\pi} \int_0^r y^n r dr d\phi = \int_0^{2\pi} \frac{1}{n+1} \sin^n \phi \left(\frac{\alpha}{(1 + \epsilon \cos \phi)} \right)^{n+2} d\phi$$

$$\int_0^{2\pi} \int_0^r (x + a\epsilon)^n r dr d\phi = \int_0^{2\pi} \frac{1}{n+1} \cos^n \phi \left(\frac{\alpha}{(1 + \epsilon \cos \phi)} \right)^{n+2} d\phi.$$

The first few moments are,

$$\text{Area} = \pi ab$$

$$\langle x \rangle = -a\epsilon$$

$$\langle y \rangle = 0$$

$$\langle (x^2) - \langle x \rangle^2 \rangle^{\frac{1}{2}} = \frac{a}{2}$$

$$\langle (y^2) - \langle y \rangle^2 \rangle^{\frac{1}{2}} = \frac{b}{2},$$

where $\langle x \rangle$ is non-zero because the ellipse is parameterized about one focus.

Appendix C

Expansion and Compression

C.1 Geometry

The dispersion from a diffraction grating may be used to introduce (remove) a temporal chirp from an optical pulse [82]. The grating equation is

$$\sin \theta + \sin \gamma = n \frac{\lambda}{d}, \quad (\text{C.1})$$

where $\theta(\gamma)$ are the incident (refracted) angles, n is the order of refraction, λ is the wavelength of the light and d is the groove spacing. Eq. (C.1) uses the convention that if the two angles are on the same side of normal, they have the same sign. One can see that the proper choice of d will limit refraction to only first order. For example, using a typical grating with $1/d = 1740$ lines/mm with $\lambda = 1.054 \mu\text{m}$ for the laser, then $\frac{\lambda}{d} = 1.83$, and there will only be first order refraction since $\sin \theta + \sin \gamma \leq 2$.

The geometry for introducing a positive chirp is shown in Fig. C.1. Positive (frequency) chirp is achieved due to the group velocity dispersion (GVD) of the system: longer wavelengths travel a longer path than shorter wavelengths. The path difference between two spectral components with wavelengths $\lambda + \delta\lambda$ and λ is given by:

$$\begin{aligned} \delta x &= \text{AB} + \text{BD} \\ &= \text{BC}(\sin \theta + \sin \gamma) \\ &= \text{BC} \frac{\lambda}{d} \quad (\text{from eq. (C.1)}) \\ &= \frac{\text{AC} \lambda}{\cos \theta d} \\ &= \frac{\text{OC} \lambda}{\cos \theta d} \delta \theta \\ &= \frac{L \lambda}{\cos^2 \theta d}. \end{aligned}$$

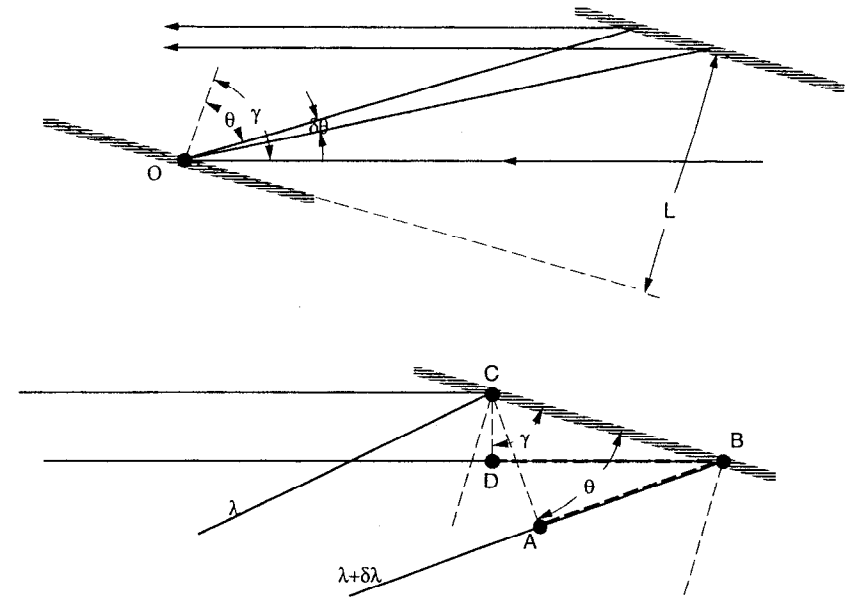


Figure C.1: Grating compression setup.

Differentiating eq. (C.1) gives

$$\frac{d\theta}{d\lambda} = \frac{1}{d \cos^3 \theta} \quad (\text{C.2})$$

such that the path difference becomes

$$\frac{dx}{d\lambda} = \frac{1}{d} \frac{L \lambda}{d} \frac{1}{\cos^3 \theta}$$

Typically the pulse system is run in a double pass configuration in order to remove the spatial chirp. This also gives twice the total delay. Therefore for a double pass configuration, the chirp introduced is

$$\frac{dt}{d\lambda} = \frac{2L\lambda}{c} \frac{1}{d \cos^3 \theta} \quad (\text{C.3})$$

It is evident that for a grating of width W the maximum delay is

$$\delta t_{\max} = \frac{2\lambda}{cd} W, \quad (\text{C.4})$$

independent of the grating angle.

For negative chirp the spectral component λ needs to be delayed with respect to $\lambda + \delta\lambda$. This is accomplished with the geometry shown in Fig. C.2 [81] and includes a 1:1 telescope such that $\delta\theta \rightarrow -\delta\theta$. The second grating is then "flipped" such that the refracted angle γ is preserved. The path delay in this configuration is

$$\begin{aligned} \delta x &= AB + BC \\ &= BE(\sin \theta + \sin \gamma) \\ &= BE \frac{\lambda}{d} \text{(as in the case of compression.)} \\ &= \frac{BD}{\cos \theta} \frac{\lambda}{d} \end{aligned}$$

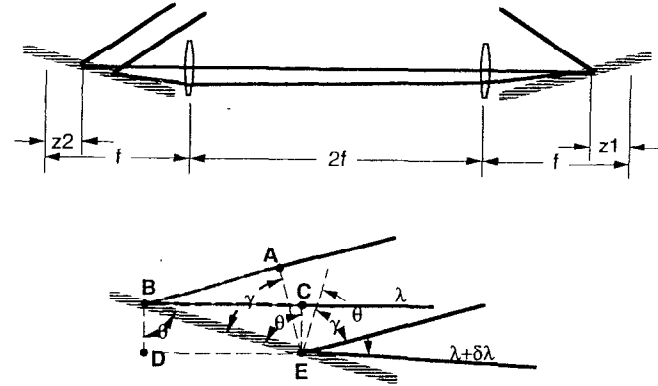


Figure C.2: Expansion setup.

This can be simplified with $BD = (z_1 + z_2)\delta\theta$, such that,

$$\delta x = \frac{(z_1 + z_2)\lambda}{\cos \theta} \frac{1}{d} \delta\theta.$$

Therefore, again using a double pass configuration, the chirp is

$$\frac{dt}{d\lambda} = \frac{2(z_1 + z_2)\lambda}{c} \frac{1}{d \cos^2 \theta} \quad (\text{C.5})$$

And, as in the case of positive GVD, the maximum delay is

$$\delta t_{\max} = \frac{2\lambda}{cd} W.$$

C.2 Design

The design of the expansion and compression stages is summarized in Table C.1. The negative chirp is used in the expansion stage while the positive is used in the compression in order to both keep the laser fluence low on the lenses and avoid breakdown at

Table C.1: Expansion and compression parameters.

gratings type and "rule"	1740/mm, Au, holographic, blazed 1.06 μm
grating size	80 mm x 110 mm (40x60 mm input side)
design wavelength	1.0535 μm
input angle (γ)	61.9°
refracted angle (θ)	72°
lenses (expansion)	1 m 3" dia. (2" input side)
spacing (expansion), $z_1 = z_2$	0.6 m
grating separation, $L / \cos \theta$	1.2 m
chirp, $\frac{dt}{d\lambda}$	267 ps/nm
maximum delay	1.34 ns
bandwidth acceptance	5.0 nm
spotsizes on grating (input)	2 mm ($1/e^2$, i.e., 1 mm σ)

the focus. The expansion and compression angles were designed to be the same such that the compression would compensate for the nonlinear chirp in the expansion (assuming the chirp is preserved in the regenerative amplifier). The angles were chosen to be as close to Littrow (the angle at which the input and output angle are identical) as was practical. This minimizes the astigmatism [104] as well as the non-linear chirp. Finally, the beamsizes are the same such that the resolution is consistent.

Appendix D

Grazing Incidence Design

The photocathode gun at the GTF allows for laser injection at both normal and grazing incidence. Normal incidence requires either a mirror inside the vacuum chamber (slightly off axis) or injection of the pulse after a bend in the electron beam. For the emittance data presented here the former was used. Two, major problems exist with this design:

- wakefields from the mirror contribute to an emittance growth in the beam.
- Dark current striking the mirror can cause damage to the mirror as well as electrostatic steering of the beam (see Appendix E).

Grazing incidence removes these problems and, in addition, because of the symmetric exit port on the gun, allows for access to the laser after it strikes the cathode (for energy and transverse profile measurements). For an appropriately polarized laser beam the quantum efficiency will increase at all but extremely near grazing incidence (see Section 6.1).

There are two major problems inherent in illuminating the cathode at grazing incidence: A circular transverse laser beam will illuminate an elliptical spot on the cathode, and the arrival time of the laser on the cathode will vary across the face of the cathode (see Fig. D.1.). For a laser pulse incident in the x - z plane at an angle α , measured with respect to the normal (z -axis), the spot size on the cathode is given, in general, by

$$w_{x,\text{cat}} = \frac{w_{x,\text{in}}}{\cos \alpha} \quad (\text{D.1})$$

$$w_{y,\text{cat}} = w_{y,\text{in}} .$$

The time slew across the pulse (along the x -axis) is

$$\delta t_{\perp} = w_{x,\text{in}} \tan \alpha . \quad (\text{D.2})$$

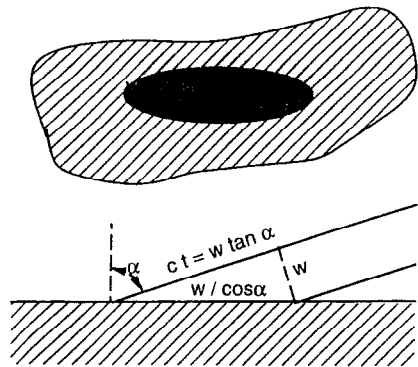


Figure D.1: Geometry of grazing incidence showing both the time-slew and the ellipticity generated by the incident laser beam.

The laser ports on the gun allow for 72° incidence. For a 2 mm circular beam, this would lead to an aspect ratio (w_x/w_y) of 3.2 with a δt_\perp of 18.5 ps. Clearly this is undesirable; however, a simple method has been developed for correcting both the time slew and ellipticity on the cathode using a single diffraction grating.

Use of a diffraction grating at angles different than Littrow will result in a change of the aspect ratio of the beam as well as introduce a time slew. For refraction in the $x-z$ plane, there will be

$$\begin{aligned} w_{x,g} &= w_{x,in} \frac{\cos \theta}{\cos \gamma} \\ w_{y,g} &= w_{y,in} \end{aligned} \quad (D.3)$$

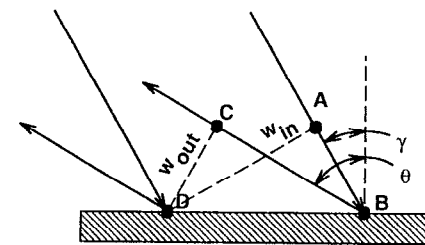


Figure D.2: Grating geometry for determining beam slew and aspect ratio.

It will also introduce a time slew in the beam of:

$$\begin{aligned} c \delta t_\perp &= AB + BC \\ &= \frac{w_{in}}{\cos \gamma} (\sin \gamma + \sin \theta) \\ &= n \frac{\lambda w_{x,in}}{d \cos \gamma} \end{aligned} \quad (D.4)$$

where eq. (D.3) and the grating equation (eq. (C.1)),

$$\sin \theta + \sin \gamma = n \frac{\lambda}{d},$$

have been used. Here γ and θ are the incident and refracted angles respectively, n is the refraction order, and d is the groove spacing. Note that there is not a tilted wave-front (which is unphysical) but rather a tilted amplitude front: the grating introduces a $2\pi n$ phase shift at each rule. By comparing eq. (D.1) with eq. (D.3) and eq. (D.2) with eq. (D.4), The conditions in which the delay can be pre-compensated for the grazing incidence are

$$\frac{n \lambda}{d \cos \gamma} = \sin \alpha. \quad (D.5)$$

However, for example, using a 3600/mm grating and $\lambda = 0.263 \mu\text{m}$ in 1st order there is no physical solution. But, a near solution exists with $\gamma = 0^\circ$, and thus, $\theta = 71.2^\circ$. This

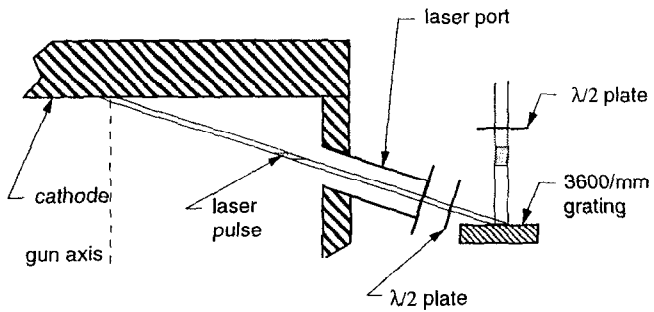


Figure D.3: Grazing incidence design: no dispersion correction.

"solution" results in easy alignment and only a $\sim 4\%$ error in both the aspect ratio and the delay compensation. A schematic of the setup is shown in Fig. D.3. For the 2 mm beam described above, this leads to an aspect ratio of 1.04 and a delay across the beam of ~ 240 fs. For comparison, at near normal incidence $\alpha \sim 4$ mrad which has almost no effect on the aspect ratio but gives approximately the same delay across the beam.

The above discussion assumes that the pulse has zero bandwidth. Due to the dispersion of the grating, the finite bandwidth of the pulse, leads to an error in both the spot size and delay as calculated above. The (angular) dispersion of the grating is found by differentiating eq. (C.1):

$$\frac{d\theta}{d\lambda} = \frac{n}{d \cos \theta}. \quad (\text{D.6})$$

For a transform limited 1 ps Gaussian pulse in the UV the bandwidth is ~ 0.1 nm. Using the above conditions this leads to a ~ 1 -mrad spread in the beam. Assuming the grating is 20 cm from the cathode this leads to an increase in the spot size from 2 mm to 2.2 mm and a 600 fs delay across the pulse. Of course, by imaging the grating onto the cathode, this effect can be removed at the expense of ease of alignment.

Appendix E

Normal Incidence Mirror Charging

The electron beam pointing in the GTF showed periodic temporal behavior. The beam would move slowly ~ 1 mm horizontally and then suddenly snap back into place. The time scale of the motion was over the course of many minutes perhaps up to 1/2 hour at first, but the time scale progressed to a period as short as 1 minute. The more rapid motion seemed to coincide with the considerable more dark current being produced from the rf gun after damage to the cathode occurred. It was eventually determined that enough dark current was striking the normal incidence laser mirror to cause an electrostatic steering of the beam. The sudden snapping of the beam was due to the discharge of the electrons from the mirror to its mount which was grounded to the beam pipe. Fig. E.1 shows one such discharge occurring. Fig. 3.5 on page 58 shows the geometry for normal incidence while Fig. 3.1 on page 54 shows the location of the Faraday cups.

The mirror was made of BK7 glass with a high reflective dielectric stack coating on the surface. It was 1 inch in diameter and 3/8 inch thick. The mirror had been significantly radiation darkened, and small fissures had developed both on the surface and in the bulk. A test mirror was coated with Chromium except over a small (few mm) area for the laser to strike and was grounded to the mirror mount. Breakdown occurred in this mirror as well leading us to believe that much of the charge was being deposited in the bulk of the mirror. The quickest solution (short of a conducting mirror) was to use a thin (~ 1 mm) 1/2" diameter Aluminum coated mirror. The new mirror has relatively poor reflectance $\sim 90\%$, but has been quite stable to the effects of the beam.

The electron beam motion was on the order of 1 mm over approximately 250 mm corresponding to an average angular kick of 4 mrad. For a 6 MeV electron beam this requires a transverse kick of only 24 kV.

The magnitude of the charge on the mirror which is required to produce the observed motion is estimated by assuming that the charge is localized at the edge of the mirror. The beam axis is approximately 10 mm from the mirror. If it is then assumed that the electric field is due to a point charge, the beam will be accelerated (transversely) across a potential given by

$$V = - \int \vec{E} \cdot d\vec{l} = \frac{Q}{4\pi\epsilon_0 d}$$

With $d \approx 10$ mm, $Q \approx 30$ nC for the 24 kV kick.

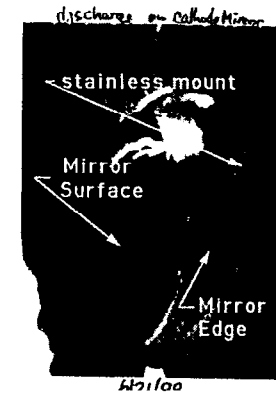


Figure E.1: Discharge from the normal incidence laser mirror.

For consistency, the time it takes to charge the mirror to 30 nC is estimated. The conductivity of the mirror is assumed to be essentially zero such that all charge remains on the mirror until a breakdown occurs. Typically just about 50% of the dark current beam is lost from the position of the first Faraday cup to the second Faraday cup due to its large energy spread. The laser mirror sits longitudinally at the same position as the first Faraday cup. The beam pipe inner diameter is ~ 35 mm while the laser mirror

extends approximately 7 mm into the beam pipe (for a 1" diameter mirror). The result is that the ratio of the cross section of the exposed portion of the mirror to the cross section of the beam pipe is $\sim 1/6$. If the charge is lost uniformly, then at 10 Hz and 6 nC dark current out of the gun, it would only take 6 seconds to charge the mirror. This is within about an order of magnitude of what was observed.

Even with a mirror which doesn't charge, the effects of the wake-field from the beam itself may become large. As the head of the beam passes the mirror (and its mount) it produces an image charge which can act on the tail of the beam. Since the beam is on the order of 1 mm radius at this point and $\gamma \sim 10$, a 100 μ rad kick could be enough to increase the emittance by 1π mm-mrad. This is approximately the same kick which would be received for 1 nC of charge from the discussions above. The appropriate solution is either to move the mirror to after the linac or to use grazing incidence illumination of the cathode (avoiding the normal incidence mirror altogether).

Appendix F

Emittance Data

Table F.1: Summary of emittance data. The first error is the estimated from a least squares fit and is not scaled to the χ^2 . The second error is a fixed 18.8% error due to the calibration uncertainty. Also given is the calculated spotsize before the first quadrupole.

charge [nC]	τ_{laser} [ps FWHM]	$\epsilon_{n,rms}$ [π mm-mrad]	χ^2_{dof}	solenoid [kG]	spotsize [mm]
1	5 ps	28.8 \pm 1.1 \pm 5.4	0.023	1.8	2.1
		22.0 \pm 0.3 \pm 4.1	1.9	1.9	1.6
		18.4 \pm 0.1 \pm 3.4	0.47	2.0	1.0
		14.4 \pm 0.4 \pm 2.7	0.60	2.1	0.37
		12.9 \pm 0.5 \pm 2.4	3.3	2.2	0.45
		22.0 \pm 0.5 \pm 4.1	4.6	2.3	1.1
1	8 ps	23.0 \pm 0.8 \pm 4.3	0.53	1.8	1.5
		16.9 \pm 0.7 \pm 3.2	3.0	1.9	1.2
		13.5 \pm 2.1 \pm 2.5	0.33	2.0	0.53
		15.9 \pm 0.3 \pm 3.0	5.0	2.1	1.0
		19.2 \pm 0.7 \pm 3.6	7.0	2.2	1.6
		27.8 \pm 0.9 \pm 5.2	7.6	2.3	0.98
1	11 ps	16.7 \pm 0.6 \pm 3.1	0.79	1.9	0.42
		12.3 \pm 1.0 \pm 2.3	3.8	2.0	0.48
		12.2 \pm 0.2 \pm 2.3	2.4	2.1	1.3
		24.8 \pm 0.3 \pm 4.6	6.6	2.3	1.1
0.5	5 ps	23.1 \pm 0.3 \pm 4.3	2.8	1.8	1.7
		15.6 \pm 0.1 \pm 2.9	1.0	1.9	0.99
		10.5 \pm 0.2 \pm 2.0	1.3	2.0	0.50
		11.1 \pm 0.3 \pm 2.1	0.75	2.1	0.39
		14.8 \pm 0.3 \pm 2.8	3.9	2.2	0.79
0.5	8 ps	18.8 \pm 1.2 \pm 3.5	6.0	2.3	1.3
		16.9 \pm 0.2 \pm 3.2	1.9	1.9	1.2
		8.0 \pm 1.3 \pm 1.5	0.68	2.0	0.44
		13.4 \pm 0.4 \pm 2.5	1.1	2.1	0.41
0.5 ^a	5 ps	24.3 \pm 1.1 \pm 4.6	0.54	2.3	1.5
		16.8 \pm 0.3 \pm 3.1	10	1.9	0.74
		15.6 \pm 3.1 \pm 2.9	2.1	2.0	0.55
		18.1 \pm 0.8 \pm 3.4	0.95	2.1	0.60
0.5 ^a	5 ps	17.7 \pm 0.5 \pm 3.3	49	2.3	0.98

^a A transversely clipped laser (1 σ) is used for these data.

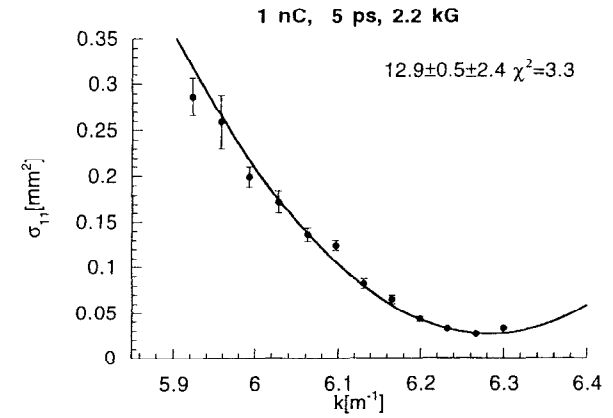


Figure F.1: Quadrupole scan for the minimum emittance at 1 nC and 5 ps.

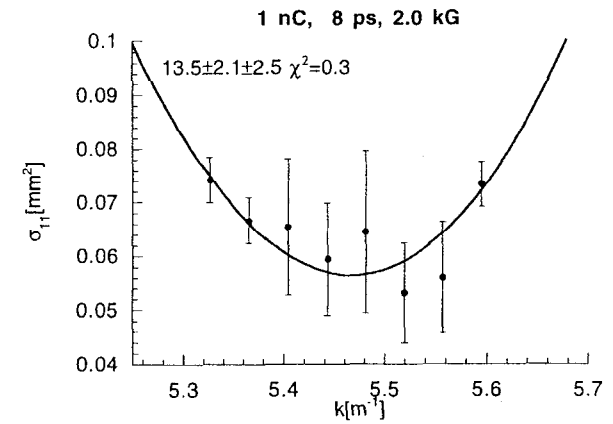


Figure F.2: Quadrupole scan for the minimum emittance at 1 nC and 8 ps.

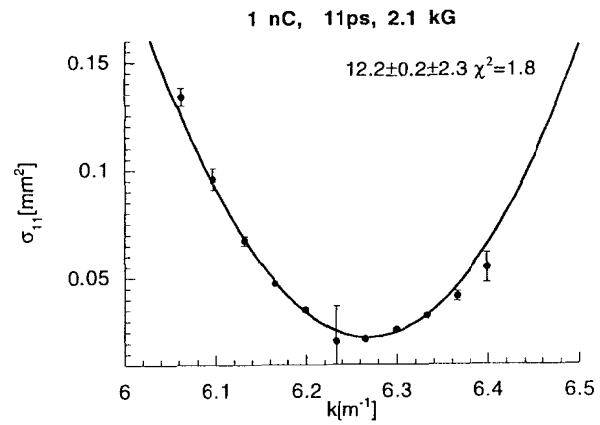


Figure F.3: Quadrupole scan for the minimum emittance at 1 nC and 11 ps.

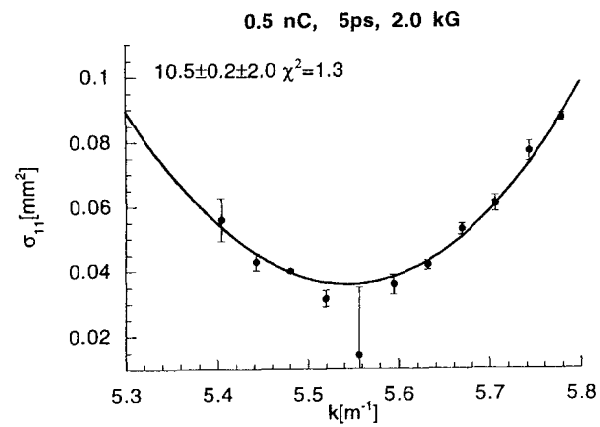


Figure F.4: Quadrupole scan for the minimum emittance at 0.5 nC and 5 ps.

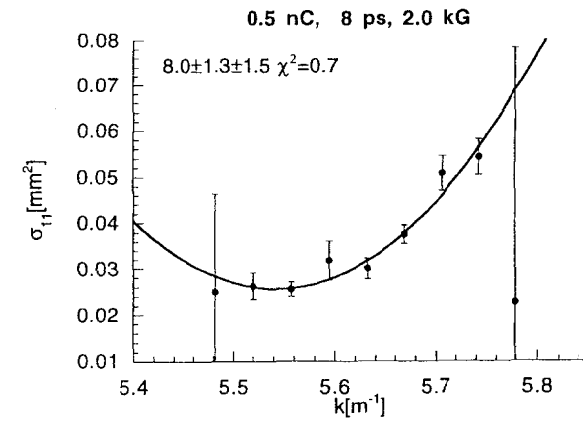


Figure F.5: Quadrupole scan for the minimum emittance at 0.5 nC and 8 ps.

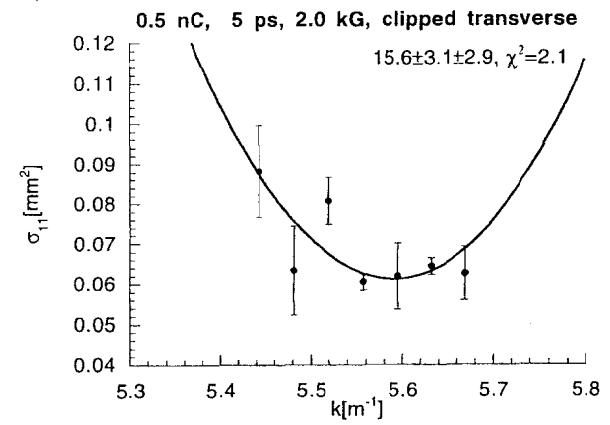


Figure F.6: Quadrupole scan for the minimum emittance at 0.5 nC, 5 ps, and transversely clipped.